

# Numerical studies of 3-D developing laminar flow in a microchannel

Tan, Swee Tiong

2007

Tan, S. T. (2007). Numerical studies of 3-D developing laminar flow in a microchannel.  
Doctoral thesis, Nanyang Technological University, Singapore.

<https://hdl.handle.net/10356/6490>

<https://doi.org/10.32657/10356/6490>

---

Nanyang Technological University

*Downloaded on 04 Apr 2024 09:35:06 SGT*



**NANYANG  
TECHNOLOGICAL  
UNIVERSITY**

**NUMERICAL STUDIES OF 3-D DEVELOPING  
LAMINAR FLOW IN A MICROCHANNEL**

**TAN SWEE TIONG**

**SCHOOL OF MECHANICAL AND  
AEROSPACE ENGINEERING**

**2007**

NUMERICAL STUDIES OF 3-D DEVELOPING LAMINAR FLOW IN A MICROCHANNEL

TAN S. T.

2007

# **Numerical Studies of 3-D Developing Laminar Flow in a Microchannel**

**Tan Swee Tiong**

School of mechanical and Aerospace Engineering

A thesis submitted to the Nanyang Technological University  
in fulfilment of the requirement for the degree of  
Doctor of Philosophy

**2007**

## Chapter One

### INTRODUCTION

#### 1.1 Background

Microchannel was initially developed to fulfill the requirements from electronic devices. The demand of functional response for electrical component increases rapidly. However the design of high-speed, high-power integrated circuits and systems is often constrained by thermal considerations. Figure 1.1 shows the exponential relationship between failing rate of electric component and its temperature.

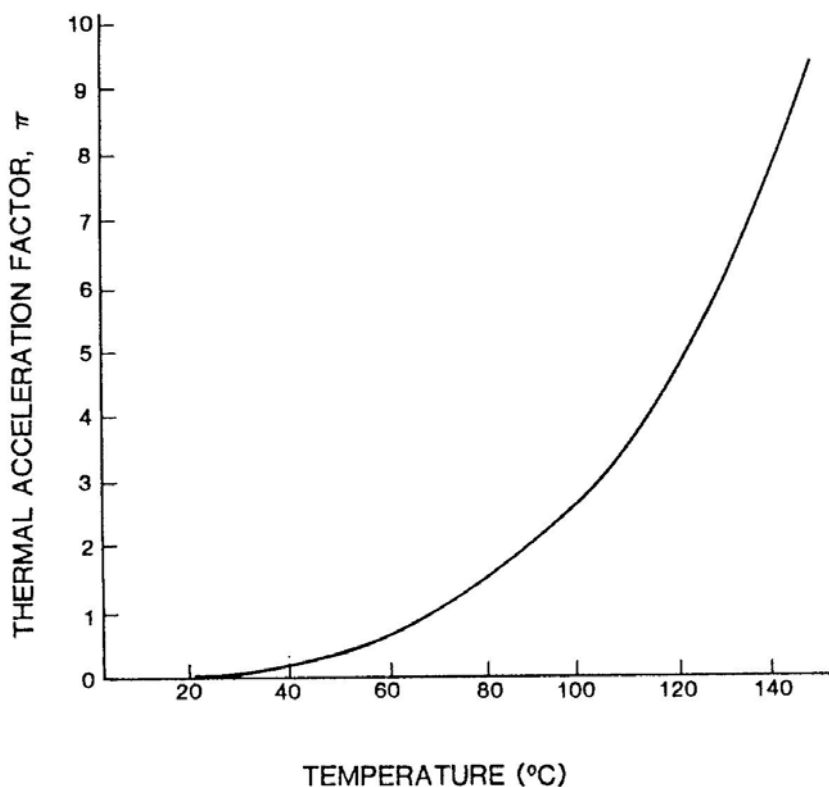


Figure 1.1 Thermal acceleration factors at different temperature [Philips (1990)]

However, there is a contradictory requirement for high rates of heat dissipation with low allowable temperature rise. Heating rates on the order of 10

$\text{Wcm}^{-2}$  are commonly produced and the allowable temperature rise is usually limited to approximately  $80^\circ$  above a  $20^\circ\text{C}$  ambient. In this decade however, the allowable temperature rise is expected to decrease somewhat, and the heat dissipation rate would be in the range of 200 to  $1000\text{Wcm}^{-2}$  [Philips (1990)]. As shown in Figure 1.2, this level of heat flux is comparable to that of a nuclear blast, but must be accommodated at a much lower temperature.

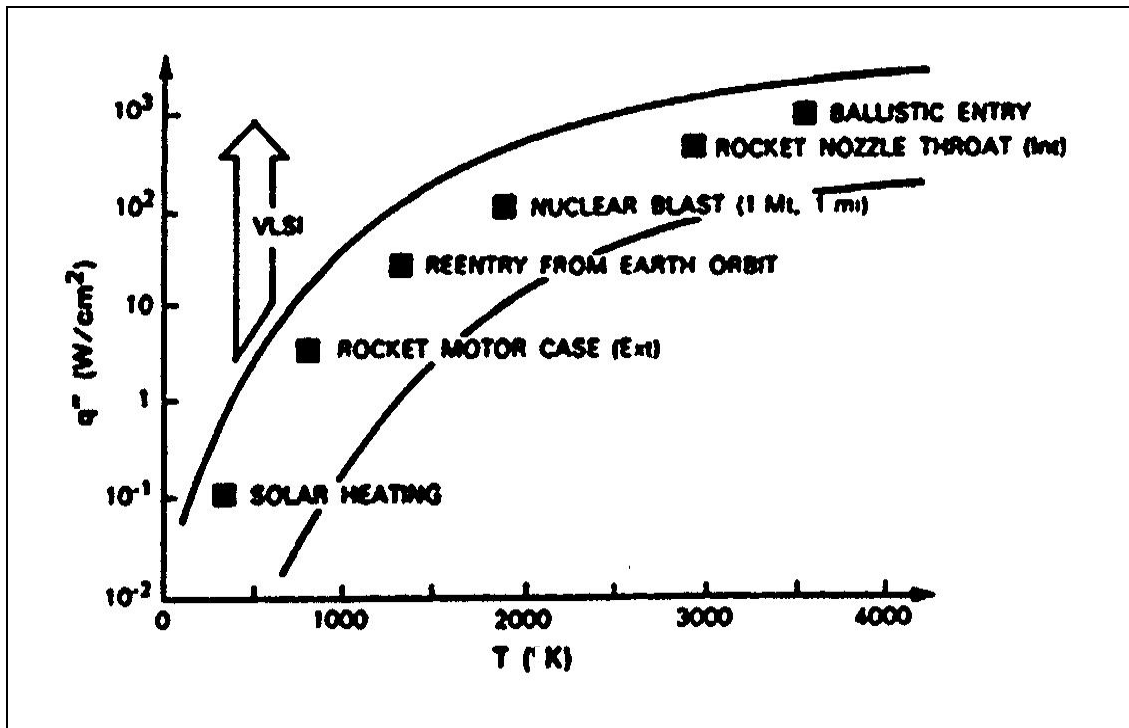


Figure 1.2 Perspective on microelectronic heat fluxes [Philips (1990)]

Hence, innovative cooling techniques will be required to fulfill these specifications and one such method is the use of forced convection heat spreaders called microchannel heat sinks. Microchannels, with their extreme high surface area to volume ratio, have high potential to be efficient heat sink for electric device. A microchannel heat sink is a structure with numerous channels and fins arranged parallel to one another and very close to the heated surface. A schematic diagram of microchannel is shown in Figure 1.3. The dissipated heat passes through the heat sink

by conduction and to the coolant by forced convection. The coolant is usually a liquid rather than a gas and the flow is usually single phase rather than two-phase. With the advancement of micromachining techniques, constructing such small but highly efficient micro heat exchangers is feasible.

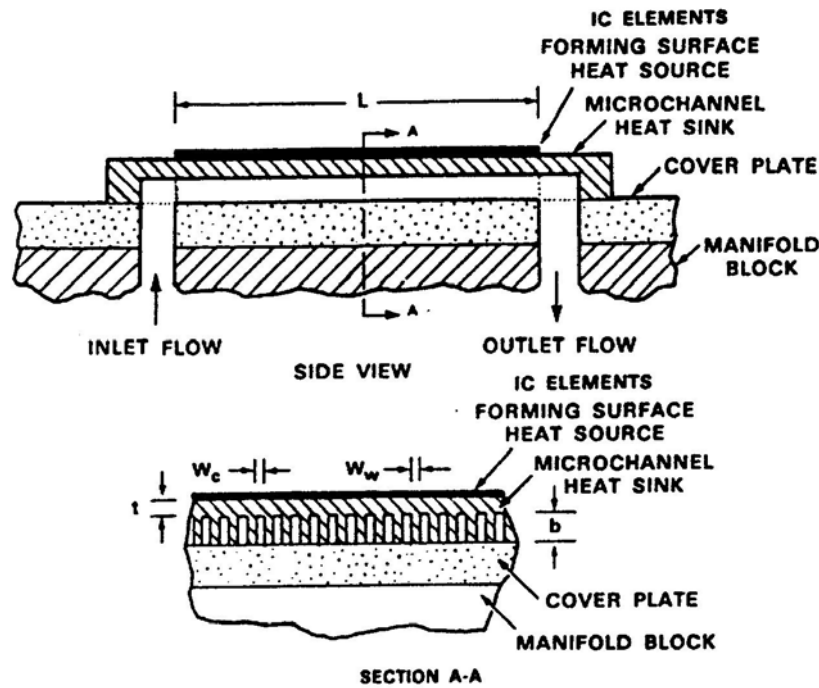


Figure 1.3 Schematic view of a micro-channel heat sink fluxes [Philips (1990)]

Tuckerman and Pease first introduced the concept a microchannel heat sink in 1981 at Stanford University [Tuckerman and Pease (1981)]. Other researchers' efforts are summarized in Chapter two. Microchannel array has been found effective in cooling electronic devices [Yang and Li (1997)].

Microchannels were also used in the area of biomedical; one of the important applications is in the separation of biological or chemical components, such as the separation of DNA in genetic engineering [Fu et al, (2002a)]. In practice, it is called electrophoresis. It uses the principle of different mobility of dielectric particles to

move in opposite direction of the electrical potential under an applied electric field. The induced flow motion is also called electroosmotic flow. The separation microchannel of electrophoresis is designed generally on a microfabricated chip within a compact chip. Figure 1.4 shows schematics of four separation microchannels on chips.

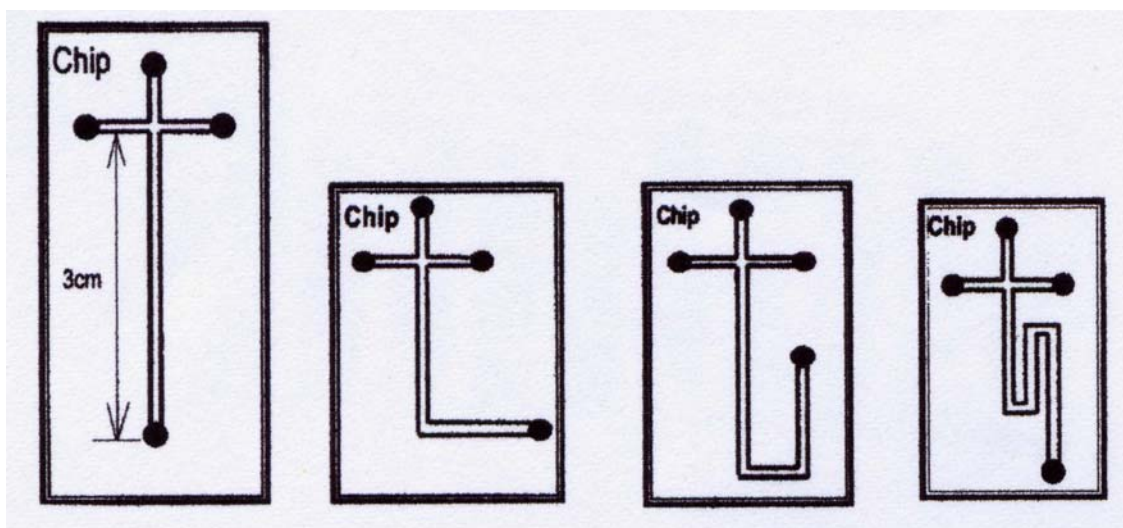


Figure 1.4 Schematics of four separation microchannels on chip  
[Fu et al (2002a)]

In the application of heat transfer for electrical, the ratio of height to width (aspect ratio) of the microchannel is close to zero, hence most of analysis for microchannels were done in 2-D [Mala, Li and Dale (1997)]. 3-D analysis is important in order to obtain more realistic prediction. In classical study [Shah and London (1978)], it was suggested that even for aspect ratio of 0.1, the performance of a rectangular channel such as friction coefficient,  $fRe$ , is significantly different from that predicted using 2-D model (aspect ratio equal to zero, as shown in Figure 1.5). In the application of separation of DNA, the typical dimensions of microchannel [Fu et al (2002b)] were  $39.95\mu\text{m}$  in depth and  $80\mu\text{m}$  in width. In such cases, predictions using 2-D model will not be realistic.

The performance of microchannel was found different from that predicted using classical Navier-Stokes equations, which was able to provide good prediction for macroscale flow. Mala, Li and Dale (1996), introduced the effect of interfacial electric double layer (EDL) on microchannel flow to explain deviations of microscale flow from macroscale flow. The EDL effect is now found to be an important effect for microchannel flow which cannot be ignored.

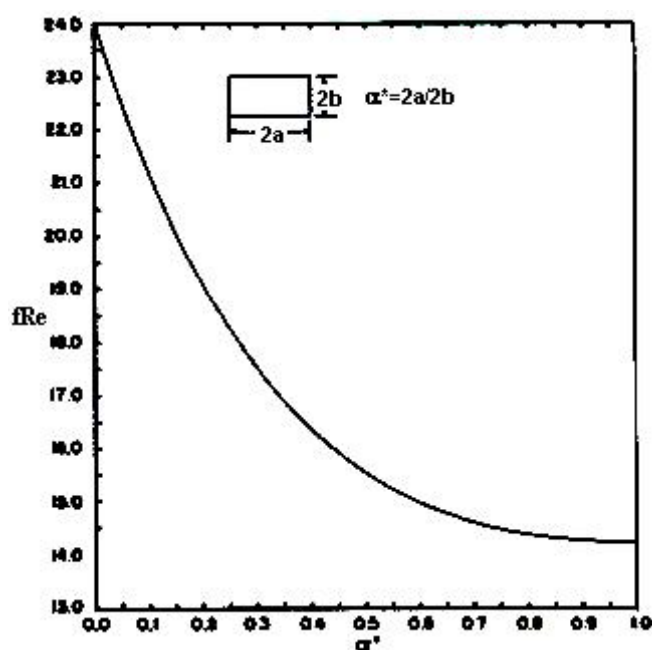


Figure 1.5  $fRe$  values for fully developed laminar flow for rectangular channel of different aspect ratio [Shah & London (1978)]

In this work, a numerical simulation was carried out to predict the performance of microchannel based on 3D-flow field. The developing region was included in the simulation to obtain a more realistic prediction. The EDL effect was also considered as it was found to be significant in the 2D-model.

## 1.2 Objectives



The objectives of this project are:

1. To simulate the liquid flow field for developing flow in the microchannel configuration with the EDL effect.
2. To study the significance of the EDL effect on pressure driven liquid flow in microchannel.
3. To study the difference between effects of the ionic concentration distributions on microchannel, as described and computed using the two different equations namely Boltzmann distribution equation and the Nernst-Planck equation.
4. To study the effectiveness of using microchannels for the cooling of electronics devices.

### 1.3 Scopes

The scopes of the project include:

1. To understand the governing equations and boundary conditions of flow and heat transfer in microchannels.
2. To construct mathematical model to simulate flow in microchannel and EDL effect.
3. To carry out numerical simulation for flow field of the microchannel, so as to establish the basic understanding the performance of microchannel.
4. To understand the EDL effect on the microchannel flow.

## Chapter Two

### LITERATURE REVIEW

---

#### 2.1 PURE EXPERIMENTAL STUDIES

In their pioneering work, Tuckerman and Pease (1981) demonstrated that conventional liquid heat exchanger technology could be scaled down to tens of micrometers and applied to silicon chips. They were able to extract 800 W from a 1-cm<sup>2</sup> chip with a 71°C temperature rise, demonstrating micro-channel heat sinks as an effective means of cooling high heat loads. The fundamental notion that, at a constant Nusselt number, the heat transfer coefficient is inversely proportional to the channel width was the foundation of their design. Their analysis of fully developed laminar flow has been the starting point for all subsequent analyses and similar experiments under the transmission of either liquids or gases in a variety of channels. Theoretical analysis of such micro-cooling system has been studied with some simplifications, which included:

1. The heat transfer coefficients along the channel walls are uniform
2. The heat transport occurs only through the vertical fins
3. The fluid temperature at each cross section is uniform

Mahalingam and Andrews (1988) studied several air-cooled silicon heat sinks and an air-cooled copper heat sink. A thermal performance model was presented which was based on incompressible flow (airflow Mach numbers were less than 0.2). Thermal spreading at the heat source perimeter was not taken into account, which helps to explain why the predicted thermal resistance was usually greater than experimental values by 25%.

Harley *et. al.* (1989) conducted an experimental investigation of fluid flow in extremely small channels to determine the length scales at which the continuum assumptions break down and if the Navier-Stokes equations adequately predict fluid behaviour. It was found that the Navier-Stokes equations start to predict a lower Darcy friction factors on the order when the length scale is around  $0.67\sim 6.7\mu\text{m}$ . In all, due to the breaking-down of continuum assumptions break down. Navier-Stokes equations were not suitable in predicting the behavior of air in microscale.

You (1989) determined the heat transfer coefficient between a complex microstructure and the flowing fluid by the measurement of the temperatures of the porous materials and the fluid in conjunction with a mathematical analysis. The functional relation of Nusselt number and the Reynolds number based on hydraulic diameter for the case of a microchannel was found to be in excellent agreement with the circular tube solutions.

Pfahler *et. al.* (1991) presented measurements of the friction factor or apparent viscosity of fluids flowing in small channels etched in silicon with depths ranging from  $0.5\mu\text{m}$  to  $50\mu\text{m}$ . The liquids used were isopropyl alcohol and silicone oil, and the gases were nitrogen and helium. The fluid's apparent viscosity was found to be consistently smaller than predicted by conventional, incompressible theory. The apparent viscosity was also found to decrease with decreasing depth for liquids.

Knight *et. al.* (1992[b]) continued their study of the option of micro-channel heat sink by conducting an experimental verification on to the models proposed in an earlier work by Knight *et. al.* (1992[a]). The experimental resistance values were higher than the predicted values due to the over prediction of volumetric flow rates.

Assuming that the heat transfer coefficient to be constant along the fin and neglected heat transfer from the channel bottom Tuckerman (1984) and Samalam (1989) concluded that the heat transfer coefficient attained a local maximum at the mid-point (both height and width). More heat would thus flow upwards in the fin. The fin temperature would tend to be more uniform than predicted by the model with the constant heat transfer coefficient. This would be especially true when the solid thermal conductivity is much larger than that of the fluid. The problem could be simplified under certain conditions by assuming the solid to be isothermal (i.e. the solid thermal conductivity is infinitely large compared to the fluid). The investigation had extended to the flat plate heat exchangers similar to those fabricated into the back of electronic chips by Weisberg & Bau (1992). They also presented a design algorithm for the selection of the heat exchanger dimensions.

Rahman and Gui (1993) performed experimental measurements of fluid flow and heat transfer in microchannel cooling passages in a chip substrate. Two different channel patterns (I-channel and U-channel) were designed for the flow field and the performance of microchannel. It was found that Nusselt numbers were larger than analytically predicted values using developing flow equations. The transition from laminar to turbulent flow was somewhat gradual because of small channel dimension, which is of the same order of magnitude as the turbulent length scale. The larger heat transfer is caused by the breakage of velocity boundary layer by surface roughness associated with etched channel structure.

The mechanism for the micro-bubble formation in the microchannels is of particular interest for applications of micro-scale phase change. Lin *et. al.* (1993) investigated the formation of vapor bubbles on a micro heater inside microchannels.

The micro heater has a typical dimension of  $0.3 \times 2 \times 50 \mu\text{m}^3$  and is made of heavily phosphorus-doped poly-silicon. The micro-bubble formation process was observed under a microscope, recorded and photographed. Maximum surface temperatures on the micro heaters were calculated by a lumped one-dimensional model. The nucleation temperature was calculated to be close to the critical point of the three liquids tested.

Although micro-channels are effective in the heat transfer mechanism, however, there is a large pressure drop that accompanies. A group of researchers investigated the possibilities of using a mini-channel instead to combine the benefits of both worlds. Bowers and Mudawar (1993) presented the design criteria and heat diffusion constraints for two-phase electronic cooling using mini-channel ( $D=2.54\text{mm}$ ) and micro-channel ( $D=510\mu\text{m}$ ) heat sinks. Emphasis was placed on analyzing thermal conduction within the heat sink to determine the optimum channel geometry based upon dimensionless cell width and heat sink thickness.

Bowers and Mudawar (1993) continued their study for two-phase electronic cooling using mini- and micro-channel heat sinks by emphasizing on reducing pressure drop and coolant flow rate. A pressure drop model was introduced that accounts for the single-phase inlet region, the single- and two-phase heated region, and the two-phase unheated outlet region. Inlet and outlet losses associated with the abrupt contraction and expansion, and the effects of compressibility and flushing within the two-phase region were also accounted for. It was found that the acceleration caused by evaporation in the channels attributed mainly to the pressure drop. However, compressibility effects were also significant in micro-channel geometry especially at Mach number exceeding 0.22. They concluded that the large pressure drop and the

potential for choking warrant the use of very small channels. They pointed out the advantages of mini-channels i.e. low-pressure drop, negligible compressibility, acceptable erosion, low likelihood of clogging and the ease of manufacturing. However, they agreed that micro-channels are still important in cases that demand dissipation of high heat fluxes and minimizing the weight and liquid inventory like avionics and space electronics.

Bowers and Mudawar (1994) furthered their study on mini- and micro-channel [Bowers and Mudawar (1993)] by conducting an experimental work on the pressure drop and critical heat flux (CHF) in such channels. A single CHF correlation was developed for both heat sinks. The use of the CHF correlation and a generalized model for pressure drop as predictive tools in assessing the merits of different channel sizes were illustrated.

Pong *et. al.* (1994) experimentally investigated the non-linear pressure distribution in uniform micro-channels. Nitrogen and helium were used as a working medium in order to investigate the effect of Knudsen number in micro gaseous flow.

Peng, Peterson and Wang (1994) experimentally investigated the flow characteristics of water flowing through rectangular micro-passages, having equivalent diameters in the range 0.133 to 0.343 mm and depth to width ratios of 0.333 to 1. In their investigation of flow behavior, the measured data included primarily the pressure variation and the flow rate. Their experiments indicated that the flow regime conversion from laminar to turbulent flow took place at much lower Reynolds numbers than conventionally predicted values, and the transition region was also over a narrower bandwidth of Reynolds numbers. They stated that the Reynolds numbers for the occurrence of laminar flow was in the range of 200 to 700, and the friction factors for both laminar and turbulent flows deviated from the classical theories. It was also

reported that the geometric features of the micro-passages (e.g.  $D_{eq}$  and  $H/b$ ) have a substantial effect on the flow.

A series of experiments with several different micro-channels, were conducted by Wang and Peng (1994), Peng *et. al.* (1995) and Peng and Peterson (1995) to examine the convective heat transfer and better understand the fundamental physical phenomena associated with this type of flow situation. The experimental results indicated that the liquid convection characteristics are quite different from those observed in conventionally sized channels. The conversions of flow modes and heat transfer regimes are initiated at much lower Reynolds number ( $Re$ ) than for the conventional situation (2000-3000). The transition from the laminar flow regime occurs at  $Re$  at approximately 300, and the transition to the fully turbulent flow regime at about  $Re = 1000$ . The transitions are also strongly affected by the liquid temperature, liquid velocity and microchannel size, and hence are not only determined by  $Re$ . They observed that the transitional  $Re$  diminished as the size of the micro-channel decreased. Wang and Peng (1994) concluded that these effects were due to large changes in the thermo-physical properties of the liquid due to high heat fluxes in small channels.

Khrustalev *et. al.* (1995) conducted boiling heat transfer in an axially grooved copper water miniature heat sink with external dimensions of  $2.6 \times 7.7 \times 40 \text{ mm}^3$  in the horizontal orientations with heat fluxes on both sidewalls of up to 100 W. The heat sink provided a nearly uniform surface temperature, a low thermal resistance and operated with a significantly smaller pressure drop and larger heated length compared to single-phase heat sinks with microchannels.

Ravigururajan and Drost (1996) presented the single-phase flow characteristics of a diamond-pattern micro-heat-exchanger. It was noted that the heat transfer enhancement was less than that obtained in a parallel channel micro-heat-exchanger. It was also found to be independent of the mass flow rate. However, the pressure drop increased at a faster rate than that experienced in a parallel channel flow.

Peng *et. al.* (1996) further investigated the sub-cooled flow boiling heat transfer characteristics of binary mixtures in micro-channel plates. Generally, mixtures with small more volatile component concentrations augmented the flow boiling heat transfer, while those with large concentrations decreased the heat transfer as compared with pure volatile liquid. They reported an optimum concentration at which the flow boiling heat transfer reached a maximum value. These characteristics were found to be affected by both liquid flow velocity and amount of sub-cooling. The heat transfer coefficient at the onset of flow boiling and in the partial nucleate boiling region was greatly influenced by liquid concentration, micro-channel and plate configuration, flow velocity and the amount of subcooling. However, micro-channel size, flow velocity, sub-cooling of the mixture and liquid concentration had no significant effect on the heat transfer coefficient in the fully nucleate boiling regime. The level of augmentation induced by increasing the number of channels diminished as size decreased.

Nguyen *et. al.* (1996) conducted an experimental investigation, numerical simulation and analytical modeling of forced convection in an electro-caloric mass-flow sensor.

Arkilic, Schmidt and Breuer (1997) performed an analytical and experimental investigation into gaseous flow with slight rarefaction through long microchannels. A two-dimensional analysis of the Navier-Stokes equations with a first-order slip-



velocity boundary condition demonstrated that both compressibility and rarefied effects were present in long microchannels. The model predicted an increase in mass flow for a given inlet and outlet pressures in microchannel flows that is based on a perturbation expansion of the Navier-Stokes equations with a first-order correction of wall slip. They also developed a mass-flow measurement technique with a resolution several orders of magnitude higher than that available commercially. The technique also allowed similar measurements to be made at various outlet pressures.

An experimental study of the EDL effect on micro-scale fluid flow was undertaken by Mala, Li, Wemer, Jacobasch and Ning (1997). Experiments were conducted to investigate the effects of EDL on flow characteristics with different potassium chloride concentrations in water and with different plate materials, P-type, silicon and glass. Microchannels with a height from 10 to 280  $\mu\text{m}$  were used in the experiments. The predicted volume rates from a mathematical model developed agreed well with the measured data.

Emi *et. al.* (1997) investigated experimentally on a flat plate on micron-sized rough surfaces for the purpose of possible boundary layer characteristics change. Direct drag and boundary layer measurements were performed on different types of micron-sized rough surfaces (textile and fiber surfaces). At a certain Reynolds number range, 7%-9% drag reduction was observed. Detailed boundary layer measurement showed that some of the characteristics of the turbulent boundary layers over such surfaces were different from that of smooth surface.

Diev *et. al.* (1997) studied, experimentally, micro-layer evaporation and its role in heat transfer during boiling in narrow vertical slot channels. The distribution of

micro-layer thickness along the vertical radius was obtained from interferograms taken using a one beam laser interferometer and high-speed photography.

Adams *et. al.* (1998) conducted experiments on turbulent, single-phase forced convection of water in circular micro-channels with diameters of 0.76 and 1.09 mm. Nusselt numbers for micro-channels were found to be higher than that of traditional large channels.

Peng *et. al.* (1998) also analyzed the thermodynamic aspects of phase transformation of liquids in micro-channels to further understand its boiling characteristics and to determine the conditions under which a portion of such liquids is likely to undergo phase change. A non-dimensional parameter and related criteria that determined the phase transition in micro-channels were derived theoretically. The results provided a theoretical and quantitative basis for the evaporating space hypothesis and for nucleation in microchannels.

Most of the latest experimental works were done to validate new theoretical, numerical and analytical works. These experimental works will be listed in section 2.2.

## 2.2 THEORETICAL, NUMERICAL AND ANALITICAL WORKS

### 2.2.1 Models without EDL effect

Philips, Glicksman and Larson (1987) theoretically and numerically studied microchannel heat sinks for fully developed and developing flow in the laminar and turbulent flow regimes, without considering the electric double layer (EDL) effect. A detailed theoretical model of thermal and fluid performance applicable to moderate aspect ratio channels was developed. To facilitate numerical computation based on that model a computer program was written. Comparisons between theory and experimental data showed good agreement (typically within 20%). Typical sizes studied used were channel width =  $220\mu\text{m}$ , substrate width =  $155\mu\text{m}$ , channel depth =  $165\mu\text{m}$  and channel length =  $0.97\text{cm}$ . An array of four  $0.25 \times 0.25 \text{ cm}^2$  resistors provided the surface heating for the test chips, and heat dissipation rates were obtained in excess of  $1000 \text{ Wcm}^{-2}$  with thermal resistance as low as  $0.072^\circ\text{C}/(\text{Wcm}^{-2})$ . They also noted that turbulent heat sink designs could have equivalent or better thermal performance than comparable laminar flow designs. The pumping power requirements for the turbulent flow designs can be kept below  $10 \text{ Wcm}^{-2}$ . The typical channel width for turbulent flow designs was in the range of 200 to  $300 \mu\text{m}$  and larger.

Phillips *et al.*'s (1987) effort also included the development of a novel "compensation heater" that can be used to enhance temperature uniformity of integrated circuits and diode laser arrays. Shown schematically in Figure 2.1, a compensation heater surrounds the primary device and dissipates heat at an equivalent rate. The width of the heater is sized such that the zone of peripheral thermal spreading is displaced outwards. Thermal spreading provides for considerable non-uniformity in the thermal resistance for the short heater design, whereas the uniformity

in the thermal resistance is much better for the longer heater length over the same range from the channel entrance. Phillips *et al.* believed that such a device could enhance IC reliability and enhance design due to improved uniform IC temperature. However, this concept is yet to be evaluated experimentally using chip-level reliability testing to verify its validity.

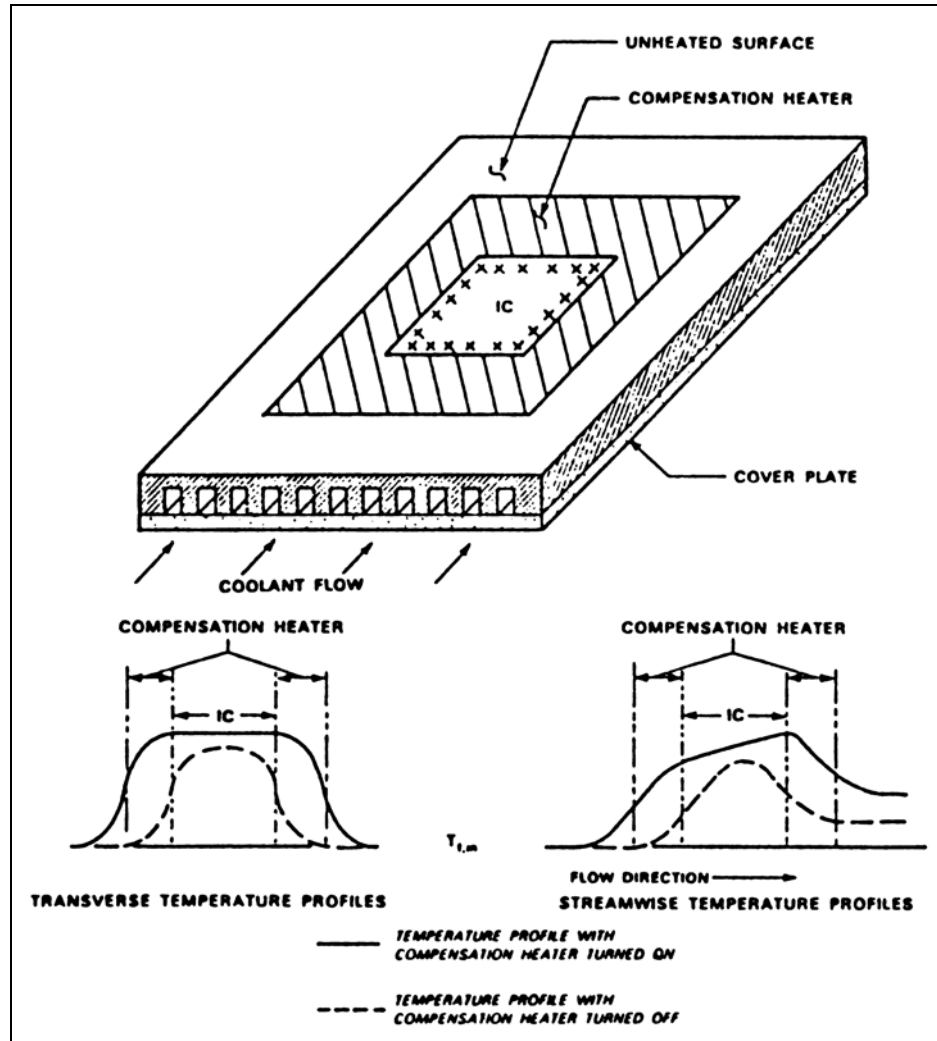


Figure 2.1 Compensation heater concepts [Phillips (1990)]

Samalam (1989) reduced the analysis to a quasi-2-dimensional differential equation. This resulted in an exact solution to obtain the optimum dimensions for the channel width and spacing analytically. Numerical examples showed that the thermal resistance could be reduced by using the optimum values. A Laplace transformation

was used to solve the governing equations and to define the temperature field in each fin. The channel width and spacing dimensions were then optimized based on the obtained solution of flow and temperature fields. The objective function used was thermal resistance. Aspect ratios as large as 10, were found to be desirable although aspect ratios varying from 4 to 6 were predicted to provide acceptable performance.

Phillips (1990) published a comprehensive review of all microchannel work to date. Analysis of developing and developed flow, both laminar and turbulent, with excluding the electric double layer (EDL) effect, was presented. Parametric variations of fin-to-channel width ratio, channel height and aspect ratio, substrate thickness and channel length were performed. A form of manifolding was proposed, in which the flow enters and exits the micro-channel several times along the flow length. This improved convective heat transfer by keeping a great part of the micro-channel in developing flow, but did not reduce the pressure drop or bulk heating of the liquid.

Flik *et. al.* (1991) developed regime maps showing the boundary between micro-scale and macro-scale heat transfer regimes. The maps related the smallest geometric dimension to temperature for conduction in solids, to temperature and pressure for convection in gases, and to the temperature of the emitting medium for radioactive transfer. The material purity and defect structure strongly influence the regime boundaries. Microstructures pertaining to a given technology can be marked on these maps to determine whether heat transfer theory is applicable. By marking the regions on the maps for the expected future development of micro-technologies, research needs in micro-scale heat transfer can be anticipated.

For many microstructures, which utilize forced convection cooling; the average thickness of the thermal boundary layer is of the same order as the length of the heated element. For these cases, thermal boundary layer theory is invalid. Ma et al. (1992)

analyzed the elliptic energy equation for steady, two-dimensional incompressible flow over a finite flat plate with insulated starting and ending lengths utilizing matched asymptotic expansions. A conventional Blasius technique transforms the energy equation into an elliptic-to-parabolic equation. A new technique was introduced which treats the boundary layer solution as the outer expansion of the elliptic-to-parabolic equation.

Nagasaki *et. al.* (1992) conducted a numerical simulation of the conjugate direct cooling of a micro heat-generating element. The computation was performed using a domain decomposition technique, in which the calculation domain was divided into several zones. It was shown that the temperature of the heating element was mainly controlled by the heat conduction in the substrate near the heating element while the heat transfer to the cooling fluid required a much broader area of the substrate than the size of the heating element. The heat transfer from the substrate to the fluid agreed with the conventional forced convection correlation of the forced convective heat transfer, but the local conduction-dominated cooling, which determines the peak temperature rise in the system, was relatively unaffected by the coolant flow.

Knight *et. al.* (1992[a]) presented a heat sink optimization with application to micro-channels. The equations governing the fluid dynamics and combined conduction/ convection heat transfer in a heat sink were presented in non-dimensional form for both laminar and turbulent flows. A scheme presented for solving these equations enabled the determination of heat sink dimensions that display the lowest thermal resistance between the hottest portion of the heat sink and the incoming fluid.

Numerous review papers had been published with regard to the emerging trend of micro-electro-mechanical systems (MEMS) in latest technology. Gravesen *et al.*

(1993) presented an overview of the research activities in the field of fluid components or systems built with micro-fabrication technologies. Focus is made on the fluidic behaviour of the various devices, such as valves, pumps and flow sensors, as well as the possibilities and pitfalls related to the modeling of these devices using simple flow theory.

Another group of researchers, Arkilic, Breuer and Schmidt (1994) studied the effects of the slip velocity on the mass flow predictions of the Navier-Stokes equations, and compared them with experimental results. The governing flow equations used in this study included the Navier-Stokes equations, the mass continuity equation, and the equation of state, along with slip-flow boundary conditions. The momentum balance at the boundary wall was used to show that the slip-velocity is a function of the velocity gradient near the wall. They showed that for large Knudsen number flows; the flow in micro-passages may be modeled more satisfactorily with the use of slip-flow boundary conditions.

Tien *et. al.* (1994) addressed the challenges in micro-scale conductive and radioactive heat transfer and recommended specific directions for future research. Challenging micro-scale heat transfer was illustrated with their applications in cryogenic systems, thin processing and the operation of electronic, optical, photo-electronic devices, and quantum structures.

Ho and Tai (1994) gave a review on MEMS and its impact on science and technology. A review on its fabrication techniques was also presented. Besides that, the importance of non-dimensional scaling in MEMS research was illustrated.

Beskok *et. al.* (1994) presented a time-accurate computational model based on the slip-flow theory to simulate momentum and heat transfer transport phenomena in complex micro-geometries, encountered in typical components of micro-devices such

as micro-capillaries, micro-valves, micro-rotors and micro-bearings. Their work presented an extension to the classical Maxwell/Smoluchowski slip conditions (for gases) to include high-order Knudsen number effects as well as to take into account the coupling of momentum and heat transfer through thermal creep and viscous heating effects. The numerical method was based on the spectral element technique and validation of the method was obtained by comparison of the numerical simulation results in simple channel slip-flows with analytical results. Reduction of pressure drop in micro-channels and the effect of compressibility were investigated. The effect of slip-flow on skin friction reduction and associated increase in mass flow rate and the variation of normal stresses were investigated as a function of Knudsen number too.

Yeung, Yuen & Zohar (1995) analyzed a system of micro-channels by solving numerically a 3-D heat transfer problem consisting of both the solid substrate and the fluid regions, allowing the introduction of localized heat sources distributed on the chip surface. They pointed out that, the heat sources in real electronic chips were concentrated in few spots; hence a uniform heat flux at the boundary cannot be considered as a good model.

Goodson *et. al.* (1995) proposed a novel cooling system for high-power laser-diode arrays, for which the maximum optical output power density per unit surface area is limited by the temperature rise due to self-heating. The proposed system used a micro-channel heat sink made of chemical-vapor-deposited (CVD) diamond, whose high thermal conductivity increases the efficiency of the channel-wall fins and reduces the array-to-coolant thermal resistance. The thermal resistance was further reduced by minimizing the separation between active regions and the diamond using epitaxial lift-off (ELO) and grafting technology. The array-to-coolant thermal resistance was calculated using a simple model for the combined conduction and convection problem



to be 75% less than that for a conventional configuration using a silicon microchannel heat sink.

Eringen *et. al.* (1995) presented a non-local lubrication theory of fluids with microstructure to provide a basic theory for calculating the rate at which a thin film drains from between two molecularly smooth, solid surfaces as they are forced together. The viscosity modular was in agreement with experiments for all film thickness. Exact solutions were obtained for drainage curves and for the spread of thin films on a rotating surface.

Rujano *et. al.*, (1995) conducted an analysis and computation of conjugate heat transfer in trapezoidal micro-channel heat sinks in a silicon substrate. The effects of the channel aspect ratio, channel spacing, Reynolds number variations and heat source location on the hydraulic and thermal performance of the device were investigated. Results suggested a better thermal performance for the rectangular channel when compared to the trapezoidal geometry and the existence of optimum channel geometry for a given operational condition.

The manifold microchannel (MMC) heat sink has been shown by Copeland (1995) to be an effective way of reducing the maximum heat source temperature and significantly reducing heat source variation. The MMC heat sink differs from a traditional micro-channel (TMC) as first proposed by Tuckerman and Pease (1981) in that the flow length is greatly reduced to a small fraction of the total length of the heat sink. In other words, the MMC heat sinks feature many inlet and outlet channels, alternating at a periodic distance along the length of the micro-channels while the TMC heat sink features one inlet and outlet channel each located at the opposite ends of the chip length. Copeland (1995) performed an analytical study of MMC; heat sinks having between 8 and 32 manifold channels per centimeter of chip length.

Fluorocarbon liquid was used as the coolant, and the micro-channel depth was fixed at one-fourth the manifold channel length. Copeland et al (1995) then experimentally tested a variety of manifold micro-channel with channel widths of 57 and 113  $\mu\text{m}$ . The micro-channel depth and wall thickness were varied, as well as the number of manifold channels. Generally, the measured convective thermal resistance was lower than predicted, with the experimental dependence on flow rate considerably stronger than predicted. Copeland (1995) compared analytical and numerical studies of a MMC heat sink. A geometry with a channel width of 57 $\mu\text{m}$  depth of 200 $\mu\text{m}$  and length of 1000 $\mu\text{m}$  was chosen. The commercial finite volume CFD code, Fluent, Version 4.3.1 was used for both isothermal and conjugate numerical studies. Copeland et al (1997) continued the study by conducting an experimental study of manifold micro-channel heat sinks for forced air-cooling. The thermal resistance was found to be strongly affected by the micro-channel width, the number of manifold inlet/outlet channels and the pumping power, but weakly by micro-channel wall-thickness-ratio and micro-channel depth cooperated with manifold inlet/outlet channel width.

Navier-Stokes based computational fluid dynamics (CFD) techniques are often inaccurate when applied to micro-electromechanical systems (MEMS). This inaccuracy stems from their calculation of molecular transport effects, such as viscous dissipation and thermal conduction, from bulk flow quantities, such as mean velocity and temperature. This approximation of micro-scale phenomena with macro-scale information fails as the characteristic length of the flow gradients ( $\Lambda$ ) approaches the average distance traveled by molecules between collisions (the mean free path), the ratio of these quantities is known as the Knudsen number,  $\text{Kn} = 1/\Lambda$  and is used to indicate the degree of flow rarefaction. For  $\text{Kn} < 0.01$ , the flow is considered to be in

the 'continuum' regime and the Navier-Stokes equations are applicable in their common form. As  $Kn$  increases, the flow moves through the 'slip-flow' ( $0.01 < Kn < 0.1$ ) and 'transition' ( $0.1 < Kn < 3$ ) regimes and finally enters the 'free-molecular' ( $Kn > 3$ ) regime with each suggesting a particular type of analysis.

Piekos and Breuer (1996) made use of the direct simulation Monte Carlo (DSMC) method for simulations of micro-channels and unlike previous analytical and computational investigations where the results were based on the Navier-Stokes equations, the DSMC approach is valid for the full range of flow regimes (continuum through free molecular). In the slip-flow regime, the results of Piekos and Breuer are in good agreement with the analytic model and experimental data presented by Arkilic, Schmidt and Breuer (1994). The DSMC method is commonly applied to reentry vehicles and it makes no continuum assumption. Instead it models the flow, as it physically exists: a collection of discrete particles, each with a position, a velocity, an internal energy, a species identity etc. These particles are moved and allowed to interact with the domain boundaries in small time steps during the calculation. Intermolecular collisions are all performed on a probabilistic basis at the end of each time step to minimize computational work. Macroscopic quantities such as flow speed and temperature are then obtained by sampling the microscopic state of all particles in the region of interest. The DSMC method has proven to be a valuable tool for investigating the behavior of flows, which are considered 'rarefield' due to miniaturization.

Beskok *et. al.* (1996) studied the effects of rarefaction and compressibility in gas micro-flows. They concluded that rarefaction negates compressibility. They also demonstrated that compressibility for shear-driven flows is negligible and rarefaction

dominates. Finally, they proposed a set of benchmark experiments designed to validate the slip-flow theory in modeling micro-flows.

Baker *et. al.* (1996) investigated the impact of temperature dependent viscosity on heat and momentum transfer characteristics in gaseous micro-channel flows. The model problem presented, coupled the momentum and energy equations through the use of Sutherland's model for dynamic viscosity. The model also incorporated the Maxwell/Smoluchowski boundary conditions at the solid-gas interfacial boundaries. Numerical results for flow fields with Knudsen numbers in the slip flow regime were compared with analytical expressions. A parametric study was examined to determine the impact of various dimensionless quantities on velocity and temperature distributions in micro-channel flows. Skin friction coefficients and Stanton numbers were also presented in their analysis.

With the large memory capacity required to handle the number of equations generated by a typical microchannel, Kendall and Rao (1996) presented a finite difference formulation for the integration of the Navier-Stokes equations for the flow through a microchannel by using a 'block system' of solution for the simultaneous equation generated. The 'block system' of solution based on the Navier-Stokes equations for flow through micro-channels allowed several advantages:

1. Optimization of memory requirements for the computation depending on channel dimensions and available computer memory.
2. Making the aspect ratio as near to unity resulting in minimal truncation and rounding off errors.

Kendall and Rao (1997) performed both computational and experimental investigation of the flow characteristics in micron sized passages to establish the relationship between Reynolds number (compressibility) and the friction factor. They

found that the friction factors obtained using the traditional correlation ( $f = 24/Re$ ) were found to be consistently lower than their experimental and computational counterparts. The traditional method assumes fully developed, 1-dimensional, incompressible flow with zero lateral velocity. They also observed a higher sensitivity to the compressible nature of the fluid for lower Reynolds number.

Jayakanthan *et. al.* (1997) used the commercial CFD code (FLUENT) to simulate the thermal performance of a single electronic package as a conjugate heat transfer problem under various air cooling conditions. Prediction of junction temperature and junction to ambient thermal resistance, compared well with available experimental measurements. The heat transfer coefficients, which are required for the simulation of the electronic package by conduction modes, were also determined.

Tso *et. al.* (1998) proposed the Brinkmann number as a parameter for correlating the convective heat transfer parameters in micro-channels. The proposal originates from a dimensional analysis of the variables influencing the laminar liquid flow convection in micro-channels.

Ho and Tai (1998) gave an updated comprehensive review on fluid flow in MEMS. They outlined the need to re-examine the effect of surface forces in the momentum equation. They also noted that the non-slip boundary condition should be relaxed for gas flows. Molecular dynamics approach is recommended as a means by which micro-fluidic problems can be investigated.

Poh and Ng (1998 & 1999) presented a CFD approach in analyzing the fluid flow and heat transfer in MMC. The commercial CFD code ANSYS/FLOTTRAN was used to generate various test stimulations under varying conditions. Comparisons were made with a derived analytical model and also simulations using the FLUENT

software. Further comparisons were also made regarding the relationship between the Reynolds number and the friction factor.

Ng and Liu (2002) study the effect of the size of time step in the application of direct simulation Monte Carlo (DSMC) method for rarefied gas dynamics. The computational domain used in the study is shown in Figure 2.2. It is found that some wall properties related to the streamwise derivative of velocity, such as wall shear stress, are sensitive to the size of time step. A series of computation and analysis is presented to illustrate the computational errors (bias) caused by the size of time step and the corresponding computational resource applied. From this investigation, a compromise can be made between the magnitude of error and computing cost; thus, a criterion on the size of time step is proposed for the DSMC method. This criterion is necessary for the application of DSMC method used in low subsonic, ultra-thin gas film lubrication with a characteristic scale of one mean free path, such as the gas bearing flow under the floating slider. In the paper, the limitation of time interval was stated as

$$\Delta t < \frac{\Delta x}{c} \quad (2-1)$$

where  $\Delta t$ ,  $\Delta x$  and  $c$  represent the size of time step, the size of cell in streamwise direction and the most probable molecular velocity respectively. A total of nine cases are investigated from  $\Delta t < 4 \times 10^{-12} s$  to  $\Delta t < 60 \times 10^{-12} s$ .

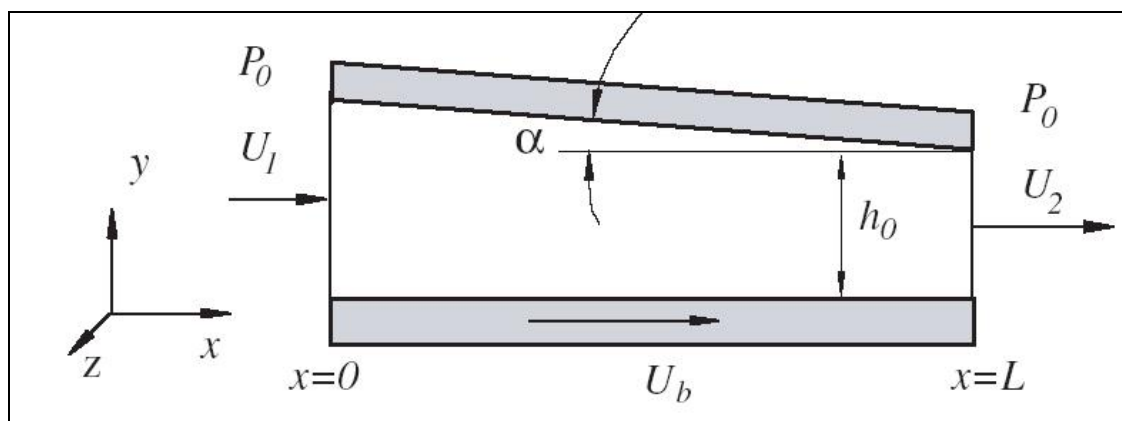


Figure 2.2 Computational domain used by Ng and Liu (2002)

### 2.2.2 Models with EDL effect

According to Mala, Li and Dale (1997), one possible explanation on the properties deviations of micro-scale flow from macro-scale flow is that they are largely due to the interfacial electric double layer (EDL), which is negligible and being ignored in macroscale fluid mechanics. In reality, most solid surfaces have electrostatic charges i.e. an electrical surface potential. If the liquid contains very small amount of ions, the electrostatic charges on the solid surface will attract the counterions in the liquid to create an electrical field. The arrangement of the electrostatic charges on the solid surface and the balancing charges in the liquid is called the EDL as illustrated in Figure 2.3.

When a liquid is forced through a micro-channel under hydrostatic pressure, the ions in the mobile part of the EDL (diffuse double layer region) are carried towards one end opposite the liquid flow, causing an electrical current (streaming current) to flow in the direction of the liquid flow.

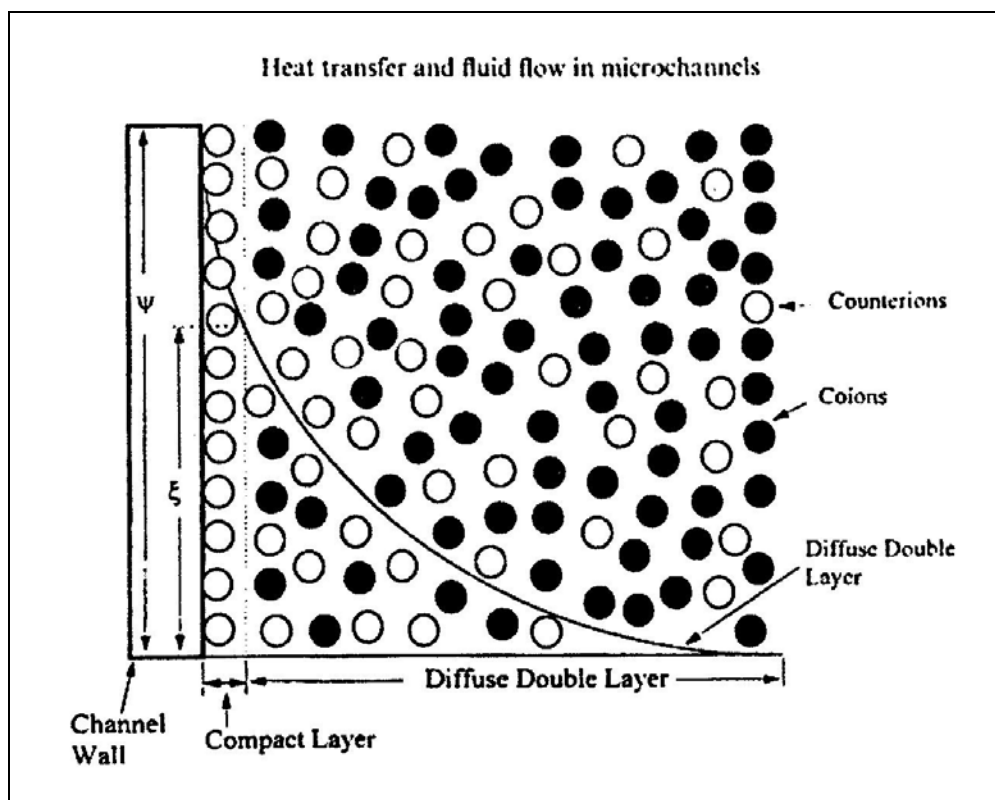


Figure 2.3 Schematic representation of the electric double layer at the channel wall

[Mala et al. (1997)]

Mala et al. found that the EDL and the streaming potential act against the liquid flow resulting in a higher apparent viscosity. This in turns results in a reduced flow velocity than in conventional theory, thus affecting the temperature distribution and reducing the Reynolds number. In macroscale flow, these interfacial electrokinetic effects are negligible as the thickness of the EDL is negligible compared to the hydraulic radius of the flow channel unlike as in microscale flow. In other words, for small electrokinetic separation distance  $\kappa$  (where in channel flow  $\kappa$  is distance between opposite walls of the channel), the EDL have a significant effect on liquid flow, while for larger  $\kappa$ , the influence is predominant only at a region near the channel wall. A simple 2-D fully developed flow model (shown in Figure 2.4) was used. In this work,



the highly non-linear term, charge density,  $\rho_e$  is linearized using Debye-Huckle linear approximation.

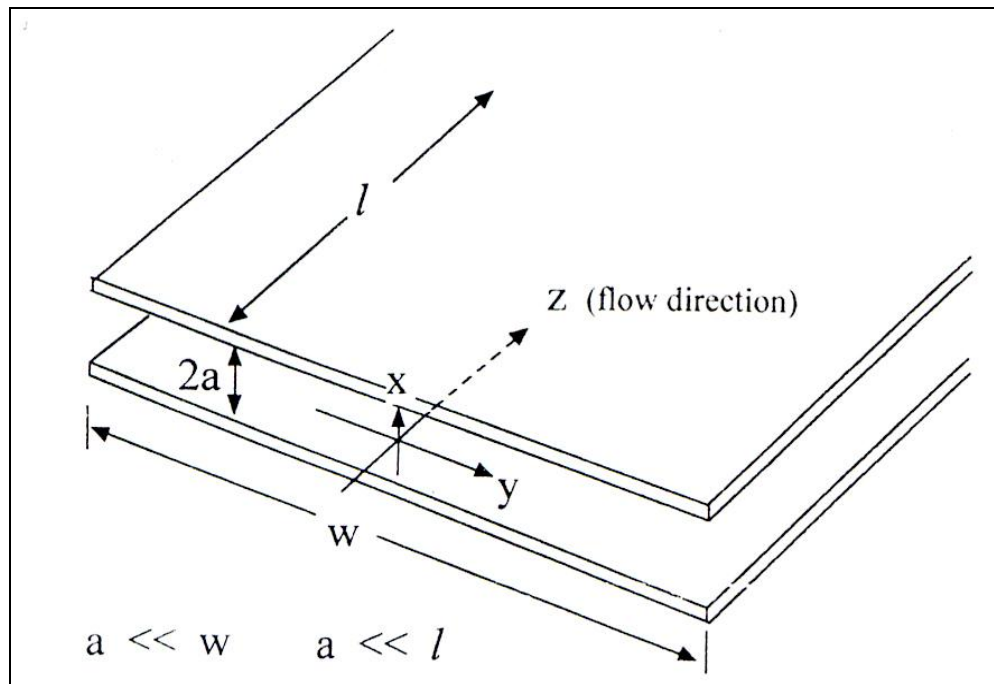


Figure 2.4 Flow model used by Mala *et. al.* (1997)

In another paper published by Mala, Yang and Li (1998), the above model was solved both analytically, using Debye-Huckle linear approximation, and numerically, without any assumption. It was found that the linear solution might significantly overestimate the electrical potential near the channel wall and in the corner regions, except for small zeta potential cases. By definition, the zeta potential is a measurable electrical potential at the shear plane, i.e., the boundary between compact layer and the diffuse layer in EDL theory [Hunter (1981)].

Yang and Li (1997) extended the model developed by Mala et al (1997) to a 3-D dimensional fully developed flow (as shown in Figure 2.5). A 2-D Poisson-Boltzmann equation was used to model the electrical potential distribution. Green function is used to solve the 2-D partial differential equation. In 1998, based on the same flow model, Yang and Li applied Debye-Huckle linear approximation, and an

analytical solution was obtained to describe the distribution of electrical potential, an exact solution to the modified NS equation in rectangular microchannel is obtained.

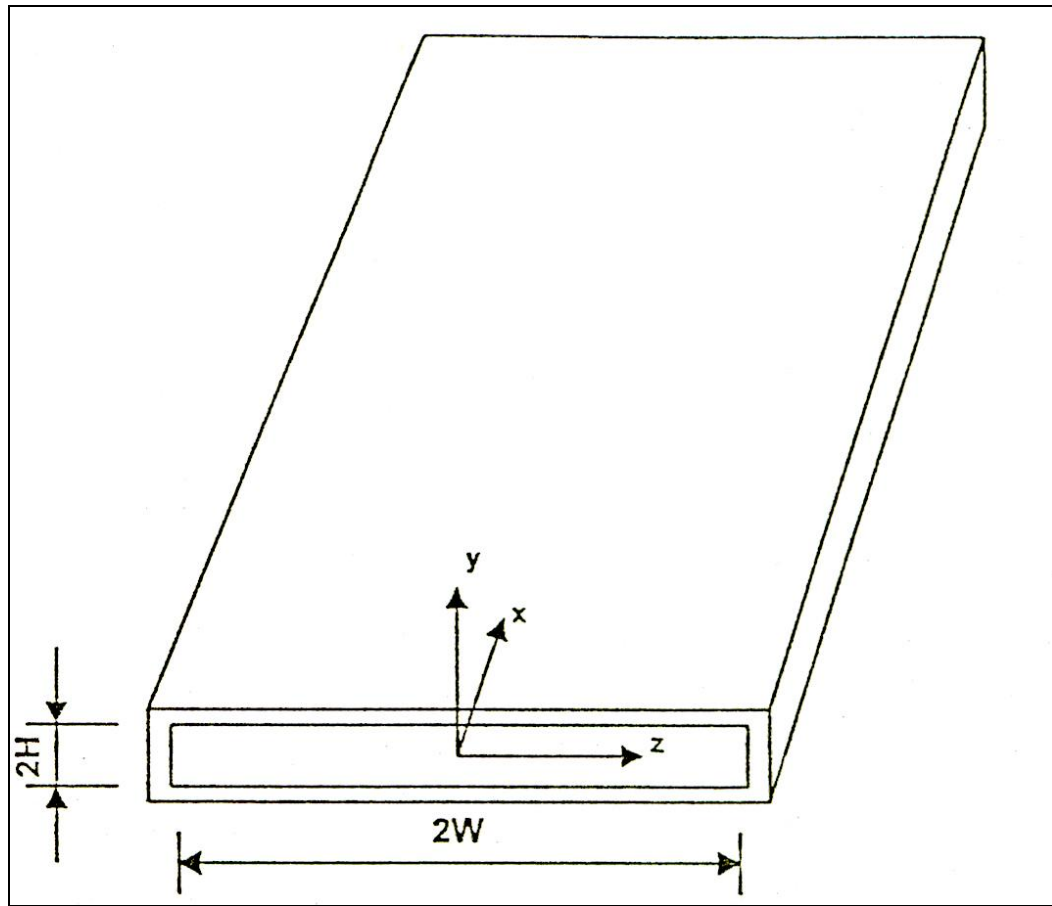


Figure 2.5 Flow model used by Yang and Li (1997)

Yang et al. [Yang, Li and Masliyah (1998)] reported a study very similar to Yang and Li (1997). In this study, symmetric boundary condition was applied (as shown in Figure 2.6).

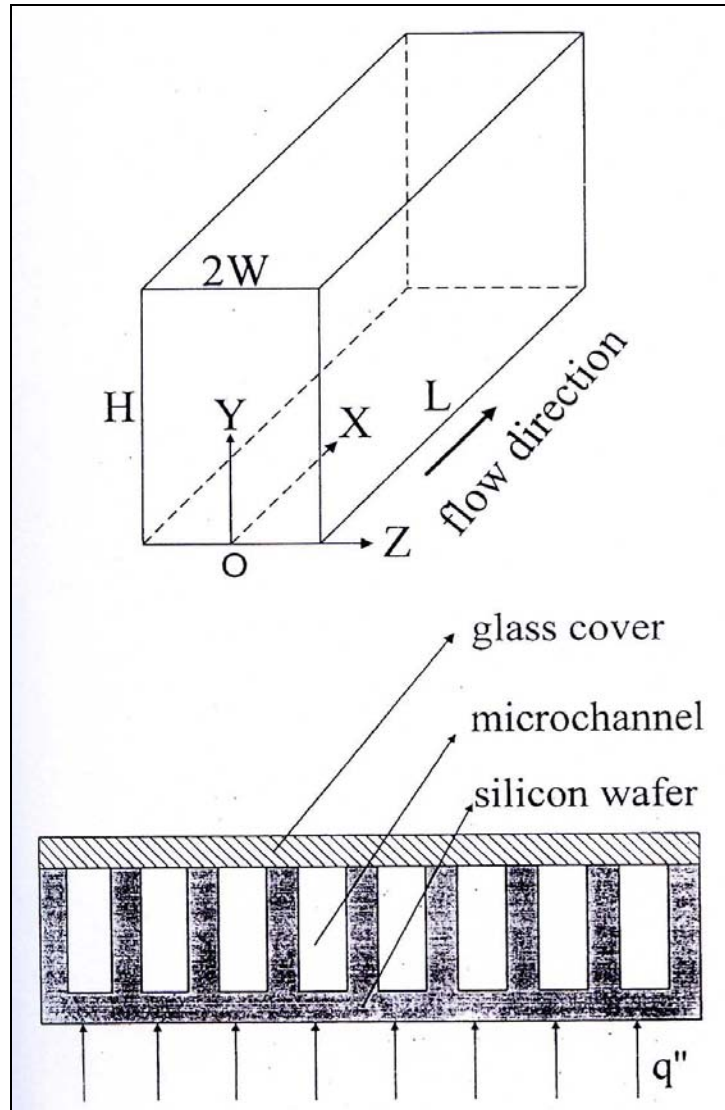


Figure 2.6 Flow model used by Yang, Li and Masliyah (1998)

Lower concentration such as  $10^{-6}$  and  $10^{-8}$  was used in this study as it was found in Yang and Li (1997) that, the electrical potential profile can extend to a much larger portion of the channel in lower concentration solution. The energy equation for the rectangular microchannels was constructed and the temperature field in the microchannel was predicted. In their paper, the validity of Boltzmann distribution of ion concentration was examined. It was found that only for a microchannel flow with a very small Peclet number or in a fully developed hydrodynamic state, the Boltzmann distribution could be safely applied.

Ng and Poh (2000a and 2000b) analyzed the EDL effect on microchannel based on the 2-D model as shown in Figure 2.7

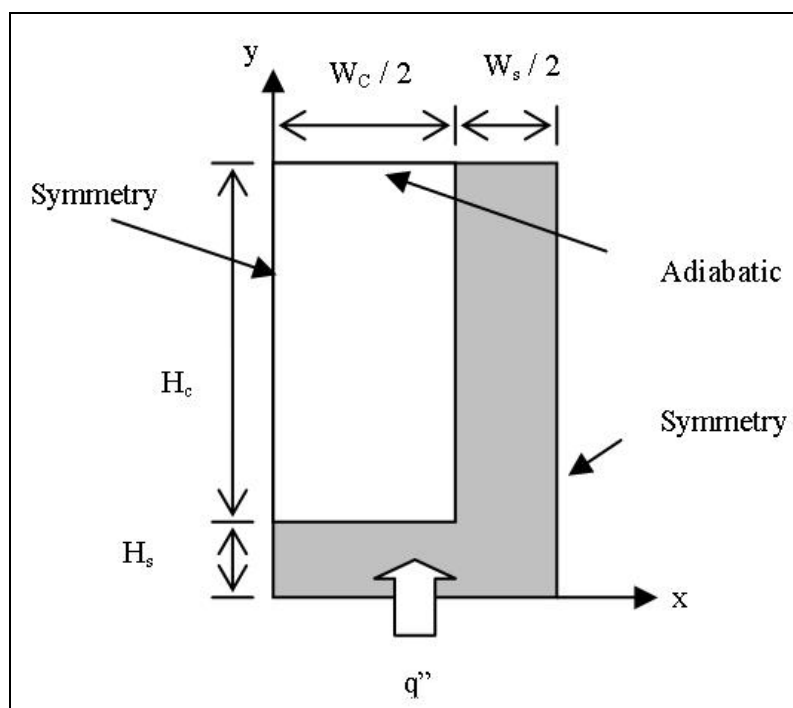


Figure 2.7 The physical model of the microchannel

It was found that the presence of the EDL reduces the liquid velocity within the channel, which affects the heat transfer mechanism in the pressure-driven microchannels. Maximum gradient of velocity profile was associated with the highest gradient of the EDL potential profile. The numerical parametric studies performed allowed the conclusion that the microchannel flows subjected to EDL is dependent on various factors. The electric field strength has a major influence on the electro-osmotic flow across the microchannel as the result of a tangentially applied electric field on a channel with the existing of an EDL. The presence of the EDL is more significant as aspect ratios decreases (i.e. the corner effects play a larger role on the development of the EDL field and thus on the velocity profiles). Also, the friction coefficient increases as the ionic concentration of the aqueous solution decreases and Zeta potential of the system increases.

Ng and Poh (2001) extended their works on microchannel from one layer to two layers. It was found that for the same dimension (Height of  $20\mu\text{m}$ , Width of  $30\mu\text{m}$ ), the nondimensional thermal resistance for double layer (0.1124) is significantly lower than that of single channel (0.2961).

Yang et al [Yang, Fu and Lin (2001)] studied EDL effect on microchannel flow, at entry (developing) region. A 2-D flow field was used and an extra-applied electrostatic field,  $\phi$  was applied to the flow field as another driving force. The physical model used is shown in Figure 2.8.

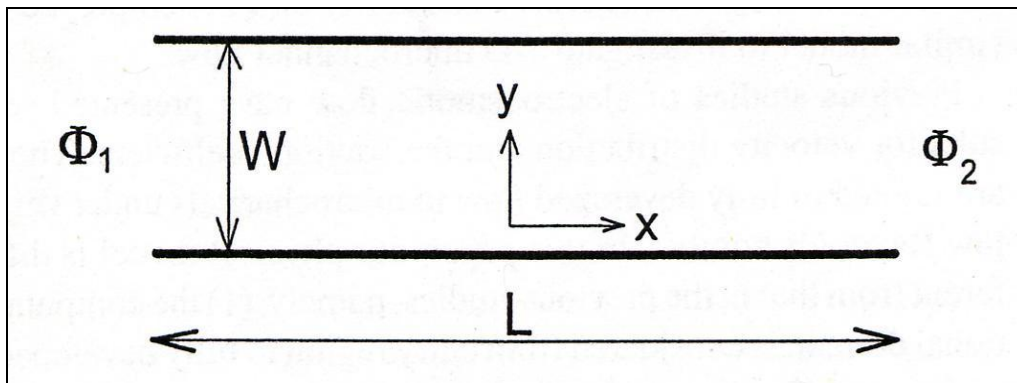


Figure 2.8 Flow model used by Yang, Fu and Hwang (2001)

For simplicity, two assumptions were made. 1) The electrical potential was assumed to be Boltzmann distribution and 2) Debye-Huckel linear approximation was applied. It was found that generally, the EDL near the channel wall tends to restrict the motion of the ions and, hence, the liquid molecules in the diffuse EDL region. The effects of the EDL field and the applied electric field on the fluid velocity distribution, pressure drop and skin friction were summarized as:

(1) The driving force of the electroosmotic flow comes from the interaction between the applied electrostatic field and the EDL. The force is non-uniform across the channel height, which is different from the classical theory for fully developed channel flows. This force is dominant next to the channel walls and may be negligibly small in

the central region of the channel, depending on the thickness of the EDL. This force drives the fluid next to the channel walls, resulting in fluid motion in the central region as a result of viscous drag force.

(2) In the prediction with EDL effect, the gradient of velocity of the fluid was found to be larger than that without EDL effect, which is due to larger net viscous drag force. Hence results in an increase of pressure drop and skin friction.

(3) Although the pressure drop is not the major driving force in the electroosmotic flow, it must have its own right to exist along the channel. Therefore, the pressure gradient term should be kept in the momentum equations for the general electroosmotic flow physics. The pressure distribution normal to channel walls is shown to be non-uniform due to the influence of the EDL.

Calculations with and without convection terms in the Navier-Stokes equations were also preformed. For the parallel flat case, when the Reynolds number is small, the computed velocity distributions are nearly flat in the fully developed region. However, for larger Reynolds numbers, the velocity profile has concave shape in the fully developed region. For the 90° bend case, a separation bubble is detected near the 90° turn. Therefore, the inertial effect can impact the velocity distributions of the electroosmotic flow, when the Reynolds number is large.

Yang et al [Yang, Fu and Hwang (2001)], further solved the same model developed by Yang, Fu and Lin (2001) without using assumption of Boltzmann distribution for electrical potential. Two extra partial differential equations named Nernst-Planck equation, based on the principle of conservation of charge, were used to described the distribute concentration and positive and negative ion,  $n^+$ ,  $n^-$ . The effect of entry region on the fluid velocity distribution, charge density boundary layer, entrance length and shear stress were discussed. Three important findings were

mentioned: 1) the entrance length was found to be longer than that of classical pressure-driven flow, 2) the thickness of the EDL in the entry region is thinner than that in the fully developed region, 3) The change of velocity profile was apparent in the entrance region, and the axial velocity profile is no longer flat across the channel height when the Reynolds number was large.

Fu *et al.* (2002) extended the above approved [Yang, Fu and Lin (2001)] to model an injection system in microfluidic chip. The work addressed the design and testing of injection systems with a variety of configurations, including a simple cross, a double-T and triple-T configuration. The paper also presented the design of a unique multi-T injection configuration (as shown in Figure 2.9). Each injection system cycles through a predetermined series of steps, in which the electric field magnitude and distribution within the various channels was strictly manipulated, to effectuate a virtual valve. The proposed design successfully combines several conventional injection systems within a single microfluidic chip.

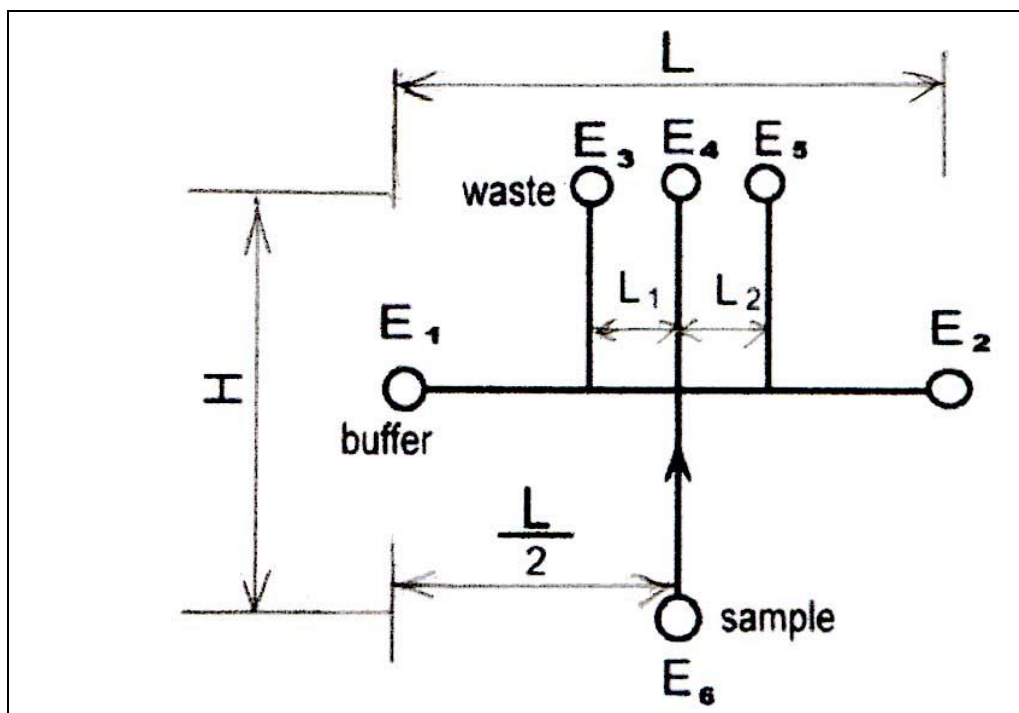


Figure 2.9 Model for unique multi-T injection configuration [Fu *et al.* (2002)]

Ng and Poh (2002a and b) studied the flow and heat transfer characteristics of microchannels for developed 2-D flow field, with different bulk ionic concentration, zeta potential and the aspect ratio of the channel.

Obot *et al* (2002) presented a critical review of published results to provide a better understanding of microchannel transport phenomena, together with the framework for future research. His main findings included: the onset of transition to turbulent flow in smooth microchannels does not occur if the Reynolds number is higher than 1,000; the Nusselt number varies as the square root of the Reynolds number in laminar flow; and, satisfactory estimate of transfer coefficients, within the accuracy of experimental errors, can be obtained by using either experimental results for smooth channels with large hydraulic diameter or conventional correlations.

Fu et al [Fu, Lin and Yang (2003)] extended the work by Yang et al [Yang, Fu and Lin (2001)] by step change in zeta potential (as shown in Figure 2.10). In this study, the full Navier-Stokes equation and the Nernst-Planck equation were used to model the change in EDL characteristic that occur when a step change in zeta potential was applied. It was found that the thickness of the EDL gradually increases downstream from the location at which the zeta potential was increased. The results indicated that a step change in the zeta potential causes a significant variation in the velocity profile and in the pressure distribution.



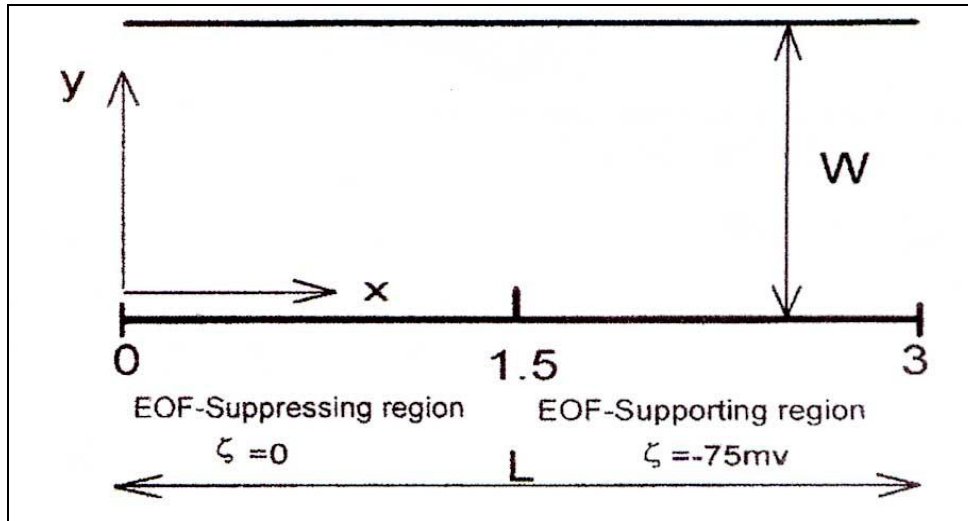


Figure 2.10 Flow model used by Fu et al (2003)

However the study on full 3-D developing flow with EDL effect through microchannel was only found in Tan and Ng (2003). It is important to investigate this as 3-D flow gives a better insight to the real flow field and, the developing flow region is more effective than the fully developed flow region from the view point of heat transfer. Ng and Tan (2004) further presented the effects of the charge density on the 3-D flow field including developing region. Results comparing the performances of the microchannel under different factors such as Reynolds number, nondimensionalized electric potential etc are shown and discussed. Nusselt numbers for each case such as with or without EDL effect are also included; so that the actual effectiveness of the micro-channel can be understood.

Tardu (2004.) investigated the EDL effect on the stability of microchannel flow. It was shown that the EDL destabilizes the Poiseuille flow considerably. For example, the critical Reynolds number decreases by a factor of five when the nondimensional Debye-Huckel parameter  $\kappa$  is around ten. It was also found that the transition was rapid for microchannels of a couple of microns height in particular when

the liquid contains a very small number of ions. The EDL effect disappears quickly for  $\kappa \geq 150$  corresponding typically to channels of height 400  $\mu\text{m}$  or larger. These results may explain why significantly low critical Reynolds numbers had been encountered in some experiments dealing with microchannel flows.

### 2.2.3 Comparison between current literature and present research work

As shown in section 2.2.2, most of the previous works were based on base 2-D governing equation. With lack of third-dimension, realistic flow field [for example microchannel for DNA separation described by Fu et al (2002a)], which often with, both developing region and aspect ratio which are not equal to infinity or zero, thus can not be studied accordingly. As mention in section 1.1, even for aspect ratio of 0.1, the performance of a rectangular channel such as the friction coefficient,  $fRe$ , is significantly different from that predicted using a 2-D model ( $AR = \text{zero}$ , as shown in Fig. 1.5).

In present research work, with the help of 3-D flow important parameter of microchannel variables such as friction coefficient,  $fRe$  and Nusselt number,  $Nu$  of a realistic microchannel can now be predicted. Hence, the effect of important properties of the flow such as Debye-Huckel parameter,  $\kappa$ , Schmidt Number,  $Sc$  and the entrance length  $L_e$  on the performance of microchannel can be evaluated at ease.

## Chapter Three

### THEORETICAL FORMULATION

#### 3.1 PHYSICAL MODEL

As the focus of this research is on 3D developing flow field, a simple rectangular channel as shown in Figure 3.1 is used as the current physical model for deriving all the theoretical formulation. The coordinate system is set such that the X, Y, Z directions depict the width  $W_c$ , length  $L_c$ , and height  $H_c$  of the rectangular channel respectively. The main stream is along Z-direction. The origin is placed at the mid-width of the rectangular channel and this permits computation to be done on half of the model.

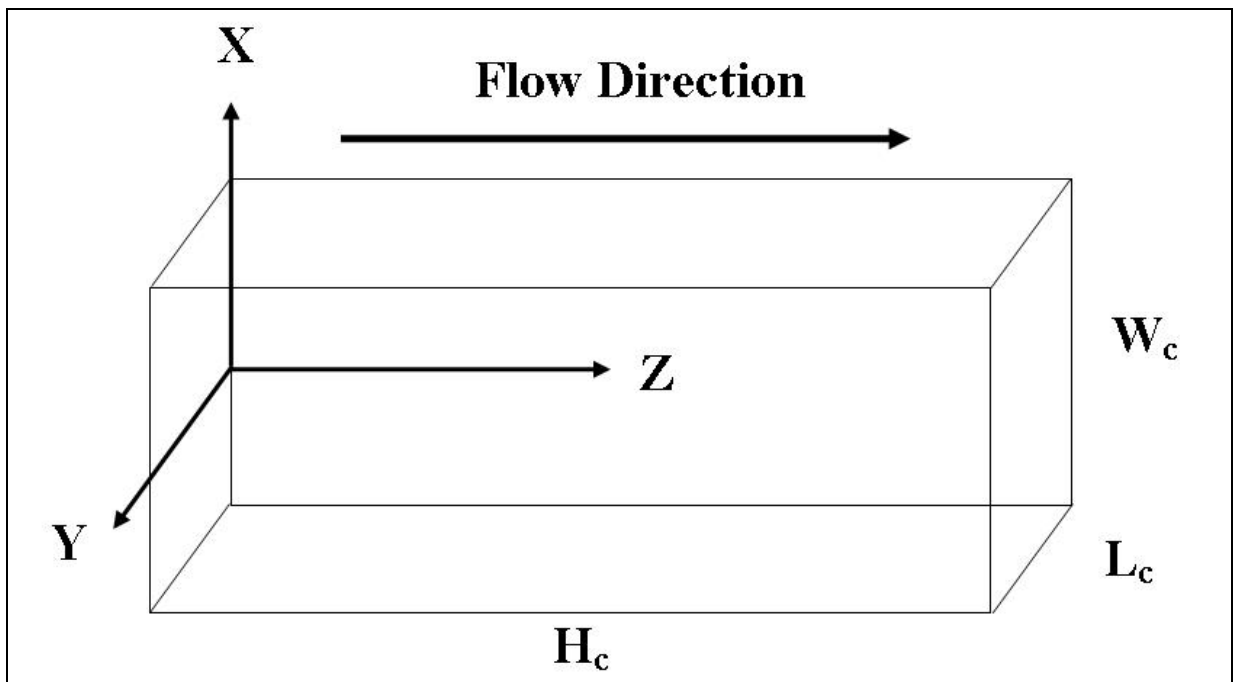


Figure 3.1 Physical model of the research

#### 3.2 ELECTRIC DOUBLE LAYER (EDL)

### 3.2.1 Background

In microscale flow, deviations in trends are likely to be caused by interfacial effects such as the electric double layer (EDL), which has negligible thickness in macroscale flow. The EDL model used in this project based on the model described by Mala *et. al.* (1997a).

Most solid surfaces have electrostatic charges i.e. an electrical surface potential. If the liquid contains very small amounts of ions, the electrostatic charges on the solid surface will attract the counterions in the liquid to establish an electrical field. The arrangement of the electrostatic charges on the solid surface and the balancing charges is called the EDL. Because of the electrical field, the ionic concentration near the solid surface is higher than that in the bulk liquid. In compact layer, which is about 0.5 nm thick, the ions are strongly attracted to the wall surface and are immobile. In diffuse double layer, the ions are affected less by the electrical field and are mobile. The thickness of the diffuse EDL ranges from a few nanometers up to several hundreds of nanometers, depending on the electric potential of the solid surface, the bulk ionic concentration and other properties of the liquid. When a liquid is forced through a microchannel under hydrostatic pressure, the ions in the mobile part of the EDL are carried towards one end. This causes an electric current, called streaming current, to flow in the direction of the liquid flow. The accumulation of ions downstream sets up an electrical field with an electrical potential called the streaming potential. This field causes a current, called conduction current, to flow back in the opposite direction. When conduction current is equal to the streaming current a steady state is reached. It is easy to understand that, when the ions are moved in the diffuse double layer, they pull the liquid along with them. However, the motion of the ions in the diffuse double

layer is subjected to the electrical potential of the double layer. Thus the liquid flow and heat transfer are affected by the presence of the EDL. In macroscale flow, these interfacial electrokinetic effects are negligible as the thickness of the EDL is negligible compared to the hydraulic radius of the flow channel. However, in microscale flow the EDL thickness is comparable to the hydraulic radius of the flow channel. For submicron capillaries the EDL thickness may even be larger than the radius of the capillary. Thus EDL effects must be considered in the studies of microscale flow and heat transfer.

Here, the effects of EDL at the solid-liquid interface on fluid flow and heat transfer through a microchannel is investigated. The solution of the Poisson-Boltzmann equation is used to describe the EDL field. The addition of the electrical body force, resulting from the double layer field, to the equation of motion results in a modified velocity distribution upon solving for steady state flow.

### 3.2.2 Mathematical formulation for electrical potential distribution

As the model is symmetric (as mention in section 3.1), only the electric field will only half of the model will be used to predict the electrostatics field. According to the theory of electrostatics, the relationship of the electrical potential,  $\Psi$ , and the net charge density per unit volume,  $\rho_e$  at any position at steady state, is given by the 3-D

Poisson's equation :

$$\left(\frac{\partial^2 \Psi}{\partial X^2} + \frac{\partial^2 \Psi}{\partial Y^2} + \frac{\partial^2 \Psi}{\partial Z^2}\right) = -\frac{\rho_e}{\epsilon \epsilon_o} \quad (3-1)$$

where  $\varepsilon$  (=80 for water) is the relative dielectric constant of the medium and  $\varepsilon_0$  (=8.854x10<sup>-12</sup> CV<sup>-1</sup>m<sup>-1</sup>) is the electric permittivity of a vacuum.

Using the following nondimensional term:

$$x = \frac{X}{D_h} \quad y = \frac{Y}{D_h} \quad z = \frac{Z}{D_h} \quad \psi = \frac{z_i e \Psi}{k_b T_{in}} \quad \text{and} \quad D_h = \frac{4L_c W_c}{2(L_c + W_c)}$$

where  $x$  is the nondimensional  $X$ -coordinate,  $y$  is the nondimensional  $Y$ -coordinate,  $z$  is the nondimensional  $Z$ -coordinate,  $D_h$  is the hydraulic diameter of the channel and  $\psi$  is the nondimensional electrostatic potential. The nondimensional form of the 3-D Poisson-Boltzmann (PB) equation can be rewritten as:

$$\frac{\partial^2 \psi}{\partial x^2} + \frac{\partial^2 \psi}{\partial y^2} + \frac{\partial^2 \psi}{\partial z^2} = -\frac{\rho_e}{2n_o z_i e} \frac{2n_o z_i^2 e^2 D_h^2}{\varepsilon \varepsilon_0 k_b T_{in}} \quad (3-2)$$

where

$z_i$  is valence of ions,  $k_b$  is Boltzmann's constant (1.3805x10<sup>-23</sup> J<sup>1</sup>K<sup>-1</sup>),  $T_{in}$  is absolute temperature of fluid at inlet of microchannel (K),  $e$  is electron charge (1.6021x10<sup>-19</sup> C),  $n_o$  is bulk concentration of ions.

As the net volume charge density  $\rho_e$  is proportional to the concentration difference between cations and anions, therefore

$$\rho_e = (n^+ - n^-) z_i e \quad (3-3)$$

where  $n^+$  and  $n^-$  are concentration of cations and anions respectively.

Hence

$$\frac{\partial^2 \psi}{\partial x^2} + \frac{\partial^2 \psi}{\partial y^2} + \frac{\partial^2 \psi}{\partial z^2} = -K^2 \frac{(n^+ - n^-)}{2n_o} \quad (3-4)$$

where

$$K = D_h \kappa$$

$\kappa = \left( \frac{2n_o z_i^2 e^2}{\epsilon \epsilon_o k_b T_{in}} \right)^{\frac{1}{2}}$ , is Debye-Huckel parameter ( $1/\kappa$  is normally referred as the EDL thickness).

As shown in equation 3-4, a full formulation of governing equations should also include the mass transfer equation for each type of ions in the system (i.e. cations,  $n^+$  and anions,  $n^-$ ).

### 3.2.3 Nernst-Planck (NP) equations

Generally, the ionic concentration distribution  $n$ , is described by the Nernst-Planck equation [van de Ven (1989)], which under steady-state conditions and in the absence of source terms can be expressed in the convective-diffusion form

$$\nabla \bullet (D_i \nabla n_i) - \nabla \bullet (\vec{V}_i n_i) = 0 \quad (3-5)$$

where  $D_i$  is the diffusion coefficient of the type- $i$  ion and  $\vec{V}_i$ , is the velocity vector of the type- $i$  ion. Under such a situation, the ion velocity  $\vec{V}_i$ , can be decomposed into contributions from hydrodynamic velocity vector  $\vec{V}$  and a velocity vector  $\vec{u}_i$ , due to the electrostatic field acting on the ion (caused by the presence of the EDL field). Then one can write

$$\vec{V}_i = \vec{V} + \vec{u}_i \quad (3-6)$$

The velocity  $\vec{u}_i$ , is related to the electrostatic force exerting on the ions by the following equation

$$F_{ei} = z_i e E = f_i \vec{u}_i \quad (3-7)$$

where  $z_i$  is the valence of the type- $i$  ion,  $e$  is the elementary charge,  $E$  is the electrostatic field strength, and  $f_i$  is the hydrodynamic resistance coefficient. Noting that  $E$  is given by

$$E = -\nabla \psi \quad (3-8)$$

where  $\psi$  is the electrical potential and the hydrodynamic resistance coefficient  $f_i$  can be determined from the Stokes-Einstein equation

$$f_i = \frac{k_b T}{D_i} \quad (3-9)$$

where  $k_b$ , is the Boltzmann constant and  $D_i$  is the diffusion coefficient of the type- $i$  ion, one can readily show that the velocity  $u$ , can be expressed by

$$\vec{u}_i = -\frac{z_i e D_i \nabla \psi}{k_b T} \quad (3-10)$$

Substituting equations 3-8 and 3-10 into equation 3-5, and using  $\nabla \bullet \vec{V} = 0$ , yields

$$\nabla^2 n_i - \frac{\vec{V}}{D_i} \bullet \nabla n_i + \nabla \bullet \left( \frac{z_i e n_i}{k_b T} \nabla \psi \right) = 0 \quad (3-11)$$

The equation 3-11 can be non-dimensionalized as

$$\nabla^2 \bar{n}_i - Pe \cdot e_v \bullet \nabla \bar{n}_i + \nabla \bullet \left( \frac{z_i e \bar{n}_i}{k_b T} \nabla \bar{\psi} \right) = 0 \quad (3-12)$$



where  $\bar{n}_i$  is the non-dimensional ionic concentration  $\bar{n}_i = \left( \frac{n_i}{n_{io}} \right)$  (here  $n_{io}$  is the bulk concentration of the type- $i$  ion),  $Pe$  is the Peclet number  $Pe = \left( |\vec{V}| D_h / D_i \right)$ ,  $e_v$  is the unit vector along the hydrodynamic velocity  $\vec{V}$  direction.

For flow field with two types of charge (one for positive and negative charge respectively), the Nernst-Planck equations, which are applied to model the distribution of the concentration of charge particle based on the conservation law for cations and anions, are written as [Yang et al (1998)]

$$\begin{aligned} & \frac{\partial \left( \bar{u} \bar{n}^+ \right)}{\partial x} + \frac{\partial \left( \bar{v} \bar{n}^+ \right)}{\partial y} + \frac{\partial \left( \bar{w} \bar{n}^+ \right)}{\partial z} \\ &= \frac{1}{Sc^+ Re} \left( \frac{\partial^2 \bar{n}^+}{\partial x^2} + \frac{\partial^2 \bar{n}^+}{\partial y^2} + \frac{\partial^2 \bar{n}^+}{\partial z^2} \right) \\ &+ \frac{1}{Sc^+ Re} \left[ \frac{\partial}{\partial x} \left( \bar{n}^+ \frac{\partial \psi}{\partial x} \right) + \frac{\partial}{\partial y} \left( \bar{n}^+ \frac{\partial \psi}{\partial y} \right) + \frac{\partial}{\partial z} \left( \bar{n}^+ \frac{\partial \psi}{\partial z} \right) \right] \end{aligned} \quad (3-13)$$

$$\begin{aligned} & \frac{\partial \left( \bar{u} \bar{n}^- \right)}{\partial x} + \frac{\partial \left( \bar{v} \bar{n}^- \right)}{\partial y} + \frac{\partial \left( \bar{w} \bar{n}^- \right)}{\partial z} \\ &= \frac{1}{Sc^- Re} \left( \frac{\partial^2 \bar{n}^-}{\partial x^2} + \frac{\partial^2 \bar{n}^-}{\partial y^2} + \frac{\partial^2 \bar{n}^-}{\partial z^2} \right) \\ &- \frac{1}{Sc^- Re} \left[ \frac{\partial}{\partial x} \left( \bar{n}^- \frac{\partial \psi}{\partial x} \right) + \frac{\partial}{\partial y} \left( \bar{n}^- \frac{\partial \psi}{\partial y} \right) + \frac{\partial}{\partial z} \left( \bar{n}^- \frac{\partial \psi}{\partial z} \right) \right] \end{aligned} \quad (3-14)$$

where

$Re$  is  $\left( \frac{\rho_f W_{in} D_h}{\mu_f} \right)$  Reynolds number

Schmidt number is defined as  $Sc^+ = \frac{\mu_f}{\rho_f D_f^+}$  and  $Sc^- = \frac{\mu_f}{\rho_f D_f^-}$  for cation and anion

respectively.  $\bar{n}^+$ ,  $\bar{n}^-$  are dimensionless cation and anion concentration,  $\bar{n}^+ = \frac{n^+}{n_o}$ ,

$$\bar{n}^- = \frac{n^-}{n_o}.$$

$D_f^+$ ,  $D_f^-$  are diffusion coefficient of ions ( $\text{m}^2\text{s}^{-1}$ )

### 3.2.4 Poisson Boltzmann Model (PBM)

As shown in equations 3-12, 3-13 and 3-14, Nernst-Planck equations are partial differential equations that consume significant extra CPU time to predict the distribution of ion concentration. In the following cases, a simplified model can be used to describe the distribution of ion concentration [Yang et al (1998)].

(i) Considering a microchannel flow with a very small Peclet number, i.e.  $Pe \approx 0$ , the second term in the equation 3-12 drops out and then it becomes

$$\nabla^2 \bar{n}_i + \nabla \cdot \left( \frac{z_i e \bar{n}_i}{k_b T} \nabla \bar{\psi} \right) = 0 \quad (3-15)$$

(ii) If the microchannel flow is fully developed, the components of hydrodynamic velocity  $\vec{V}$  satisfy  $u = u(y, z)$  and  $v = w = 0$  in terms of Cartesian coordinates. Under such conditions, equation 3-12 is reduced to

$$\nabla^2 \bar{n}_i - Pe_x \frac{\partial \bar{n}_i}{\partial x} + \nabla \cdot \left( \frac{z_i e \bar{n}_i}{k_b T} \nabla \bar{\psi} \right) = 0 \quad (3-16)$$

Note that under steady-state situations no mass exchange occurs at the channel wall. This implies that there is no appreciable ionic concentration gradient along the axial direction, i.e.  $\frac{\partial \bar{n}_i}{\partial x} = 0$ . Accordingly, the equation 3-16 is also reduced to equation 3-15. In either case (i) or case (ii), one can readily solve equation 3-16 with well-known Boltzmann distribution, which implies uniform dielectric constant; the number concentration of the type- $i$  ion in a symmetric electrolyte solution is of the form [Mala *et. al.* (1997)]:

$$n_i = n_{oi} \exp\left(-\frac{z_i e \Psi}{k_b T_{in}}\right) \quad (3-17)$$

where  $z_i$  is valence of type- $i$  ions,

$k_b$  is Boltzmann constant ( $1.3805 \times 10^{-23} \text{ JK}^{-1}$ ),

$T$  is absolute temperature (K),

$e$  is electron charge ( $1.6021 \times 10^{-19} \text{ C}$ ),

$n_{oi}$  is bulk concentration of type- $i$  ions.

With the nondimensional terms  $\psi = \frac{z_i e \Psi}{k_b T_{in}}$  and  $\bar{n}_i = \frac{n_i}{n_{oi}}$ , equation 3-17 can be written

as,

$$\bar{n}_i = \exp(-\psi) \quad (3-18)$$

This is the well-known Boltzmann distribution. Therefore, we may conclude that for a microchannel flow with a very small Peclet number or in a fully developed hydrodynamic state, the Boltzmann distribution is still valid.

The net charge density in a unit volume of the fluid is given by:

$$\begin{aligned}
\rho_e &= z_i e (n^+ - n^-) \\
&= z_i e \left[ -n_o \exp\left(\frac{z_i e \Psi}{k_b T}\right) + n_o \exp\left(-\frac{z_i e \Psi}{k_b T}\right) \right] \\
&= -2n_o z_i e \sinh\left(\frac{z_i e \Psi}{k_b T}\right)
\end{aligned} \tag{3-19}$$

where  $n_o$  = average number of positive or negative ions per unit volume or ionic-number concentration.

This leads to the Poisson-Boltzmann equation as shown below:

$$\frac{\partial^2 \psi}{\partial x^2} + \frac{\partial^2 \psi}{\partial y^2} + \frac{\partial^2 \psi}{\partial z^2} = K^2 \sinh \psi \tag{3-20}$$

where  $K$  is the product of  $D_h$  and  $\kappa$ ,  $K = D_h \kappa$

$\kappa = \left( \frac{2n_o z^2 e^2}{\epsilon \epsilon_0 k_b T_o} \right)^{\frac{1}{2}}$ , is Debye-Huckel parameter ( $1/\kappa$  is normally referred as the EDL thickness).

### 3.3 NAVIER-STOKES EQUATION WITH EDL EFFECT

#### 3.3.1 EDL body force

Hitherto, the distribution of the EDL properties such as non-dimensional electrical potential and the net electrical charge density, have been described by equations 3-4, 3-13, 3-14 and 3-19. The EDL effect is introduced to the fluid flow by extra body force term  $\vec{F}_{EDL}$ . As explained in section 3.1, the EDL body force,  $F_{EDL}$  is related to charge density,  $\rho_e$  and  $z$ -direction electrical field strength,  $\vec{E}$  by

$$\vec{F}_{EDL} = \vec{E} \rho_e \tag{3-21}$$

As the literature for 3-D developing was rare, the author developed an expression for the  $\vec{E}$ , which described the EDL effect. When a liquid is forced through a microchannel under a hydrostatic pressure difference, the ions in the mobile part of the EDL are carried towards the downstream end. This causes an electrical current, called the streaming current, to flow in the direction of the liquid flow. The accumulation of ions downstream, however, sets up an electric field with an electrical potential, called the streaming potential. This field generates a current, called the conduction current, to flow back in the opposite direction. When the conduction current is equal to the streaming current, a steady state is reached. Usually the net electrical current  $I$ , flowing in the axial direction of the microchannel, is the algebraic summation of the electrical convection current (i.e., streaming current),  $I_s$  and the electrical conduction current,  $I_c$ . In a steady state, this net electrical current should be zero.

$$I = I_s + I_c = 0 \quad (3-22)$$

As shown in Figure 3.1, our physic model defines the net flow to be in the Z-direction, therefore only charge with Z-direction velocity component is contribute to the current, hence the electrical streaming current is of the form

$$I_s = \int \left[ \rho_e w - \left( eD \frac{\partial n^+}{\partial z} - eD \frac{\partial n^-}{\partial z} \right) \right] dA \quad (3-23)$$

Generally, the electrical conduction current in the microchannel includes two parts: one is the bulk liquid conduction current,  $I_{bc}$  whereas the other is the surface conduction current,  $I_{sc}$ , due to the accumulated charge in the EDL. Then the electrical conduction current can be expressed as

$$I_c = I_{bc} + I_{sc} = \lambda_t E_z A \quad (3-24)$$

where  $\lambda_t$  is the total electrical conductivity, given by

$$\lambda_t = \lambda_o + \left( \frac{P_C}{A_C} \right) \lambda_s \quad (3-25)$$

Here  $P_C$  and  $A_C$  are the wetting perimeter and cross-sectional area of the channel, respectively.  $\lambda_o$  is the bulk electrical conductivity of the solution and  $\lambda_s$  is the specific conductivity. The total electrical conductivity,  $\lambda_t$  was chosen from experimental result by Mala *et. al.*(1997b). With selected height of microchannel, concentration of solution microchannel height and the material of the microchannel, Total resistance,  $R_T$  can be obtained (as shown in Figure 3.2). Hence  $\lambda_t$  can be found by the reciprocal of  $R_T$ .

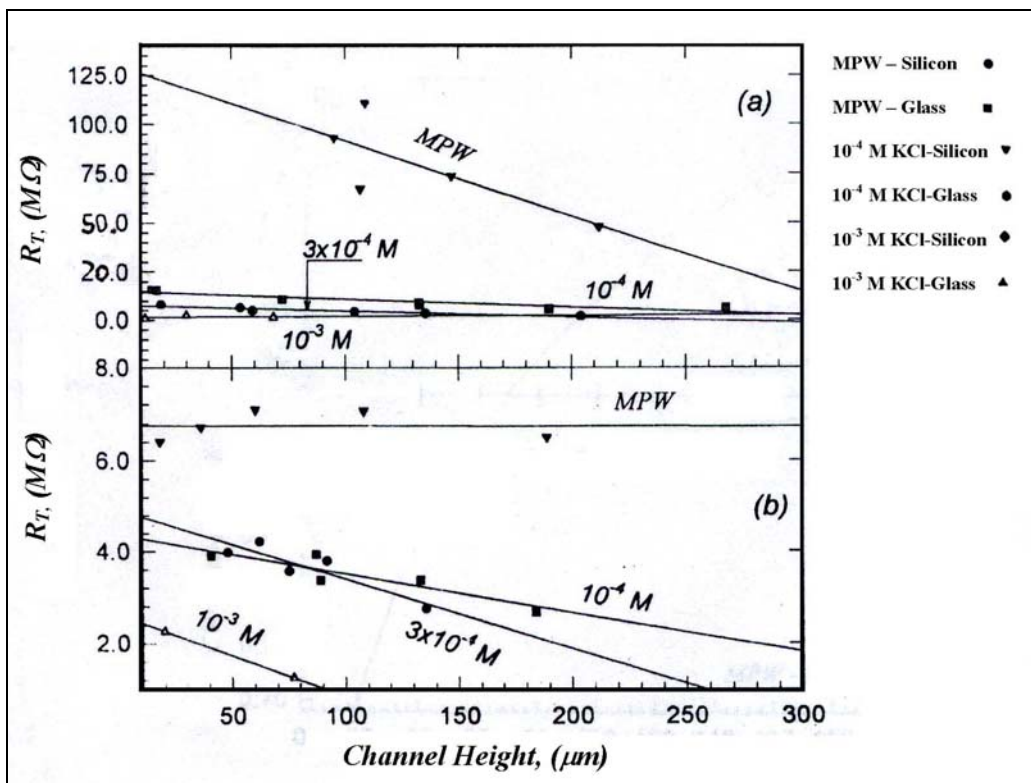


Figure 3.2 Variation of the channel's total electrical resistance with the channel height;

(a) glass; and (b) silicon channels [Mala *et. al.*(1997b)]

Although the flow field include developing region, as the microchannel model shown in Figure 3.1 is symmetric and the net flow is in Z-direction, only Z-direction component of electrical field strength  $E_z$  is contributed to the EDL body force. Physically, the Z-direction electrical field strength,  $E_z$  is called the streaming potential and is a steady-state potential difference which builds up along a microchannel.

Substituting equations 3-24, and 3-23 into equation 3-22, the  $z$ -direction electrical field strength,  $E_z$  can be written as

$$\lambda_t E_z A = \int \left[ \rho_e W - \left( eD \frac{\partial n^+}{\partial Z} - eD \frac{\partial n^-}{\partial Z} \right) \right] dA \quad (3-26)$$

therefore, the dimensionless form is obtained as

$$\bar{E}_z = \left( \frac{D_h}{W_c} \right) \left( \frac{D_h}{L_c} \right) \bar{G}_2 \int \left[ \rho_e w - \left( eD_f \frac{\partial n^+}{\partial z} - eD_f \frac{\partial n^-}{\partial z} \right) \right] d\bar{A} \quad (3-27)$$

where

$$\bar{G}_2 = \frac{2n_o z_i e D_h W_{in} H_c}{\lambda_t \xi_o}, \bar{A} = \frac{A}{L_c W_c}$$

### 3.3.2 Governing Equations

Hence, the Navier Stokes equations [Hoffmann (1989)] of 3-D steady state incompressible developing laminar flow for microchannel are given as follows:

#### Continuity Equation

$$\frac{\partial u}{\partial x} + \frac{\partial v}{\partial y} + \frac{\partial w}{\partial z} = 0 \quad (3-28)$$

#### Momentum Equations

x-direction

$$u \frac{\partial u}{\partial x} + v \frac{\partial u}{\partial y} + w \frac{\partial u}{\partial z} = \frac{1}{\text{Re}} \left( \frac{\partial^2 u}{\partial x^2} + \frac{\partial^2 u}{\partial y^2} + \frac{\partial^2 u}{\partial z^2} \right) - \frac{\partial p}{\partial x} \quad (3-29)$$

y-direction

$$u \frac{\partial v}{\partial x} + v \frac{\partial v}{\partial y} + w \frac{\partial v}{\partial z} = \frac{1}{\text{Re}} \left( \frac{\partial^2 v}{\partial x^2} + \frac{\partial^2 v}{\partial y^2} + \frac{\partial^2 v}{\partial z^2} \right) - \frac{\partial p}{\partial y} \quad (3-30)$$

z-direction

$$u \frac{\partial w}{\partial x} + v \frac{\partial w}{\partial y} + w \frac{\partial w}{\partial z} = \frac{1}{\text{Re}} \left( \frac{\partial^2 w}{\partial x^2} + \frac{\partial^2 w}{\partial y^2} + \frac{\partial^2 w}{\partial z^2} \right) - \frac{\partial p}{\partial z} - \overline{G_1} \overline{E_z} \overline{\rho_e} \quad (3-31)$$

### Energy Equation

$$u \frac{\partial \theta}{\partial x} + v \frac{\partial \theta}{\partial y} + w \frac{\partial \theta}{\partial z} = \frac{1}{\text{Re}} \left( \frac{\partial^2 \theta}{\partial x^2} + \frac{\partial^2 \theta}{\partial y^2} + \frac{\partial^2 \theta}{\partial z^2} \right) + \frac{Ec}{\text{Re}} \phi \quad (3-32)$$

the following non-dimensional terms are used

$$x = \frac{X}{D_h} \quad y = \frac{Y}{D_h} \quad z = \frac{Z}{D_h}$$

$$u = \frac{U}{W_{in}} \quad v = \frac{V}{W_{in}} \quad w = \frac{W}{W_{in}}$$

$$p = \frac{P - P_{in}}{\rho_f W_{in}^2} \quad \theta = \frac{T - T_{in}}{q'' D_h} \quad \alpha = \frac{k_f}{C_p \rho_f}$$

$$\text{Re} = \frac{\rho_f W_{in} D_h}{\mu_f} \quad \text{Pr} = \frac{\mu_f}{\rho_f \alpha} \quad Ec = \frac{W_{in}^2}{C_p (T_s - T_{in})}$$

$$Pe = \text{Re} \text{Pr} = \frac{W_{in} D_h}{\alpha} \quad \overline{G_1} = \frac{2n_o z_i e \xi_o}{\rho W_{in}^2} \quad D_h = \frac{4L_c W_c}{2(L_c + W_c)}$$

$$\overline{\rho_e} = \frac{n^+ - n^-}{n_0}$$



$$\phi = 2 \left[ \left( \frac{\partial u}{\partial x} \right)^2 + \left( \frac{\partial v}{\partial y} \right)^2 + \left( \frac{\partial w}{\partial z} \right)^2 \right] + \left[ \frac{\partial u}{\partial y} + \frac{\partial v}{\partial x} \right]^2 + \left[ \frac{\partial w}{\partial y} + \frac{\partial v}{\partial z} \right]^2 + \left[ \frac{\partial u}{\partial z} + \frac{\partial w}{\partial x} \right]^2$$

Note: All undefined symbols are defined in the list of symbols (page vii)

### 3.4 BOUNDARY CONDITIONS

The following boundary conditions are applied [Ng and Tan (2000a)]

#### Velocity

$$\text{At } x=0 \quad u=0, \frac{\partial v}{\partial x}=0, \frac{\partial w}{\partial x}=0 \quad (\text{Symmetric boundary condition})$$

$$x = \frac{W_c}{2D_h}, \quad u=0, v=0, w=0 \quad (\text{Wall boundary condition})$$

$$y=0, \quad u=0, v=0, w=0 \quad (\text{Wall boundary condition})$$

$$y = \frac{L_c}{D_h}, \quad u=0, v=0, w=0 \quad (\text{Wall boundary condition})$$

$$z=0, \quad u=0, v=0, w=1 \quad (\text{Inlet condition})$$

$$z = \frac{H_c}{D_h}, \quad \frac{\partial u}{\partial z}=0, \frac{\partial v}{\partial z}=0, \frac{\partial w}{\partial z}=0 \quad (\text{Fully developed condition})$$

#### Temperature

$$\text{At } x=0, \quad \frac{\partial \theta}{\partial x}=0 \quad (\text{Symmetric boundary condition})$$

$$x = \frac{W_c}{2D_h}, \quad \frac{\partial \theta}{\partial x} = q'' \quad (\text{Wall boundary condition})$$

$$y=0, \quad \theta=0 \quad (\text{Constant heat flux})$$

$$y = \frac{L_c}{D_h}, \quad \theta=0 \quad (\text{Wall boundary condition})$$

$$z=0, \quad \theta=0 \quad (\text{Inlet condition})$$

$$z = \frac{H_C}{D_h}, \quad \frac{\partial \theta}{\partial z} = 0 \quad (\text{Fully developed condition})$$

### EDL Potential

$$\text{At } x = 0, \quad \frac{\partial \psi}{\partial x} = 0 \quad (\text{Symmetric boundary condition})$$

$$x = \frac{W_C}{2D_h}, \quad \psi = \bar{\xi}_o \quad (\text{Wall boundary condition})$$

$$y = 0, \quad \psi = \bar{\xi}_o \quad (\text{Wall boundary condition})$$

$$y = \frac{L_C}{D_h}, \quad \psi = \bar{\xi}_o \quad (\text{Wall boundary condition})$$

$$z = 0, \quad \psi = 0 \quad (\text{Inlet condition})$$

$$z = \frac{H_C}{D_h}, \quad \frac{\partial \psi}{\partial z} = 0 \quad (\text{Fully developed condition})$$

where

$$\bar{\xi}_o = \frac{z_i e \xi_o}{k_b T_{in}}$$

$\xi_o$  is the Zeta potential on wall.

## 3.5 THE IMPORTANT PARAMETERS

In this section, some of the important parameters are defined and listed [White (1988)]. The volumetric flow rate through the parallel plates can be obtained by integrating the velocity distribution over the cross-sectional area; the volume flow rate,  $Q$  through the parallel plates can then be obtained as follows:

$$Q = \int_{A_c} W dA_c \quad (3-28)$$

The friction coefficient  $C_f$  is defined as:

$$C_f = f \text{ Re} \quad (3-29)$$

The friction factor,  $f$  is given as:

$$f = \frac{8\tau_w}{\rho_f W_{in}^2} \quad (3-30)$$

where

$$W_{in} = \frac{Q}{A_c} \quad (3-31)$$

The shear stress is given by

$$\tau_w = \left| \frac{\mu W_{in}}{D_h} \frac{dw}{dx} \right| \quad (3-32)$$

The Reynolds number is given by:

$$\text{Re} = \frac{\rho_f V_{ave} D_h}{\mu} \quad (3-33)$$

Assuming that both plates have constant and equal temperatures and the inlet temperature of the fluid is known, the equation can now be solved numerically [Patankar (1980)] to obtain the temperature distribution in the XZ plane of the microchannel.

According to the energy balance,

$$-k_f \left| \frac{\partial T}{\partial Y} \right|_{Y=0} = h(T_w - T_m) \quad (3-34)$$

where

$$T_m = \frac{1}{V_{ave} A_c} \int_{A_c} W T dA_c \quad (3-35)$$

The Nusselt number is given as below:

$$Nu = \frac{2hD_h}{k_f} = \frac{2}{\theta_m} \left| \frac{\partial \theta}{\partial x} \right|_{x=\pm 1} \quad (3-36)$$

where

$$\theta = \frac{T - T_{in}}{q'' D_h},$$

The average Nusselt number is calculated as:

$$Nu_{ave} = \frac{1}{z} \int_0^{L_c} Nu dz \quad (3-37)$$

Note that the derivative  $\left| \frac{\partial \theta}{\partial x} \right|_{x=\pm 1}$  is calculated using the standard three-point formula.

Table 3.1 show the general parameters used in the analysis unless stated:

Table 3.1 General parameters and their values used

Model Parameters	Values	Fluid Properties (salt water)	Values
Width, $W_c$	40 $\mu$ m	Density, $\rho_f$	997 Kg/m <sup>3</sup>
Length, $L_c$	20 $\mu$ m	Viscosity, $\mu_f$	8.55 $\times 10^{-4}$ (Ns)/m <sup>2</sup>
Height, $H_c$	400 $\mu$ m	Thermal Conductivity, $k_f$	0.613 W/(mK)
Hydraulic diameter, $D_h$	25.67 $\mu$ m	Heat Capacity, $C_p$	4179 J/(KgK)
-	-	Schmidt No., Sc	10 <sup>5</sup>
-	-	Reynolds No., Re	60
-	-	Prandtl No., Pr	6.22
-	-	Eckert number No., Ec	6.03 $\times 10^{-5}$

## Chapter Four

### NUMERICAL ALGORITHM

#### 4.1 INTRODUCTION AND COMPUTATIONAL MESH

The numerical algorithm used in this project is based on SIMPLER, which was introduced by Patankar (1980) and is a robust algorithm that has been widely used. As there are highly nonlinear source terms associated in equations 3-13, 3-14 and 3.15, the commercial software such as CFX or Fluent may not be able to produce stable and robust computation, a code based on FORTRAN programming was developed to predict the 3-D developing microchannel flow as described in chapter 3.

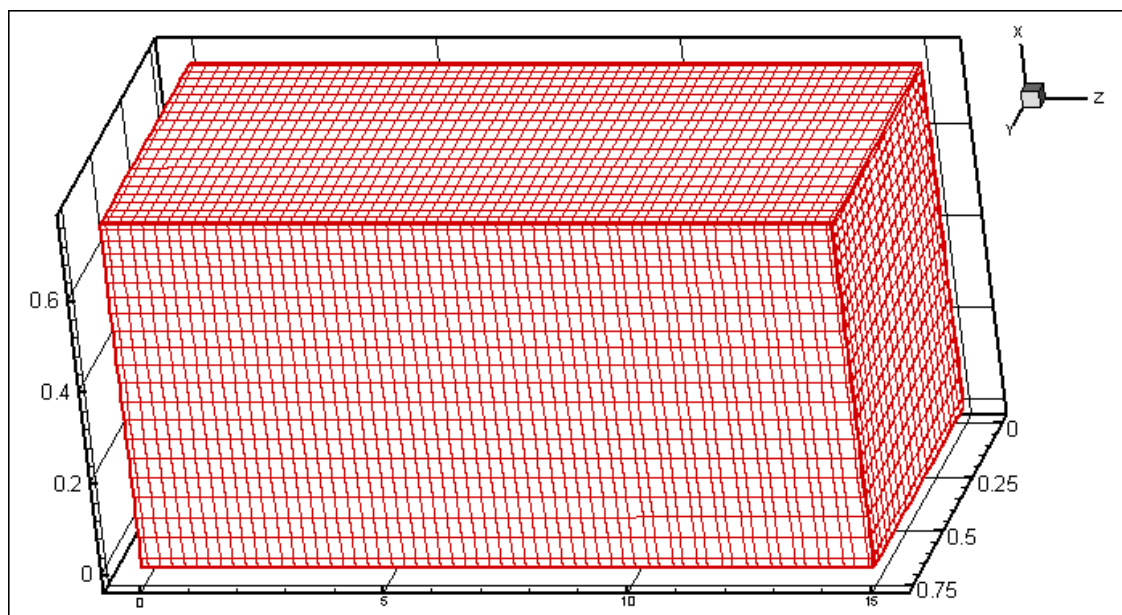


Figure 4.1 Mesh for computation

Based on the 3-D physical model mentioned in chapter 3 (Figure 3.1), the mesh used for computation is shown in Figure 4.1 which is symmetric at Y-Z plane. With suitable boundary conditions, only half of the physical model is meshed and solved. The number of mesh used in this project will be  $20 \times 20 \times 60$  in x, y and z direction respectively.

In the following sections, the grid generation and discretization will be illustrated in 2-D for better illustration, and will be extended to 3-D.

## 4.2 GRIDS AND CONTROL VOLUME GENERATION

In this thesis, the algorithm is first illustrated in 2-D and will be extended to 3-D in section 4.4. For a two-dimensional problem, as used for developing flow cases, the basic construction of the control volumes and the grids is shown in Figure 4. 2 [Patankar (1991)].

Firstly, the calculation domain is divided into control volumes. Then, the grid points are placed at the centers of the control volumes. In Figure 4.2, the dashed lines correspond to the boundaries of the control volumes; the solid lines denote the grid lines while the dots are the grid points. A grid point will hence link to its four-neighbouring grid points through the four faces of the control volume. For a near-boundary control volume, one of its faces coincides with the boundary of the calculation domain. A boundary grid point will be placed at the center of the control-volume face.  $I$  and  $J$  as shown in Figure 4.2 denote the grid locations in the  $x$ - and  $y$ -directions respectively. The value  $I=1$  refers to the grid line at the left boundary while  $I=LI$  is for the right boundary. Similarly,  $J=1$  and  $J=M1$  stand for the bottom and top boundary grid lines respectively.

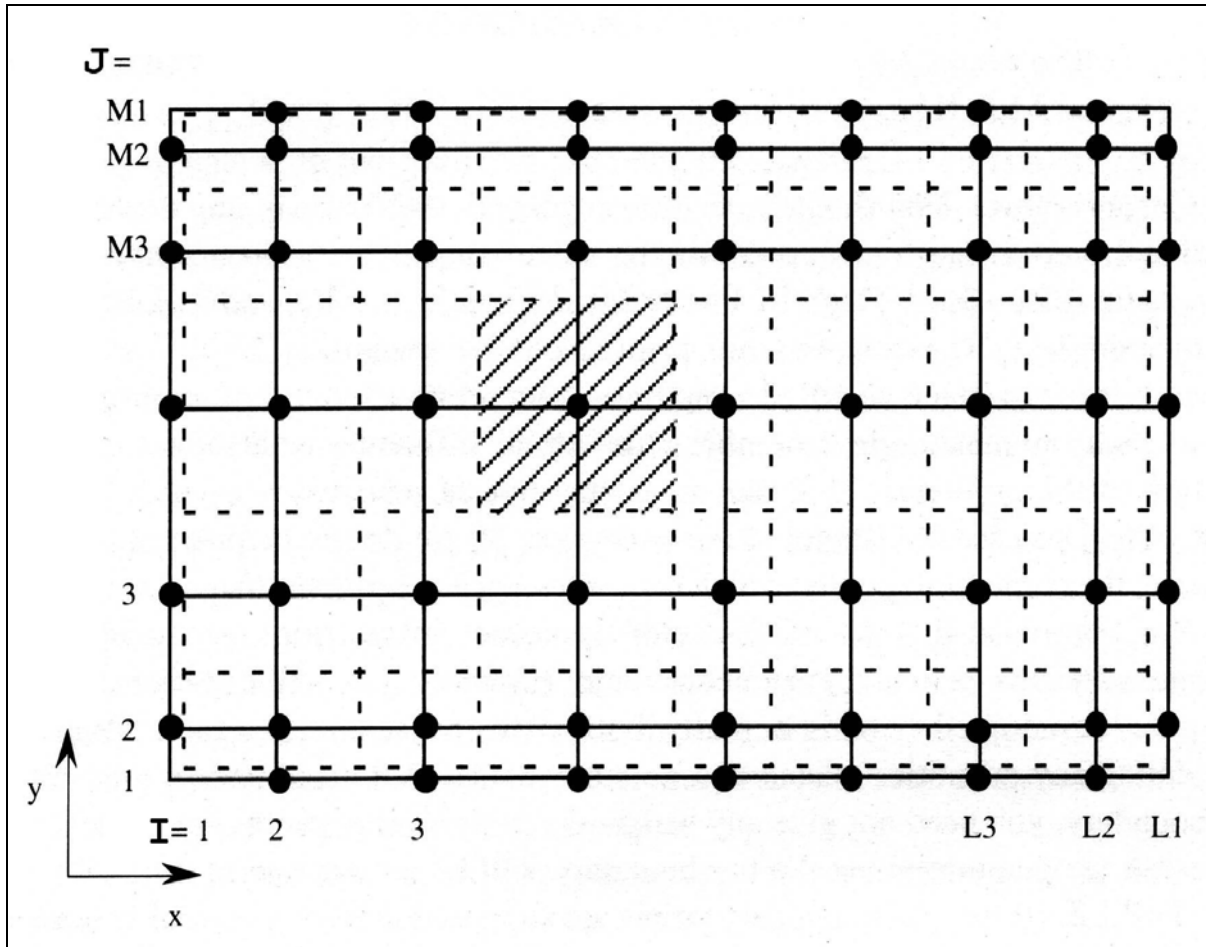


Figure 4.2 Control volumes and grid points

### 4.3 GENERAL DISCRETIZATION EQUATION FOR TWO DIMENSIONS

For the simple illustration, the derivation of discretization equation will be shown in two dimensions. The non-dimensional Poisson-Boltzmann, momentum and energy equations are basically the differential equations and thus can be represented by appropriate general differential equations Figure 4. 2 [Patankar (1980)]:

$$\frac{\partial(\rho\phi)}{\partial t} + \frac{\partial(\rho u_i \phi)}{\partial x_i} = \frac{\partial}{\partial x_i} \left( \Gamma \frac{\partial \phi}{\partial x_i} \right) + S \quad (4-1)$$

Equation (4-1) can also be written for incompressible flows as

$$\rho \frac{\partial \phi}{\partial t} + \rho u_i \frac{\partial \phi}{\partial x_i} = \frac{\partial}{\partial x_i} \left( \Gamma \frac{\partial \phi}{\partial x_i} \right) + S \quad (4-2)$$

where  $\phi$  denotes the dependent variable of the general differential equation. The fluxes of  $\phi$  are defined by:

$$J_x = \rho u \phi - \Gamma \frac{\partial \phi}{\partial x} \quad (4-3)$$

$$J_y = \rho v \phi - \Gamma \frac{\partial \phi}{\partial y} \quad (4-4)$$

where  $\Gamma$  is the generalized diffusion coefficient.

The two dimensional form of equation (4-1) can be written as

$$\frac{\partial(\rho\phi)}{\partial t} + \frac{\partial J_x}{\partial x} + \frac{\partial J_y}{\partial y} = S \quad (4-5)$$

The integration of equation (4-5) over the control volume is shown in Figure 4.2 would give

$$\frac{(\rho_P \phi_P - \rho_P^o \phi_P^o) \Delta x \Delta y}{\Delta t} + J_e - J_w + J_n - J_s = (S_C + S_P \phi_P) \Delta x \Delta y \quad (4-6)$$

where the source term has been linearized in the usual manner and, for the unsteady terms,  $\rho_P$  and  $\phi_P$  are assumed to converse over the whole control volume.



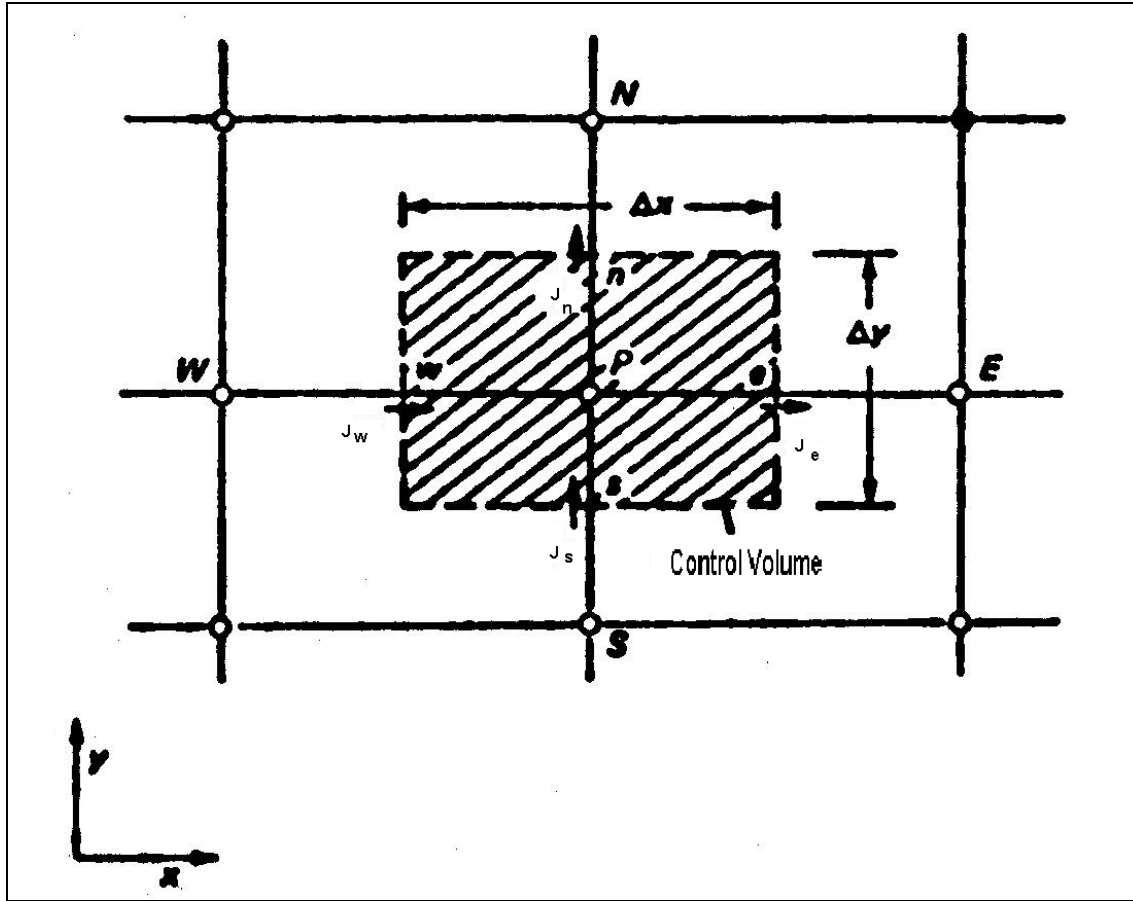


Figure 4.3 Control volumes for the two-dimensional situation

The “old” values are denoted by  $\rho_P^o$  and  $\phi_P^o$ . In conformity with the fully implicit practice, all other values (i.e. those without a superscript) are to be regarded as the “new” values. The quantities  $J_e$ ,  $J_w$ ,  $J_n$ ,  $J_s$  are the integrated total fluxes over the control volume faces; that is  $J_e$  stands for  $\int J_x dy$  over the interface  $e$ , and so on.

In a similar manner, we can integrate the continuity equation (3.1) over the control volume and obtain

$$\frac{(\rho_P - \rho_P^o) \Delta x \Delta y}{\Delta t} + F_e - F_w + F_n - F_s = 0 \quad (4-7)$$

where  $F_e$ ,  $F_w$ ,  $F_n$ ,  $F_s$  are the mass flow rates through the faces of the control volume. If  $\rho u$  at point  $e$  is taken to prevail over the whole interface  $e$ , we can write

$$F_e = (\rho u)_e \Delta y \quad (4-8a)$$

$$F_w = (\rho u)_w \Delta y \quad (4-8b)$$

$$F_n = (\rho u)_n \Delta x \quad (4-8c)$$

$$F_s = (\rho u)_s \Delta x \quad (4-8d)$$

If we now multiply equation by  $\phi_P$  and subtract it from equation (4-6), we obtain

$$\begin{aligned} & (\phi_P - \phi_P^o) \frac{\rho_P^o \Delta x \Delta y}{\Delta t} + (J_e - F_e \phi_P) - (J_w - F_w \phi_P) + (J_n - F_n \phi_P)_w \\ & - (J_s - F_s \phi_P) = (S_C + S_P \phi_P) \Delta x \Delta y \end{aligned} \quad (4-9)$$

For the grid points  $i$  and  $i+1$  separated by a distance  $\delta$ , as shown in Figure 4.3, the total flux  $J$  crossing an interface between these grid points can be represented using equation (4-3) as

$$J^* \equiv \frac{J\delta}{\Gamma} = P\phi - \frac{d\phi}{d(\frac{x}{\delta})} \quad (4-10)$$

where  $P$  is the Peclet number,  $\frac{\rho u \delta}{\Gamma}$ .

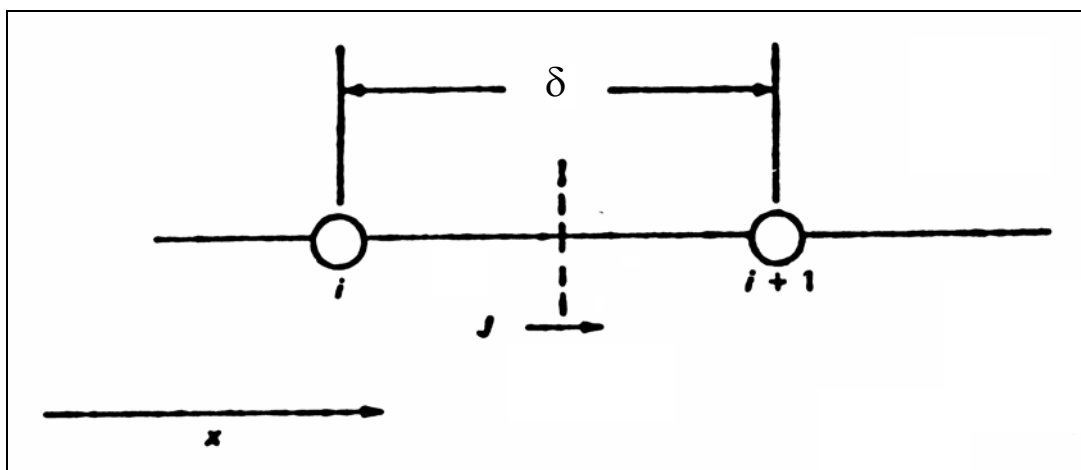


Figure 4.4 Total flux  $J$  between two grid points

The value of  $\phi$  at the interface will be some weighted average of  $\phi_i$  and  $\phi_{i+1}$ , while the

gradient  $\frac{d\phi}{d(\frac{x}{\delta})}$  will be some multiple of  $\phi_{i+1} - \phi_i$ . Thus  $J^*$  can also be represented as

$$J^* = P[\alpha\phi_i + (1-\alpha)\phi_{i+1}] - \beta(\phi_{i+1} - \phi_i) \quad (4-11)$$

where  $\alpha$  and  $\beta$  are dimensionless multipliers that depend on  $P$ . In this manner,  $J^*$  can be expressed as

$$J^* = B\phi_i + A\phi_{i+1} \quad (4-12)$$

where  $A$  and  $B$  are dimensionless coefficient that are functions of the Peclet number,  $Pe$  (The coefficient  $A$  is associated with the grid point  $i+1$ , which is Ahead of the interface, while  $B$  is connected with the grid point  $i$ , which is Behind the interface, as seen from the chosen coordinate direction ).

The relation of  $A$  and  $B$  with Peclet number  $P$  is shown in Figure 4.5

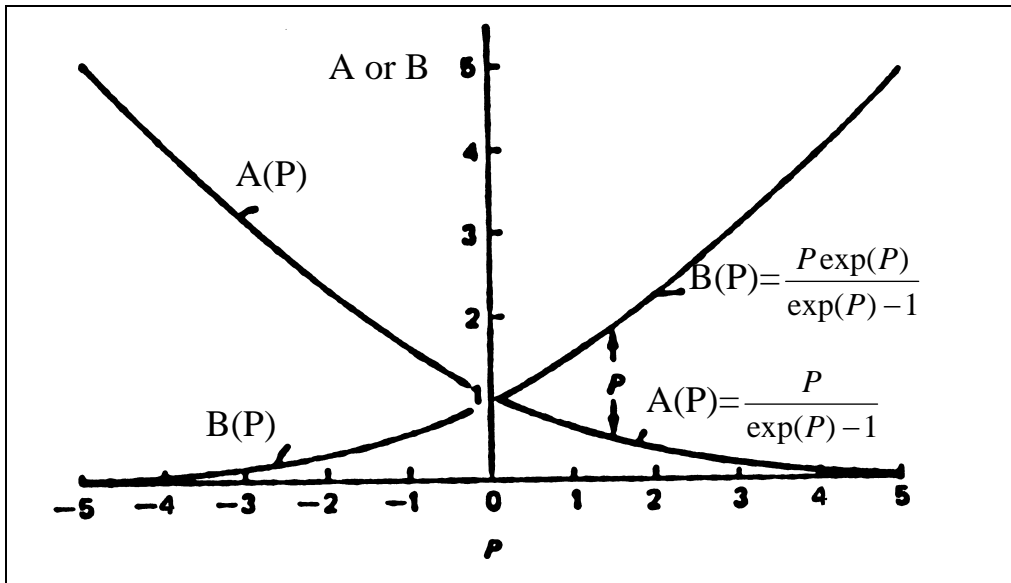


Figure 4.5 Variation of  $A$  and  $B$  with Peclet number [Patankar (1980)]

Consider the case when  $\phi_i$  and  $\phi_{i+1}$  are equal, the diffusion flux  $\Gamma \frac{\partial \phi}{\partial x}$  must be zero, and

$J$  would then simply be the convection flux  $\rho u \phi$ . Thus, under these conditions we have,

$$J^* = P\phi_i = P\phi_{i+1} \quad (4-13)$$

Combination of equations (4-11) and (4-12) leads to

$$B = A + P \quad (4-14)$$

By combining equations (4-11) and (4-13), we can get the following two relations:

$$J^* - P\phi_i = A(\phi_i - \phi_{i+1}) \quad (4-15)$$

$$J^* - P\phi_{i+1} = B(\phi_i - \phi_{i+1}) \quad (4-16)$$

Applying equations (4-14) and (4-15) on interface  $e$  and  $w$  as shown in Figure 4.3,

terms such as  $J_e - F_e \phi_P$  and  $J_w - F_w \phi_P$  can be expressed as

$$J_e - F_e \phi_P = a_e(\phi_P - \phi_e) \quad (4-17a)$$

$$J_w - F_w \phi_P = a_w(\phi_P - \phi_w) \quad (4-17b)$$

where

$$a_e = D_e A(|P_e|) + [-F_e, 0] \quad (4-18a)$$

$$a_w = D_w A(|P_w|) + [-F_w, 0] \quad (4-18b)$$

$[A, B]$  defined a new operator to denote the greater of  $A$  and  $B$ ,  $|C|$  modulus which denotes the positive value of  $C$ .

Here  $D_e$  and  $D_w$ , just like their counterparts  $F_e$  and  $F_w$  contain the area  $\Delta y$  of the faces  $e$  and  $w$  (will be shown in equation 4-21). With similar expressions for  $J_s - F_s \phi_P$  and

$J_n - F_n \phi_P$ , we are in a position to write the final form of the discretization equation.

Because of the nature of the expression in equation (4-16), the rule about the sum of the neighbour coefficients is readily satisfied.

The two-dimensional discretization equation can now be written as

$$a_p \phi_p = a_e \phi_e + a_w \phi_w + a_n \phi_n + a_s \phi_s + b \quad (4-19)$$

where

$$a_e = D_e A(|P_e|) + [-F_e, 0] \quad (4-20a)$$

$$a_w = D_w A(|P_w|) + [-F_w, 0] \quad (4-20b)$$

$$a_n = D_n A(|P_n|) + [-F_n, 0] \quad (4-20c)$$

$$a_s = D_s A(|P_s|) + [-F_s, 0] \quad (4-20d)$$

$$a_p^o = \frac{\rho_p^o \Delta x \Delta y}{\Delta t} \quad (4-20e)$$

$$b = S_C \Delta x \Delta y + a_p^o \phi_p^o \quad (4-20f)$$

$$a_p = a_e + a_w + a_n + a_s + a_p^o - S_p \Delta x \Delta y \quad (4-20g)$$

Here  $\phi_p^o$  and  $\rho_p^o$  refer to the known values at time  $t$ , while all other values ( $\phi_p$ ,  $\phi_e$ ,  $\phi_w$ ,  $\phi_n$ ,  $\phi_s$  and so on) are the unknown values at time  $t + \Delta t$ . The flow rates  $F_e$ ,  $F_w$ ,  $F_n$ ,  $F_s$  have been defined in equation (4-8). The corresponding conductances are defined as

$$D_e = \frac{\Gamma_e \Delta y}{(\delta x)_e} \quad (4-21a)$$

$$D_w = \frac{\Gamma_w \Delta y}{(\delta x)_w} \quad (4-21b)$$

$$D_n = \frac{\Gamma_n \Delta y}{(\delta y)_n} \quad (4-21c)$$

$$D_s = \frac{\Gamma_s \Delta y}{(\delta y)_s} \quad (4-21d)$$

and the Peclet numbers by

$$P_e = \frac{F_e}{D_e}, P_w = \frac{F_w}{D_w}, P_n = \frac{F_n}{D_n}, P_s = \frac{F_s}{D_s} \quad (4-22)$$

The power-law scheme is recommended for the function  $A(|P|)$ , which is

$$A(|P|) = \left[ 0, (1 - 0.1|P|)^5 \right] \quad (4-23)$$

where  $A$  is the storage capacity per unit volume and  $S$  is the generation rate per unit volume for the relevant physical quantity.

Hence, in general, for each definition of dependent variable,  $\phi$ , there exist its corresponding meanings of  $A$ ,  $F$  and  $S$ .

## 4.4 GENERAL DISCRETIZATION EQUATION FOR THREE DIMENSIONS

Now, we set out to write a discretization equation based on the general differential equation (4-1) for three dimensions (with  $T$  and  $B$  representing the “top” and “bottom” neighbours in the  $z$  direction):

$$a_P \phi_P = a_e \phi_e + a_w \phi_w + a_n \phi_n + a_s \phi_s + a_t \phi_t + a_b \phi_b + b \quad (4-24)$$

where

$$a_e = D_e A(|P_e|) + [-F_e, 0] \quad (4-25a)$$

$$a_w = D_w A(|P_w|) + [-F_w, 0] \quad (4-25b)$$

$$a_n = D_n A(|P_n|) + [-F_n, 0] \quad (4-25c)$$

$$a_s = D_s A(|P_s|) + [-F_s, 0] \quad (4-25d)$$

$$a_t = D_t A(|P_t|) + [-F_t, 0] \quad (4-25e)$$

$$a_b = D_b A(|P_b|) + [-F_b, 0] \quad (4-25f)$$

$$a_p^o = \frac{\rho_p^o \Delta x \Delta y \Delta z}{\Delta t} \quad (4-25g)$$

$$b = S_c \Delta x \Delta y \Delta z + a_p^o \phi_p^o \quad (4-25h)$$

$$a_p = a_e + a_w + a_n + a_s + a_t + a_b + a_p^o - S_p \Delta x \Delta y \Delta z \quad (4-25i)$$

The flow rates and conductance are defined as

$$F_e = (\rho u)_e \Delta y \Delta z, \quad D_e = \frac{\Gamma_e \Delta y \Delta z}{(\delta x)_e} \quad (4-26a)$$

$$F_w = (\rho u)_w \Delta y \Delta z, \quad D_w = \frac{\Gamma_w \Delta y \Delta z}{(\delta x)_w} \quad (4-26b)$$

$$F_n = (\rho u)_n \Delta z \Delta x, \quad D_n = \frac{\Gamma_n \Delta z \Delta x}{(\delta y)_n} \quad (4-26c)$$

$$F_s = (\rho u)_s \Delta z \Delta x, \quad D_s = \frac{\Gamma_s \Delta z \Delta x}{(\delta y)_s} \quad (4-26d)$$

$$F_t = (\rho u)_t \Delta x \Delta y, \quad D_t = \frac{\Gamma_t \Delta x \Delta y}{(\delta z)_t} \quad (4-26e)$$

$$F_b = (\rho u)_b \Delta x \Delta y, \quad D_b = \frac{\Gamma_b \Delta z \Delta x}{(\delta z)_b} \quad (4-26f)$$

The Peclet number  $P$  is to be taken as the ratio of  $F$  and  $D$  as shown in equation (4-22)

respectively. The function of  $A(|P|)$  is same as equation (4-23).

## 4.5 TREATMENT OF BOUNDARY CONDITIONS

For every near-boundary grid point, the corresponding grid point acts as one of the neighbours. Therefore, either a value or an equation must be available for the  $\phi$  at the boundary node. Two kinds of boundary treatment are used. The lower-order treatment is a logical consequence of the formulation described in section 4.2 while the higher-order treatment gives a more accurate formula for the boundary fluxes.

#### 4.5.1 Lower-Order Treatment

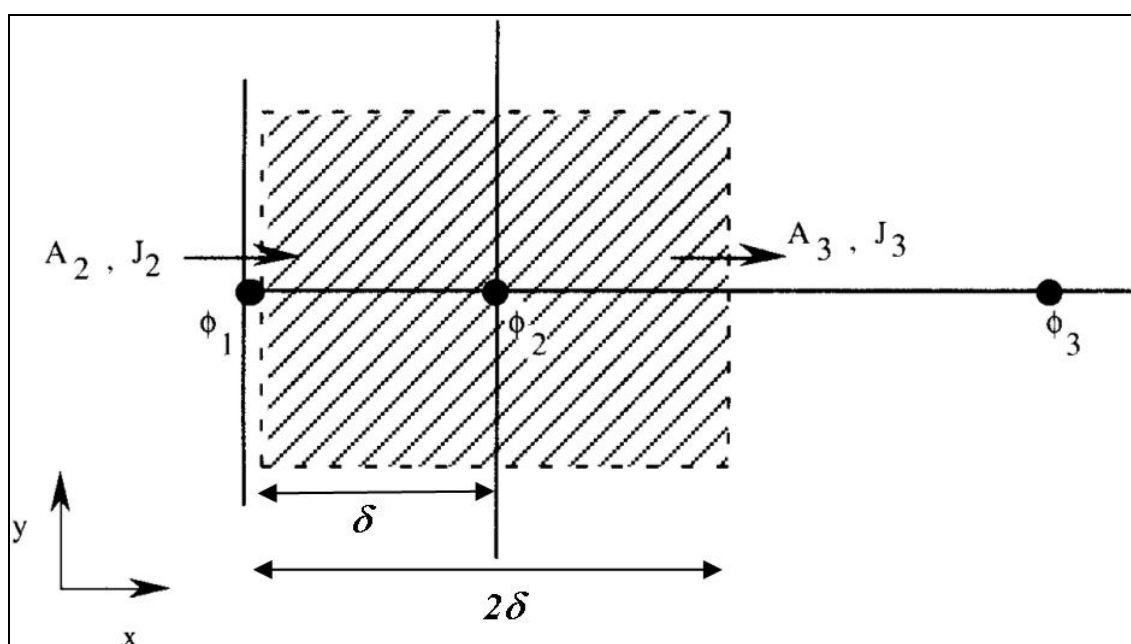


Figure 4.6 A typical control volume near the left boundary

In the lower-order treatment [Patankar (1991)], the total flux formulae are obtained if the Peclet number  $P$  is to be taken as the ratio of  $F$  and  $D$  as shown in equation (4-22) respectively. The function of  $A(|P|)$  is same as equation (4-23).

Figure 4.6 illustrates the situation near the boundary grid point  $(I,J)$ . The control volume face for  $I=2$ , which coincides with the left boundary of the domain can be considered to lie between the locations of  $\phi_1$  and  $\phi_2$  if a control volume of infinitesimal



thickness is imagined around the location of  $\phi_1$ . With that, the total flux,  $J_2$  at the boundary is still the same as given in equation (4-6).

The total flux formulae in the lower-order treatment are derived from the piecewise-linear profile, which implies that the flux,  $J$  remains constant between two neighbouring grids. However, the interface is not located midway between  $\phi_1$  and  $\phi_2$ , giving somewhat inaccurate results.  $J_2$  is expressed as,

$$J_2 = \left( \frac{\Gamma_2}{\delta} \right) (\phi_1 - \phi_2) \quad (4-27)$$

#### 4.5.2 Higher-Order Treatment

In the higher-order treatment [Patankar (1991)], the total flux formulae are obtained if the diffusion flux is regarded as being linear in distance between the two opposite faces of a control volume. When applied to the boundary control volume, the following flux profile as shown in Figure 4.7 is obtained. The  $J$  distribution is linear with  $x$  between  $J_2$  at the left face and  $J_3$  at the right face of the control volume.

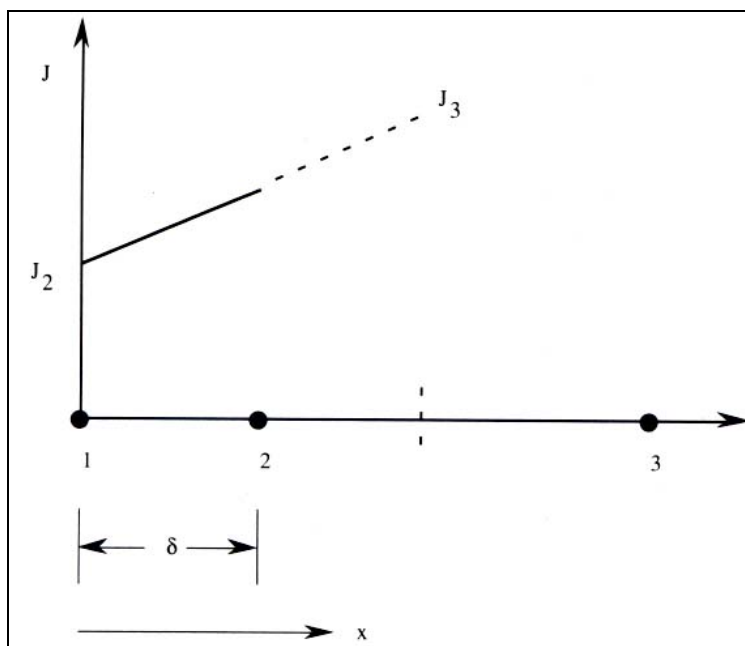


Figure 4.7 Assumed profile for the total flux  $J$  in the higher-order treatment

The assumed  $J$  distribution between the grid points 1 and 2 is given as:

$$J = -\Gamma \frac{d\phi}{dx} = J_2 + J'(x - x_1) \quad (4-28)$$

where

$$J' = \frac{dJ}{dx} \approx \frac{J_3 - J_2}{2\delta} \quad (4-29)$$

as shown in figure 4-6,  $2\delta$  is the distance between boundary for  $J_2$  and  $J_3$

An expression for  $J_2$  is obtained as follows:

$$J_2 = \left(\frac{4}{3}\right) \left[ \left(\frac{\Gamma_2}{\delta}\right) (\phi_1 - \phi_2) \right] - \left(\frac{1}{3}\right) J_3 \quad (4-30)$$

A generalized form of the equation is given as:

$$J_2 = \beta \left[ \left(\frac{\Gamma_2}{\delta}\right) (\phi_1 - \phi_2) \right] - (\beta - 1) J_3 \quad (4-31)$$

The expression for  $J_3$  can be written along the lines of equation (4-6) as:

$$J_3 A_3 = D_3 (\phi_1 - \phi_2) \quad (4-32)$$

where  $D_3$  is the appropriate diffusion conductance for the link connecting  $\phi_1$  and  $\phi_2$ .

The discretization equation for the near-boundary control volume (2, $J$ ) should now be based on equation (4-18) for the flux  $J_2$  through its left face rather than on equation (4-7).

The expression of the diffusion flux,  $J_2$  is hence written as:

$$J_2 = \beta \left[ \left(\frac{\Gamma_2}{\delta}\right) (\phi_1 - \phi_2) \right] + (\beta - 1) \left( \frac{D_3}{A_3} \right) (\phi_3 - \phi_2) \quad (4-33)$$

The equation detailed in this section can be applied with appropriate values of  $\beta$  as follows:

1. Higher-order treatment:  $\beta=4/3$  [as equation (4-30)]
2. Lower-order treatment:  $\beta=1$  [as equation (4-27)]

### 4.5.3 Types of Boundary Conditions

In general, there are two types of boundary conditions [Patankar (1991)]:

1. The boundary value of  $\phi$  is given.
2. The diffusion flux at the boundary,  $J_B$  is given in the form of:

$$J_B = f_C + f_P \phi_B \quad (4-34)$$

When the diffusion flux is wholly known,  $f_C$  represents the known value of the flux while  $f_P$  is set to zero. On the other hand, when the diffusion flux is known as a linear function of  $\phi_B$ , both  $f_C$  and  $f_P$  are set to non-zero. When the flux is a non-linear function of  $\phi_B$ ,  $f_C$  and  $f_P$  depend on  $\phi_P$  and they should be then iteratively updated (linearization) as detailed earlier in section 4.2.

## 4.6 SOLUTION PROCEDURE

The solution procedure employed is a combination of the line-by-line method and a block correction scheme [Patankar (1980)].

### 4.6.1 Line-by-line method

In the discretization equation, the y-direction neighbours  $\phi_N$  and  $\phi_S$  are considered tentatively known, then the equations would only have three unknowns,  $\phi_P$ ,  $\phi_E$  and  $\phi_W$ . If such three-unknown equations are formed along an x-direction line, their form would be:

$$a_i \phi_i = b_i \phi_{i+1} + c_i \phi_{i-1} + d_i \quad \text{for } i=2, L2 \quad (4-35)$$

where  $\phi_i$ ,  $\phi_{i+1}$  and  $\phi_{i-1}$  denote  $\phi_P$ ,  $\phi_E$  and  $\phi_W$  respectively.

The coefficients are related by the following:

$$a_i = a_p$$

$$b_i = a_E$$

$$c_i = a_W$$

$$d_i = a_N \phi_N^* + a_S \phi_S^* + b$$

$\phi^*$  denotes an estimated value. Because of the boundary modifications, the coefficients  $c_2$  and  $b_{L2}$  are zero.

The line-by-line method consists of employing the Tri-Diagonal-Matrix Algorithm (TDMA) along the lines in the  $x$ -direction. This is then repeated in the  $y$ -direction. As the new values of  $\phi$  along a line are calculated, they are used as the estimates  $\phi^*$  in the line solution for the next line. The sequence in which the lines are chosen is as follows: Firstly, the line traverse is made along the  $x$ -direction line just above the bottom boundary. Then, the successive parallel lines up to the top boundary are visited. The same lines are then traversed in a top-to-bottom sweep direction. This is followed by the TDMA traverses along the  $y$ -direction lines using a left-to-right sweep followed by a right-to-left sweep. This practice is intended to bring the influence of all the boundary values quickly into the interior of the calculation domain.

#### 4.6.2 Block-correction method

The speed of convergence of the line-by-line method is further enhanced by a block-correction method. The central idea of the block-correction scheme is that an unconverged field  $\phi_{i,j}^*$  obtained from prior iterations is corrected by adding uniform corrections  $\bar{\phi}_i$  along lines of constant  $i$ . The equation is given as:

$$\phi_{i,j} = \phi_{i,j}^* + \bar{\phi}_i \quad (4-36)$$

The correction  $\bar{\phi}_i$  is chosen such that the integral conservation over the control-volume blocks defined by each constant- $i$  line is exactly satisfied. The equation governing  $\bar{\phi}_i$  is expressed as:

$$BL(I) \bar{\phi}_i = BL(I) \bar{\phi}_{i+1} + BL(I) \bar{\phi}_{i-1} + BLC(I) \quad (4-37)$$

where

$$BL(I) = \sum_{j=2}^{j=M/2} (a - d - e)$$

$$BLP(I) = \sum_{j=2}^{j=M/2} b$$

$$BLM(I) = \sum_{j=2}^{j=M/2} c$$

$$BLC(I) = \sum_{j=2}^{j=M/2} (b - d - e)$$

$BLC(I)$  represents the integral residual for the block around a constant- $i$  line. The corrections  $\bar{\phi}_i$  reduce all the integral residuals to zero. In short, when the block corrections are made, the corrected field of  $\phi$  implies perfect integral conservation of heat, mass and momentum etc. over each block. A similar procedure applies for lines of constant- $j$ .

Repetitions of the solution algorithm are done to obtain the converged solution. When, in a given pass through the solution algorithm, the local relative error,  $\varepsilon$ , is found to be everywhere less than or equal to  $10^{-5}$ , subsequent repetitions of the algorithm are halted.

The local relative error is defined as:

$$\varepsilon = \left| \frac{(RES)}{(TERM)} \right| \quad (4-38)$$

where  $RES$  is the residual of the discretization equation and  $TERM$  is the largest of all the terms in the discretization equation.

$RES$  is given as:

$$RES = b\phi_{i+1,j}^* + c\phi_{i-1,j}^* + d\phi_{i,j+1}^* + e\phi_{i,j-1}^* - a\phi_{i,j}^* \quad (4-39)$$

The repetitions (inner iterations) in the code give the solution of the linear algebraic equations. The outer iterations are for the recalculation of the coefficients to account for non-linearity. In the following, the term "iteration" implies the outer iteration.

For non-linear problems like the Poisson-Boltzmann equation, the coefficients in a given discretization equation depend on  $\phi$ . Iteration is hence needed. Taking the Poisson-Boltzmann equation as an example, the idea is discussed next. Firstly, an estimation of the electric field is done at all grid points. Treating this as the known electric potential field, the tentative values of the coefficients in the discretization equation are then calculated. The equations are solved to obtain a new electric potential field. Regarding this as a better estimation for the electric potential field, the coefficients are recalculated and the equation is solved again. In short, at any given stage, the discretization coefficients are calculated from the current estimates of all the  $\phi$  values. The solution of the discretization equation gives an improved estimation, which is used to recalculate the coefficients. This process is repeated until the solution ceases to change from iteration to iteration. Converged solution is then said to have achieved under a specific convergence criterion.

Under-relaxation is used in view of the possibilities of the divergence of the iterative process. With under-relaxation, the changes in the coefficients from iteration to iteration are reduced.

For under-relaxation, the general discretization equation is redefined as:

$$(a_p + i)\phi_p = \sum a_{nb}\phi_{nb} + b + i\phi_p^* \quad (4-40)$$

where the initial,  $i$ , is chosen as:

$$i = \frac{(1-\alpha)}{\alpha} \sum a_{nb} \quad (4-41)$$

where  $\alpha$  is the relaxation factor, in the code, value of  $\alpha$  from 0.05~ 0.20.

As  $\alpha$  gets closer to zero, the changes in  $\phi$  are greatly slowed down. Over-relaxation is introduced if  $\alpha > 1$ . On the other hand, no under-relaxation is introduced when  $\alpha = 1$ .

#### 4.7 TREATMENT OF NONLINEAR SOURCE TERM

As shown in Chapter 3, there are a number of highly nonlinear terms associated with the Nernst-Planck equations (equations 3-13, 3-14) and Z-direction momentum equation (equations 3-31). It is thus important to linearize these nonlinear sources terms and adding under-relaxation to the source terms, so as to avoid diverging of the solution. The basic principle of linearization is as follows:

$$S_{n+1}^* = S_n + \sum \frac{\partial S}{\partial \phi_i} \phi_i \quad (4-42)$$

where  $S_{n+1}^*$  is the source term after linearization. Therefore the source terms mentioned above are linearized as follows:

$$\begin{aligned}
& \left( \begin{aligned} & + \frac{1}{Sc^+ Re} \left[ \frac{\partial}{\partial x} \left( \overline{n^+} \frac{\partial \psi}{\partial x} \right) + \frac{\partial}{\partial y} \left( \overline{n^+} \frac{\partial \psi}{\partial y} \right) + \frac{\partial}{\partial z} \left( \overline{n^+} \frac{\partial \psi}{\partial z} \right) \right] \\ & + \frac{1}{Sc^- Re} \left[ \frac{\partial}{\partial x} \left( \overline{n^-} \frac{\partial \psi}{\partial x} \right) + \frac{\partial}{\partial y} \left( \overline{n^-} \frac{\partial \psi}{\partial y} \right) + \frac{\partial}{\partial z} \left( \overline{n^-} \frac{\partial \psi}{\partial z} \right) \right] \\ & - \overline{G_1 E_z} \overline{\rho_e} \end{aligned} \right)_{n+1}^* \\
= & \left( \begin{aligned} & + \frac{1}{Sc^+ Re} \left[ \frac{\partial}{\partial x} \left( \overline{n^+} \frac{\partial \psi}{\partial x} \right) + \frac{\partial}{\partial y} \left( \overline{n^+} \frac{\partial \psi}{\partial y} \right) + \frac{\partial}{\partial z} \left( \overline{n^+} \frac{\partial \psi}{\partial z} \right) \right] \\ & + \frac{1}{Sc^- Re} \left[ \frac{\partial}{\partial x} \left( \overline{n^-} \frac{\partial \psi}{\partial x} \right) + \frac{\partial}{\partial y} \left( \overline{n^-} \frac{\partial \psi}{\partial y} \right) + \frac{\partial}{\partial z} \left( \overline{n^-} \frac{\partial \psi}{\partial z} \right) \right] \\ & - \overline{G_1 E_z} \overline{\rho_e} \end{aligned} \right)_n + \\
& \left( \begin{aligned} & + \frac{1}{Sc^+ Re} \left[ \overline{n^+} \frac{\partial}{\partial x} \left( \frac{\partial \psi}{\partial x} \right) + \overline{n^+} \frac{\partial}{\partial y} \left( \frac{\partial \psi}{\partial y} \right) + \overline{n^+} \frac{\partial}{\partial z} \left( \frac{\partial \psi}{\partial z} \right) \right] \\ & + \frac{1}{Sc^- Re} \left[ \overline{n^-} \frac{\partial}{\partial x} \left( \frac{\partial \psi}{\partial x} \right) + \overline{n^-} \frac{\partial}{\partial y} \left( \frac{\partial \psi}{\partial y} \right) + \overline{n^-} \frac{\partial}{\partial z} \left( \frac{\partial \psi}{\partial z} \right) \right] \\ & - \overline{G_1 G_2} \left( \frac{D_h}{W_c} \right) \left( \frac{D_h}{L_c} \right) \overline{\rho_e} \int \overline{\rho_e} d\overline{A} \end{aligned} \right)_n \quad (4-43)
\end{aligned}$$

The source term is further relaxed as follows:

$$S_{n+1} = \beta S_{n+1}^* + (1 - \beta) S_n \quad (4-44)$$

where  $S_{n+1}$  is the updated source term used in the new iteration and  $\beta$  is the relaxation factor for the source terms. In this work,  $\beta=0.85$  was used. In all, by introducing the above linearization and relaxation the code is stable in the computation.



## Chapter Five

### VALIDATION OF CODE

#### 5.1 VALIDATIONS OF FLOW FIELD

##### 5.1.1 Velocity Profile

Based on a classical model [Weisberg et. al. (1992)], comparisons were made between the non-dimensional velocity field obtained from the classical expressions (equation 5-1) for a fully-developed laminar water flow in a rectangular duct (as shown in Figure 5.1) and that of the current in-house developed code, also the fully developed region. The coordinate system of the current code was modified so that direct comparison with the classical expression can be made.

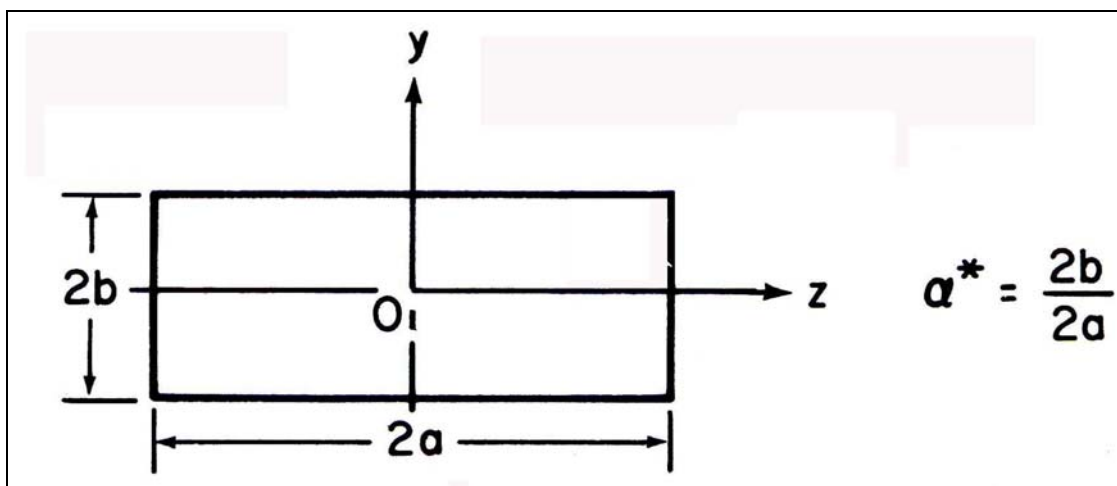


Figure 5.1 The rectangular duct model used for classical analysis

The only boundary condition stated was the zero velocity at channel wall. The cross section of rectangular is characterized by aspect ratio  $\alpha^*=2b/2a$ . The parameters used in the comparison are listed in Table 5.1.

Table 5.1 The parameters of the microchannel used for velocity profile comparison

Width, 2a	60 μm
Length, 2b	30 μm

The classical expression for the non-dimensional velocity field where  $\alpha^* \leq 0.5$  is expressed as [Weisberg et. al. (1992)]:

$$u(x, y) = \frac{48}{\pi^3} \left[ 1 - \frac{96}{\pi^5 b} \sum_{i=1,3,5,\dots}^{\infty} \frac{\tanh(\frac{i\pi b}{2a})}{i^5} \right] \sum_{i=1,3,5,\dots}^{\infty} (-1)^{\frac{i-1}{2}} \left[ 1 - \frac{\cosh(\frac{i\pi y}{2a})}{\cosh(\frac{i\pi b}{2a})} \right] \frac{\cosh(\frac{i\pi x}{2a})}{i^3} \quad (5-1)$$

1)

The non-dimensional velocity field from classical expressions is shown in Figure 5.2 while the non-dimensional velocity profile obtained from the code is illustrated in Figure 5.3.

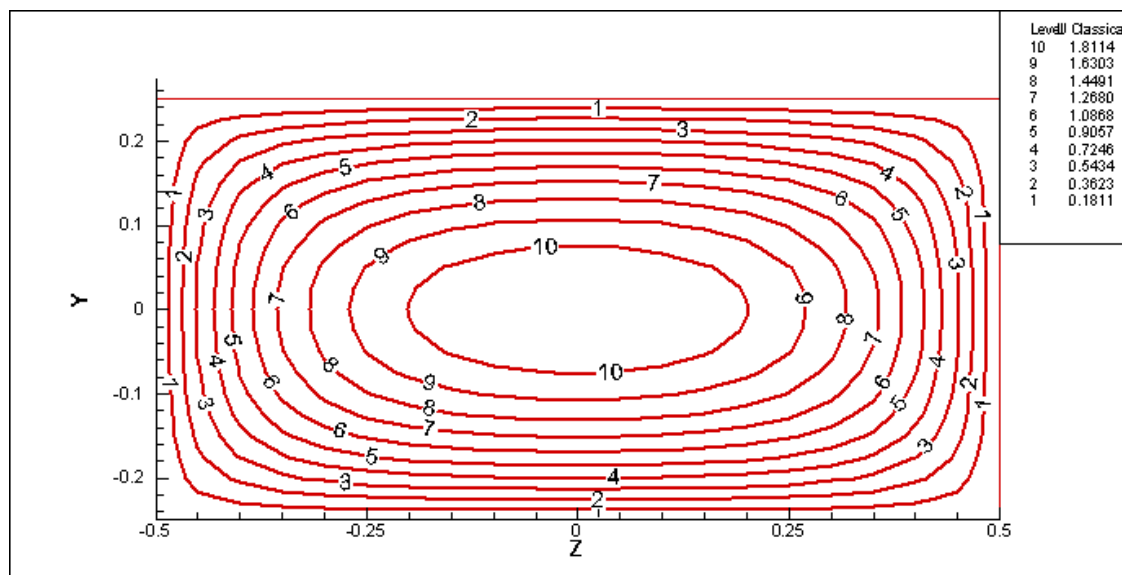


Figure 5.2 Non-dimensional velocity profiles from classical expressions

[Weisberg et. al. (1992)]

The velocity scale used in the classical expressions is the cross-sectional averaged velocity,  $u_{ave}$  while the velocity scale used in the code is unity. The length scale used in the classical expressions is the channel height while the length scale used in the code is the hydraulic diameter of the channel. Hence, as basis for comparison, the velocity scale in the code is changed to  $u_{ave}$  for better comparison. Table 5.2 shows the non-dimensional velocity values at various coordinates based on Figure 5.1. The numerical values of the non-dimensional velocity agree well with the classical values within 0.15% as shown in Table 5.2 and Figure 5.4.

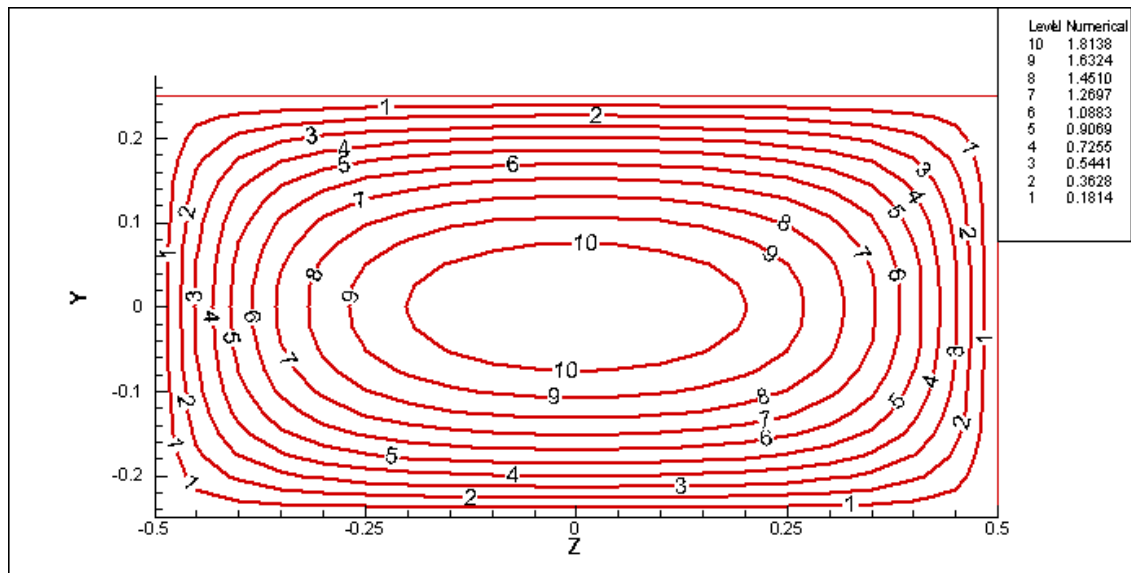


Figure 5.3 Non-dimensional velocity profiles from current code

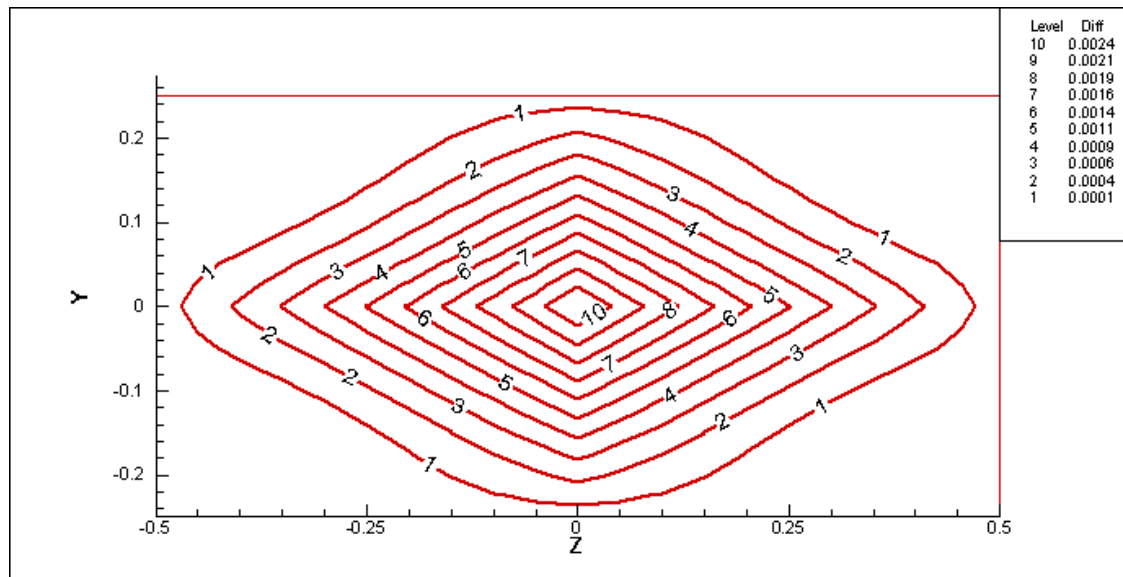


Figure 5.4 The difference of nondimensional velocity values between prediction using current code and classical expressions

Table 5.2 The difference of nondimensional velocity values between prediction using current code and classical expressions

No.	X-coordinate	Y-coordinate	Classical	Numerical	%Error
1	0	0	1.9919	1.9945	0.15
2	0	0.25	1.6710	1.6721	0.07
3	0	0.45	0.5889	0.5891	0.03

### 5.1.2 Friction coefficient

Comparisons were also made between the values of friction coefficient values for the conventional fully developed flow in rectangular ducts (single channel) where water is used as the working fluid. The analytical data were obtained from Shah & London (1978). The physical model is shown in Figure 5.1 and the boundary condition is same as that used in section 5.1.1. The computed numerical values of  $fRe$  [Equation (3-29)] agree well with the exact solution to within 0.3% as presented in Table 5.3.

Table 5.3 Comparisons between numerical and exact solutions of  $fRe$

No	Aspect ratio ( $\alpha^*$ )	Numerical results	Shah & London (1978)	% Error
1	1.00	14.23851	14.22708	0.080 %
2	0.75	14.513858	14.47570	0.296%
3	0.67	14.74027	14.71184	0.193%
4	0.50	15.50741	15.54806	-0.261%
5	0.30	17.46924	17.51209	-0.245%

where aspect ratio,  $\alpha^*=2b/2a$

## 5.2 VALIDATIONS OF THERMAL FIELD

For thermal field, comparison was made between the classical analytical data obtained from Shah and London (1978) and the prediction by current code at fully developed region, based on Nusselt number,  $Nu$ . The physical model and flow condition used by classical analytical data was same as the flow condition mentioned in section 5.1 (as shown is Figure 5.1). The thermal boundary condition was stated as a constant heat flux  $q'$  at wall.

Table 5.4 Comparisons of  $Nu$  between the numerical and exact solutions

No	Aspect ratio ( $\alpha^*$ )	Numerical results	Shah & London (1978)	% Error
1	1.00	3.62033	3.60795	0.343 %
2	0.75	3.68734	3.70052	-0.356%
3	0.67	3.77943	3.79033	-0.288%
4	0.50	4.13670	4.12330	0.325%
5	0.30	4.96215	4.98989	-0.556%

where aspect ratio,  $\alpha^*=2b/2a$

The computed numerical values of Nusselt number,  $Nu$  using equation 3-36 and classical analytical data are tabulated in Table 5.4. It is found that the numerical values agree very well with the classical analytical data and the error is within 0.6%.

### 5.3 VALIDATIONS OF ELECTRICAL FIELD

The validation of electrical field was done using electrical potential across the cross-sectional area of the channel at fully developed area. Comparison was made between analytical prediction by Patankar and Hu (1998) and numerical prediction by current code. Note that several assumptions were made in the analytic prediction:

1. The electrical field was fully developed.
2. The Debye-Huckel approximation was applied; it implied that the flow is subjected to a small electrical potential. For 2-D model, equation 3-20 was thus simplified to equation 5-2

$$\frac{\partial^2 \psi}{\partial y^2} = K^2 \psi \quad (5-2)$$

2)

3. A 2-D model was used in the analysis. Therefore aspect ratio is close to zero.

The classical expression for the non-dimensional electrical potential distribution was expressed as:

$$\psi(y) = \left( 1 - \frac{\cosh[\kappa(y - 0.5)]}{\cosh[0.5\kappa]} \right) \quad (5-3)$$

3)

With the example,  $\kappa=20$  and aspect ratio =0.1 being applied in the current code, The numerical values of the nondimensional velocity agree well with the classical values to within 0.5% as included in Table 5.5 and Figure 5.4.

Table 5.5 Comparisons between the numerical and analytical solutions of  $\psi$ 

No	y-coordinate	Numerical results	Patankar and Hu (1998)	% Error
1	0.05	0.367879	0.369436	0.423%
2	0.1	0.135335	0.135762	0.315%
3	0.2	0.018316	0.018355	0.216%
4	0.3	0.002480	0.002483	0.141%
5	0.4	0.000914	0.000915	0.112%

where aspect ratio,  $y=Y/H_c$

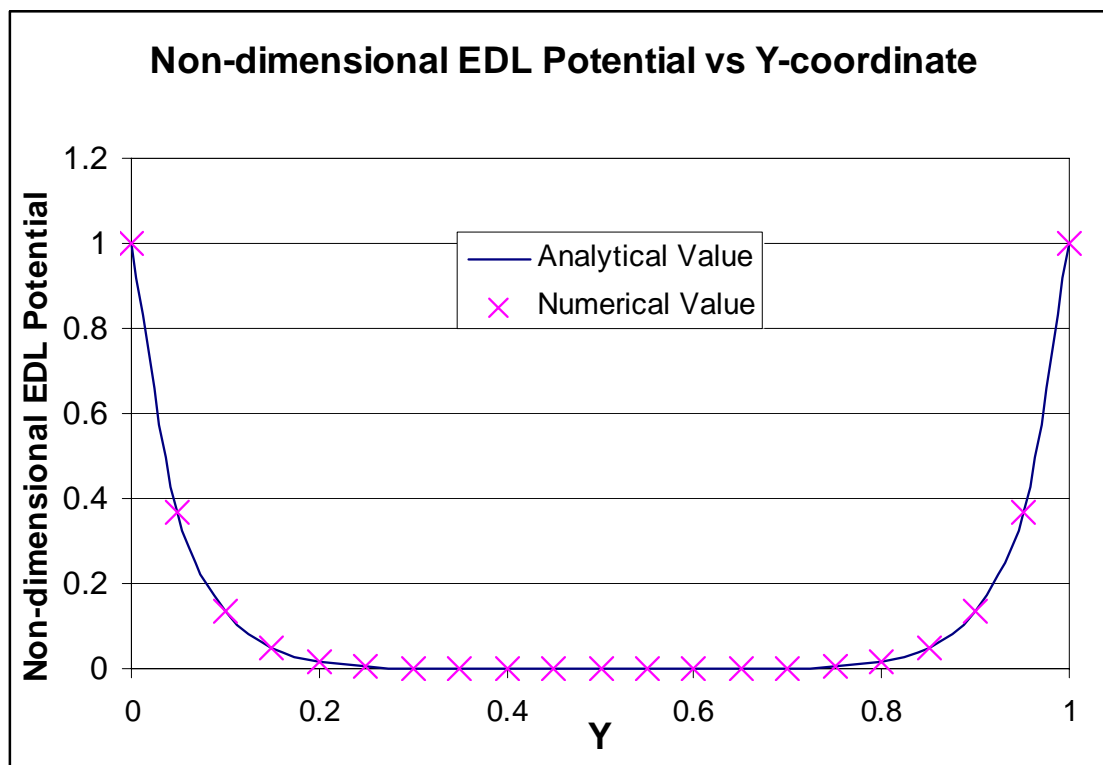


Figure 5.5 Comparison between electrical potential predicted by numerical and analytical prediction



## 5.4 COMPASION WITH OTHER EDL WORKS

### 5.4.1 Yang and Li (1998)

Yang and Li (1998) presented the prediction of friction coefficient at different aspect ratio, in the present of EDL effect. The flow field was predicted based on 3-D fully developed flow, solved using analytical method. The flow field was modeled based on rectangular microchannel with a width of  $30\mu\text{m}$  and length of  $1\text{cm}$ , the height was varied with the aspect ratio as shown in Figure 5.6. The results are compared with that predicted with the code developed by the author. As shown in Figure 5.6, the results predicted by the author agree with the prediction by Yang and Li for both  $\xi$  equal to 50 and 75 mV with Debye-Huckel parameter,  $\kappa$  equal to 24.7. The error was found within 2%.

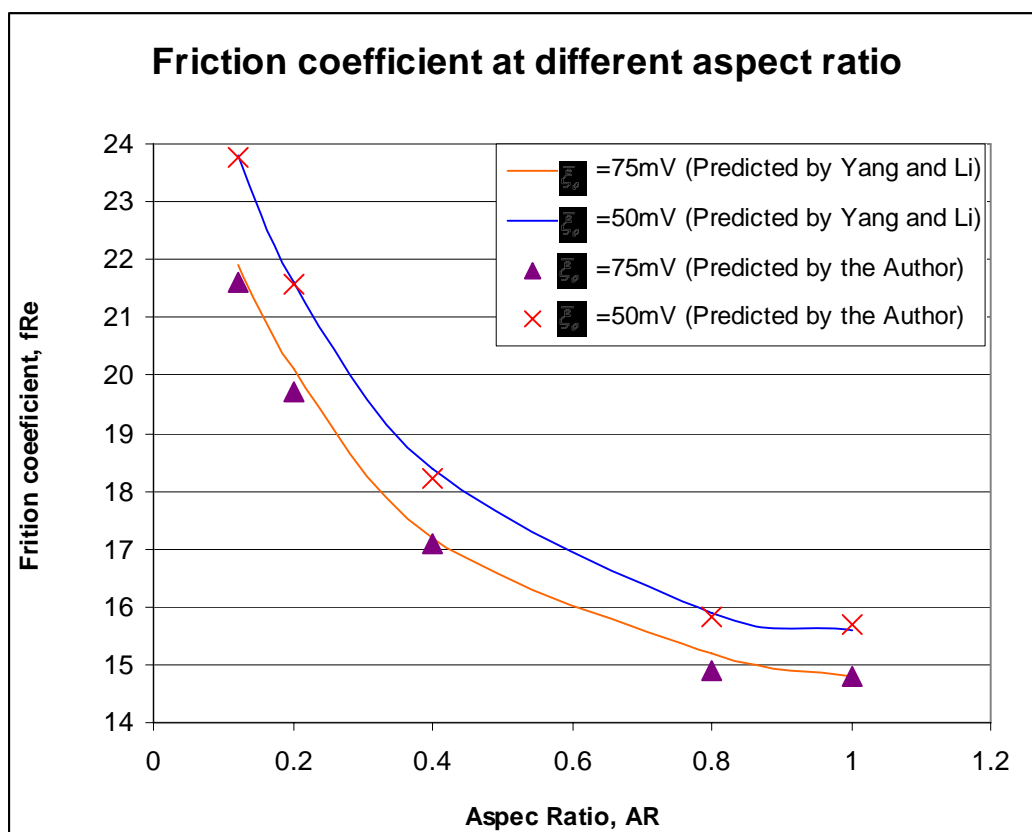


Figure 5.6 Comparison between electrical potential predicted by Yang and Li (1998) and the current code

### 5.4.2 Ng and Poh (2000)

Another work related to friction coefficient at different aspect ratio was presented by Ng and Poh (2000) with another set of parameters. The results was presented based on the aspect ratio value large than therefore is reciprocal of aspect ratio defined in section 5.4.1.

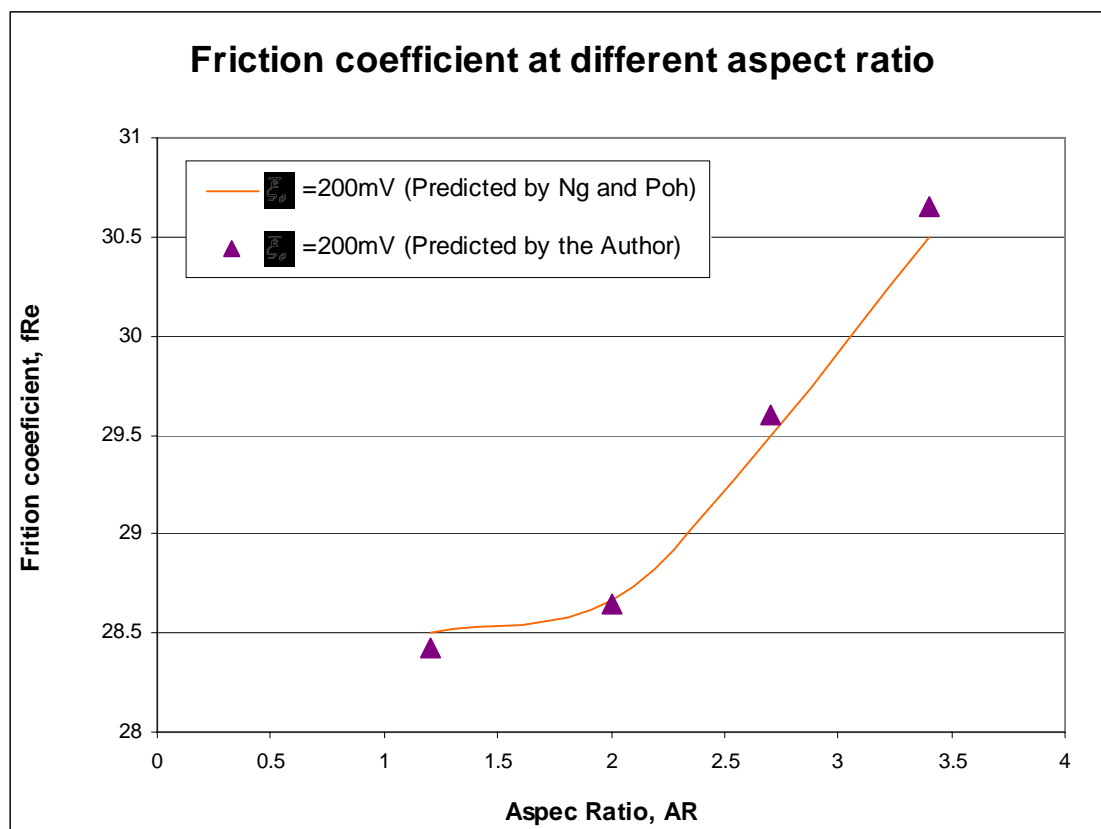


Figure 5.7 Comparison between electrical potential predicted by Ng and Poh (2000) and current code

The flow field was also predicted based on 3-D fully developed flow using numerical method. The rectangular microchannel was chose to model the flow field. The width and length of the microchannel was 20 $\mu$ m and 1000  $\mu$ m respectively, the height was varied with the aspect ratio as shown in Figure 5.7. The wall electrical potential was 200mV and molar concentration of the solution is 10<sup>-8</sup>M (Potassium

Chloride, KCl solution). With comparison to with the result predicted by Ng and Poh (2000), as included in Figure 5.7, the agreement by the current results within 5%.

## 5.5 VALIDATIONS OF GRID

In this project, the flow field was model with grids of  $10 \times 20 \times 60$  mesh in X, Y and Z direction respectively. The two critical regions are the near wall region and the flow developing region, where important variable such as velocity, temperature and electrical potential change rapidly. The value of friction coefficient,  $fRe$  at grid point (20, 40, 3) is used to check the robustness of the chosen mesh size.

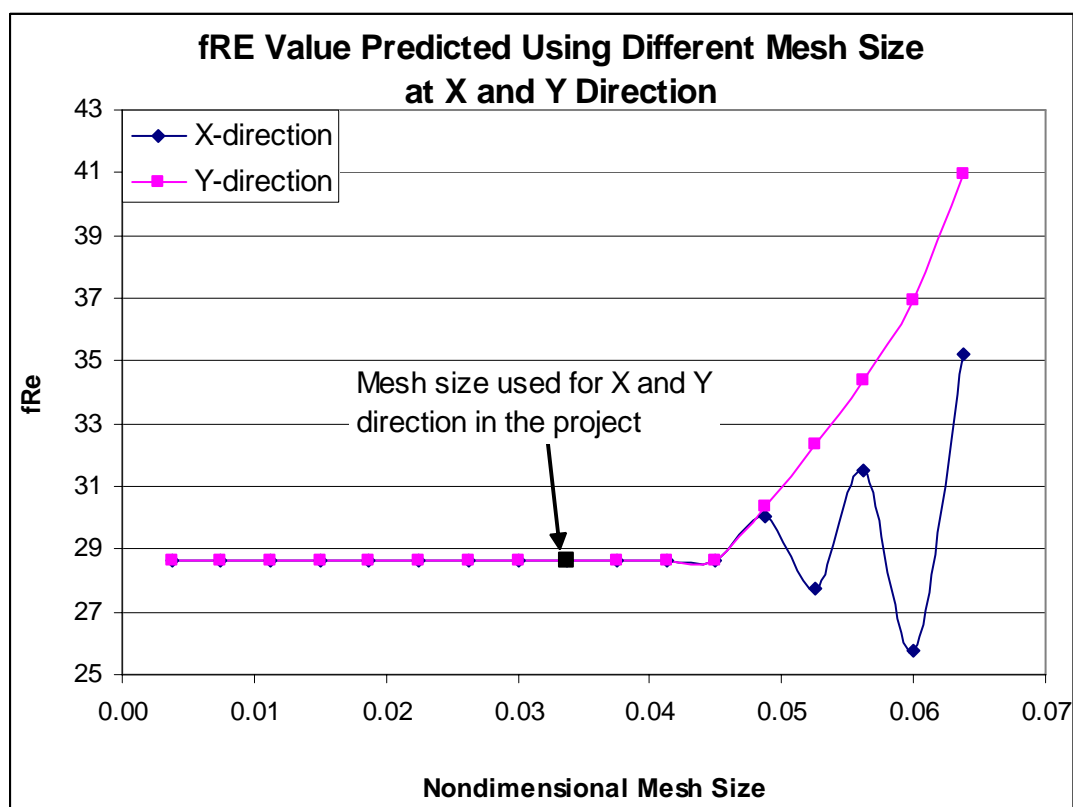


Figure 5.8  $fRe$  values predicted using different mesh size at X and Y direction

Figure 5.8 and Figure 5.9 show the predicted  $fRe$  value at grid point (20, 40, 3) at value at different mesh size. As shown in Figure 5.8 the nondimensional mesh

dimensions of 0.045 are sufficient to be used to predict precise values in X and Y dimensions. On the other hand, for Z dimension of the nondimensional mesh size, as shown in Figure 5.9, it is found that a dimension of 0.25 is sufficient to predict the  $fRe$  value precisely.

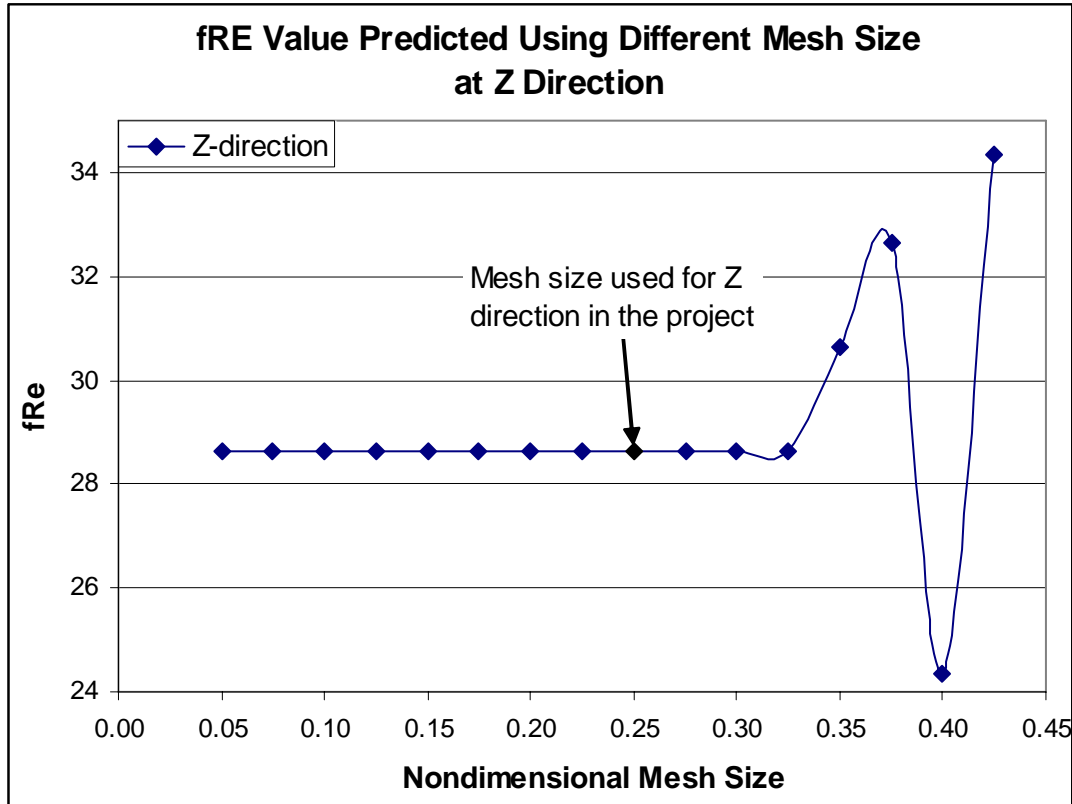


Figure 5.9  $fRe$  values predicted using different mesh size at Z direction

## Chapter Six

### RESULTS AND DISCUSSION

With the equations derived in Chapters 3 and the numerical scheme presented in Chapter 4, analysis on 3-D microchannel developing flow with EDL was performed. In the analysis friction coefficient (equation 3-19),  $fRe$  will be used to analyze the flow field at near wall region while velocity at center of channel is another variable to analyze the flow field at the main stream. On the other hand, Nusselt number is the performance index of the heat transfer for a microchannel. The computation was done on a PC platform using Mobile Intel Pentium® 4, 1.99GHz with 256 MB RAM. Unless stated, the working fluid is Potassium Chloride (KCl) solution, with viscosity ( $\mu_f$ ) of  $0.90 \times 10^{-3} \text{ Kg m}^{-1}\text{s}^{-1}$ , density ( $\rho_f$ ) of  $997 \text{ Kg m}^{-3}$ , dielectric constant( $\varepsilon$ ) of 78.5 and thermal conductivity ( $k_f$ ) of  $0.613 \text{ W m}^{-1}\text{K}^{-1}$ . The aspect ratio of the microchannel used was 0.5 unless stated.

#### 6.1 Discrepancy between Predictions With and Without EDL Effect

##### 6.1.1 Comparison of the flow field with and without EDL effect

As known (equation 3-18) the electrical field strength,  $\overline{E_z}$  is induced to oppose the electrical streaming current and the EDL body force,  $F_{EDL}$ , is thus expected to have the nature in opposing the flow. We next study results predicted with and without EDL for the same geometry and similar flow settings. For the case with EDL effect, the wall electrical potential  $\overline{\xi}_o$  is equal to 4 and  $K$  value is 78.12 ( $\overline{\xi}_o$  and  $K$  are dimensionless terms).

Figure 6.1 and Figure 6.2 show the nondimensional velocity plots for flow fields with and without EDL effect respectively. The two sets of prediction suggest similarities in trend. At  $z=0$  (the lowest plane), the magnitude of velocity in  $z$ -direction is shown as one, which is the inlet velocity (boundary condition). As the flow progress, the velocity of the liquid next to wall become zero, while the nondimensional velocity of the fluid at center increases and is more than one. Over the cross-sectional area in stream direction, the magnitude of velocity reveals parabola distribution, which is a typical phenomenon of developing flow.

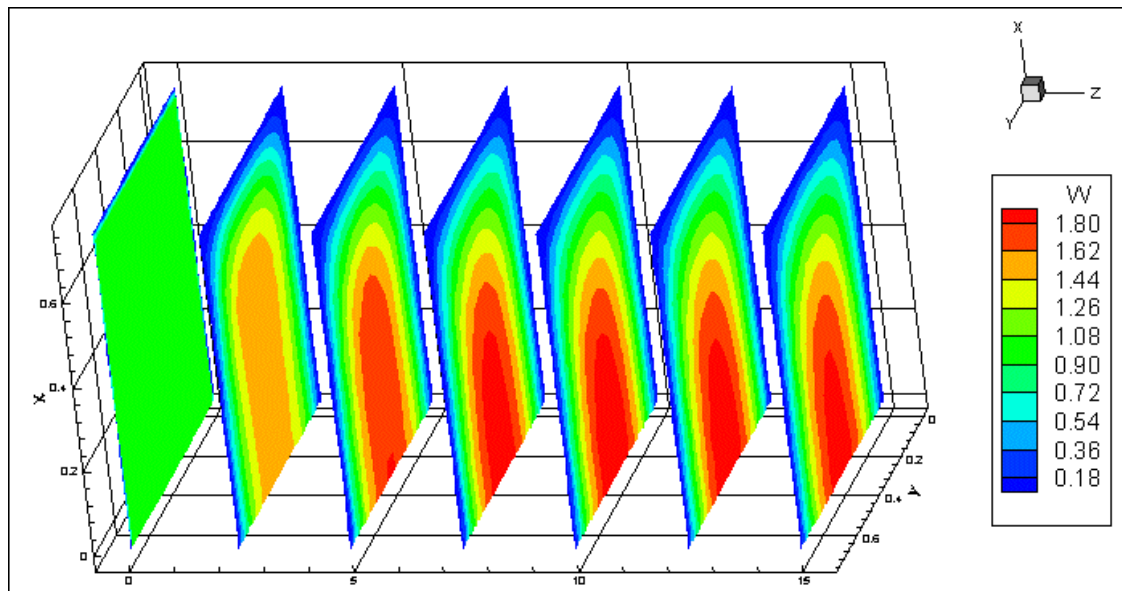


Figure 6.1 Typical 3-D nondimensional velocity plot flow field with EDL effect

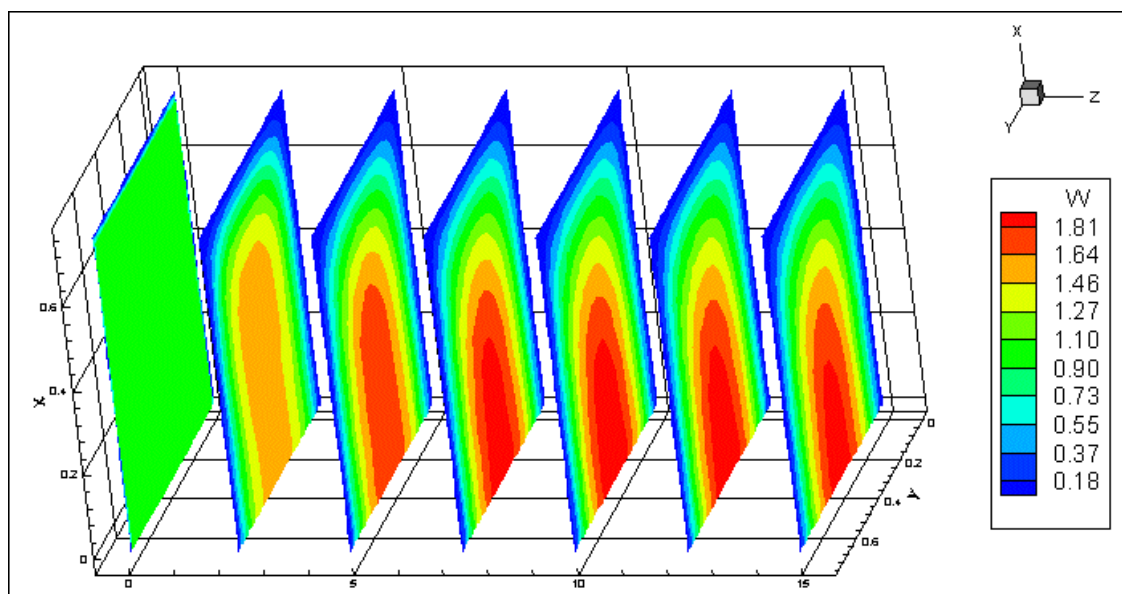


Figure 6.2 Typical 3-D nondimensional velocity plot for flow field without EDL effect

However, the discrepancy between the flow field with and without EDL is shown by the difference in the magnitude of the nondimensional velocity at same location. The velocity of fluid at the center of the channel for flow field with EDL effect (1.9939, at fully developed region, where percentage change of the dimensionless velocity less than 1%) has a slightly lower value (only 0.60%) as compared to the flow field without EDL effect (2.0059 at fully developed region). But the velocity distribution of the flow field with EDL effect is steeper at near wall region through smoother at near center region of the channel. The steeper near wall velocity and higher center velocity indicates a typical phenomenological evidence of higher viscosity.

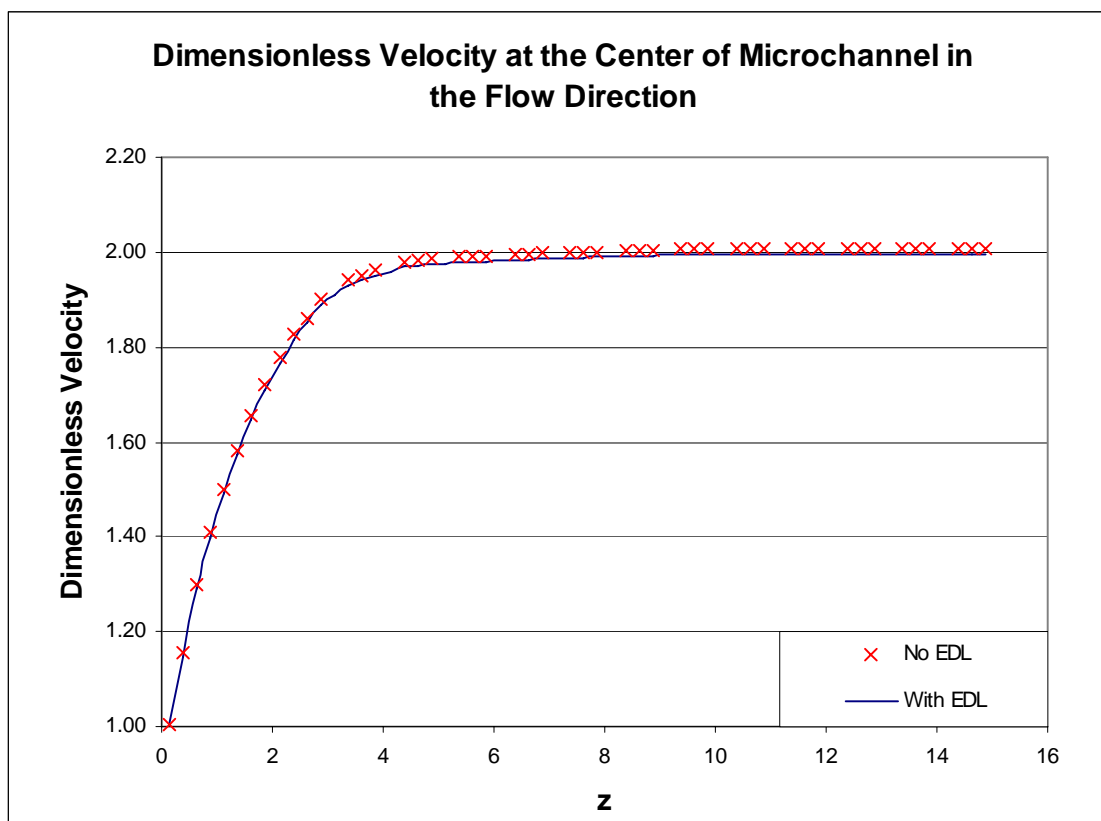


Figure 6.3 Predicted dimensionless velocity  $w$  values along  $Z$  direction for flow field with and without EDL effect

Due to the attraction between the wall potential and the ions in the fluid, the EDL effect tends to restrict the motion of near wall ions. Hence, the near wall fluid flow will be further ‘held-back’. This effect of slowing down the near wall fluid molecules is acting in addition of the viscosity effect. As the mass flow has to conserve throughout the channel, the fluid velocity at the channel center will increase. As this phenomenon is very similar to the viscosity effect, the EDL effect can thus be considered equivalent to the effect of higher viscosity as compared to a flow field without EDL effect. Figure 6.3 and Table 6.1 indicate that the  $fRe$  value of flow field with EDL effect (16.8559 fully developed region) is generally 8.70% higher than that



without EDL effect (15.5074 at fully developed region). Similar trend based on 2-D developed flow model was also reported by Ng and Poh (2002).

Table 6.1 Comparison of the result of flow field predicted with and without EDL effect

Predicted parameters	With EDL	No EDL	% difference
Dimensionless velocity $w$ at center of microchannel in fully developed region	1.9939	2.0059	-0.60%
Friction coefficient $C_f$ at hot wall at fully developed region	16.8559	15.5074	8.70%

### 6.1.2 Comparison of the temperature field with and without EDL effect

The EDL also extends its effect from velocity field to temperature in a similar manner. Figure 6.4 and Figure 6.5 present the nondimensional temperature distribution in the microchannel for flow field with and without EDL effect respectively. Similar to the nondimensional velocity plots, Figure 6.4 and Figure 6.5 show similar distribution profile but different temperature. The high temperature wall (hot wall) of the channel is the surface where heat is transferred into the liquid, in which there is a rapid decrease in temperature and then followed by a gradual decrease in temperature towards the other three walls (cold adiabatic walls).

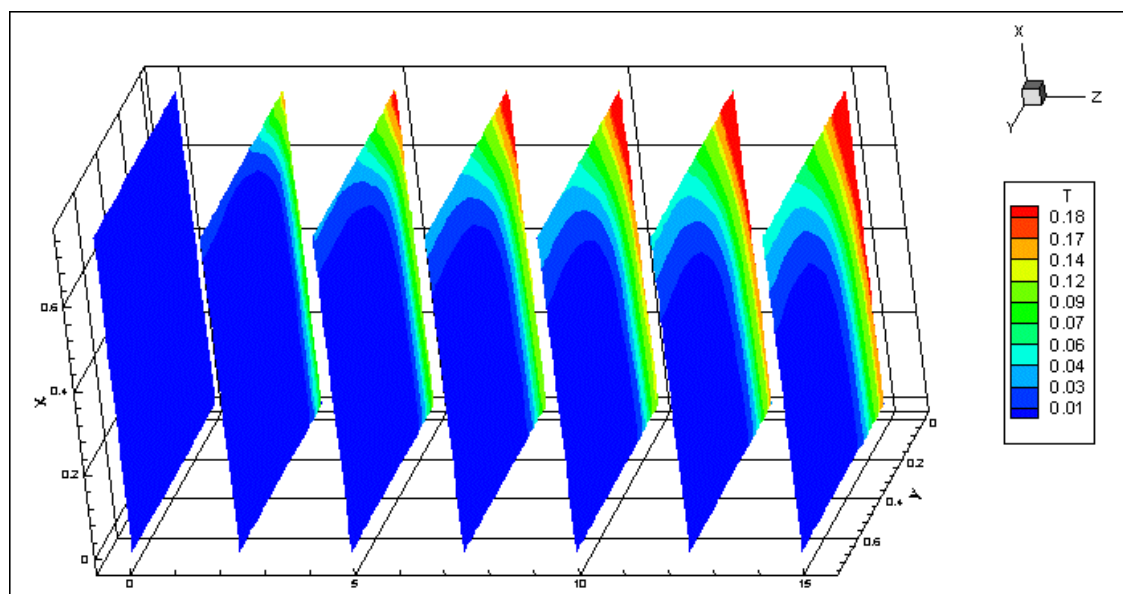


Figure 6.4 Typical 3-D nondimensional temperature plots for flow field with EDL effect

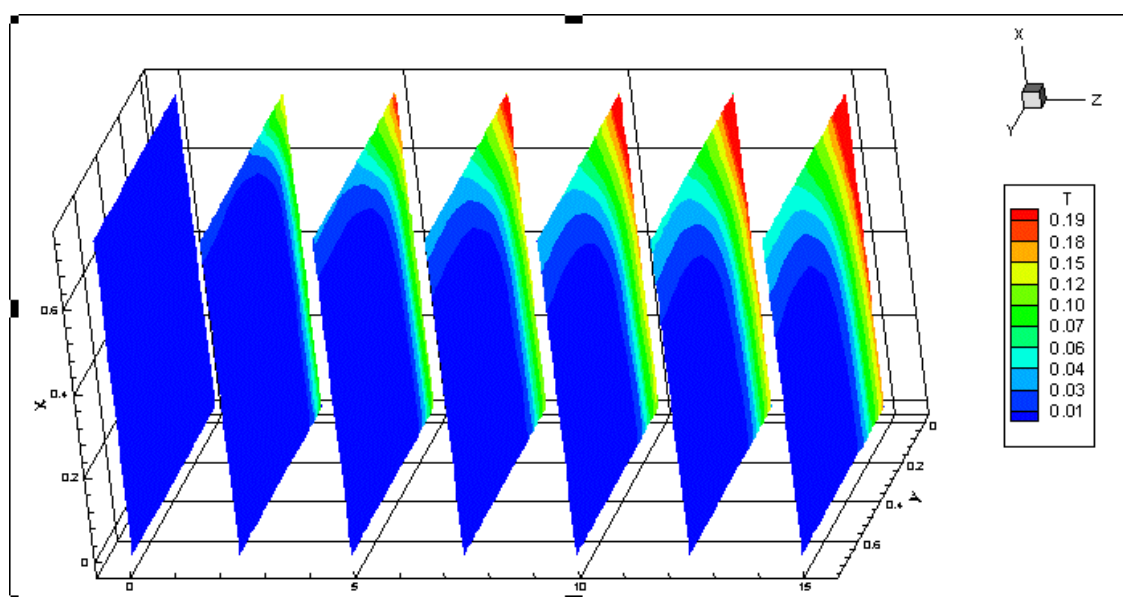


Figure 6.5 Typical 3-D nondimensional temperature plots for flow field without EDL effect

As shown in Figures 6.6, the dimensionless temperature for flow field at the hot wall, with EDL effect (0.0214 in the fully developed region) is 5.26% higher than that of without EDL effect (0.0203 in the fully developed region). As a result, the wall

temperatures of flow field with EDL effect are higher when transferring the same amount of heat.

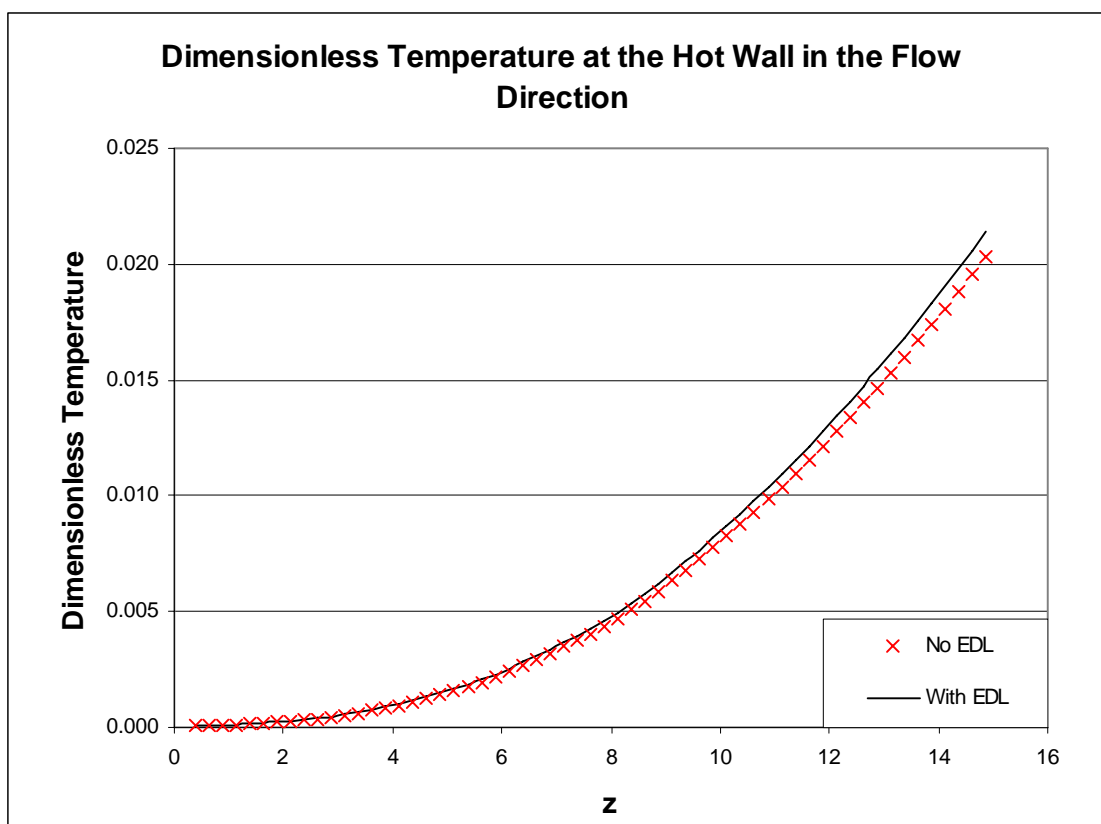


Figure 6.6 Predicted dimensionless temperature,  $\theta$  values along  $Z$  direction for flow field with and without EDL effect

Figure 6.7 shows that the predicted  $Nu$  value prediction with EDL (3.7298 in the fully developed region) is 9.84% lower than that without EDL effect (4.1367 in the fully developed region). Table 6.2 indicates that the predicted average  $Nu$  value in microchannel with EDL effect ( $Nu_{ave} = 4.5600$ ) is 12.26% lower than prediction without EDL effect ( $Nu_{ave} = 5.1970$ ). Hence the performance of the microchannel would be overestimated without considering the EDL effect. Figure 6.7 suggests that the  $Nu$  value in the developing region is significantly higher than the  $Nu$  value in the

fully developed region. Therefore developing flow is a very important region which cannot be ignored.

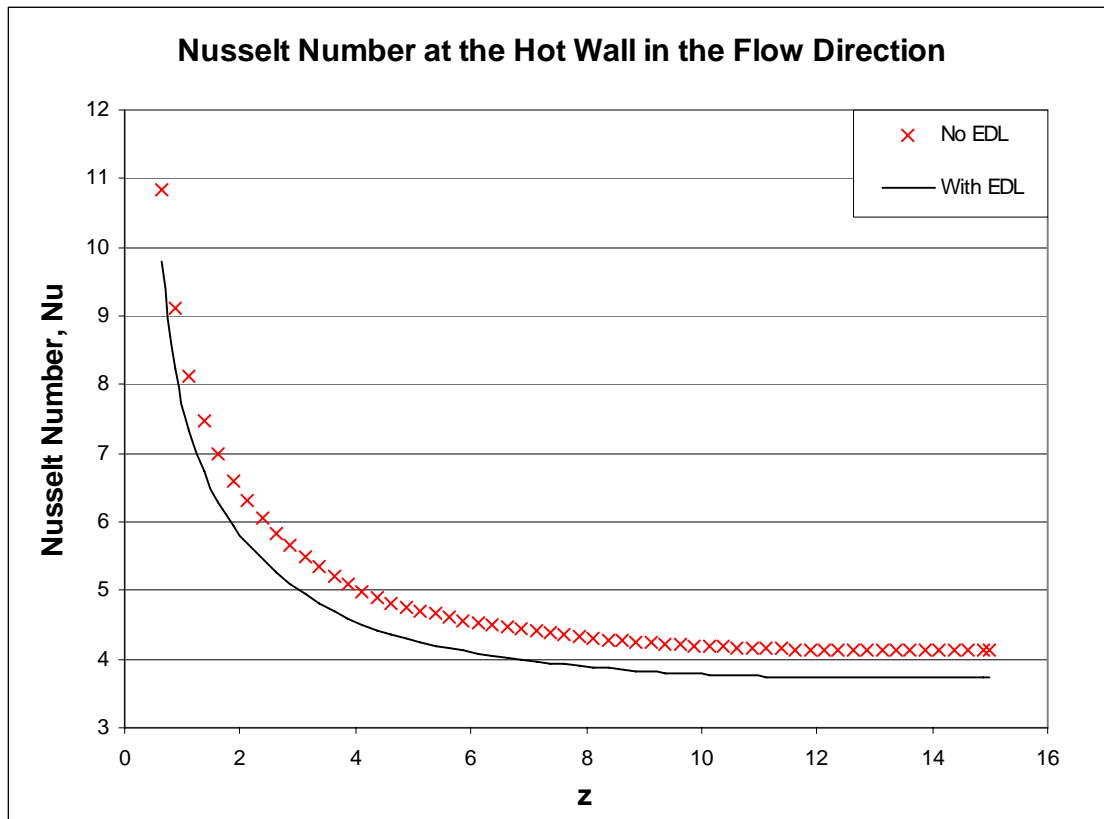


Figure 6.7 Nu values along Z direction for flow field with and without EDL effect

Table 6.2 Comparison of the result of the thermal field predicted with and without EDL effect

Predicted parameters	With EDL	No EDL	% difference
Dimensionless temperature $\theta$ at hot wall at fully developed region	0.0214	0.0203	5.26%
Local Nusselt $Nu_x$ at hot wall at fully developed region	3.7298	4.1367	-9.84%
Average Nusselt $Nu_{ave}$ of the microchannel	4.5600	5.1970	-12.26%

In brief, EDL effect is very important especially in the near wall region. The discrepancy of performance of microchannel such as  $fRe$  and  $Nu$  values can be as high as 10% between the prediction with and without EDL effect.

## 6.2 Discrepancy between Predictions by Different Models

In this study, the focus will be the comparison between prediction by Nernst - Planck model (NPM, in section 3.2.3) and Poisson-Boltzmann model (section 3.2.4). In NPM two partial differential equations (Nernst-Planck equation) based on conservation of charge, are used to describe the distribution of ion concentration. On the other hand, in PBM, Boltzmann distribution was used to describe the distribution of ion concentration. The NPM has been claimed to be more suitable for modeling EDL effect in the developing flow field. However PBM with its low computation time is an attractive model for estimating the performance of microchannels. Other than the parameters listed in Table 3-1, some extra parameters used for NPM and PBM in this section are listed in Table 6.3

Table 6.3 Parameters used for comparing the prediction by NPM and PBM

Model Parameters	Values
$k$ value	100
Schmidt No., $Sc$	$10^5$

### 6.2.1 Ion concentration

The fundamental difference between the PBM and NPM, is the approach used in predicting the dimensionless ion concentration distribution. In Figure 6.8, the distributions of dimensionless ion concentration predicted by PBM and NPM in  $y$ -direction and at the exit of microchannel are compared. The results are almost identical, except in the near wall region (i.e. the grid next to channel wall) in which the positive charge concentration predicted by NPM and PBM are 0.935 and 0.905 respectively, prediction by NPM is 4.5% higher than that predicted by PBM. For

negative charge concentration predicted by NPM and PBM are 1.07 and 1.13 respectively, prediction by NPM is 5.3% lower than that predicted by PBM.

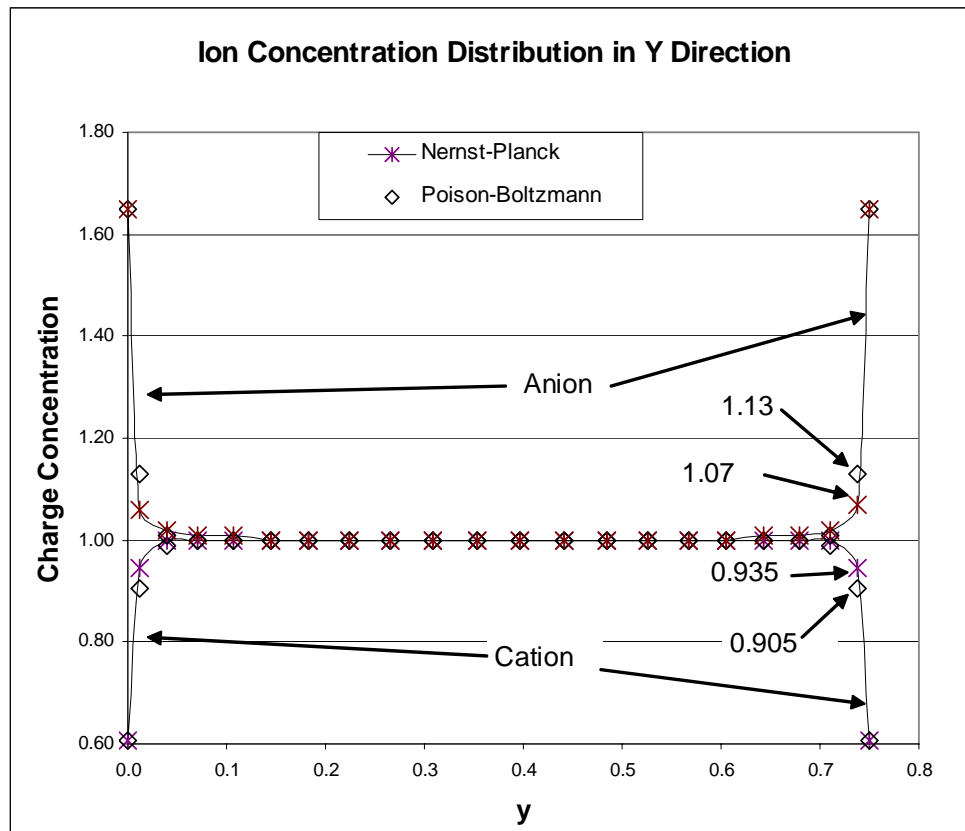


Figure 6.8 Cation and anion concentration distribution along y-direction, at the exit of microchannel

Due to the assumption of Boltzmann distribution of ion concentration in  $x$ ,  $y$ -plane, the ion concentration distribution in  $z$ -direction predicted by PBM is constant.

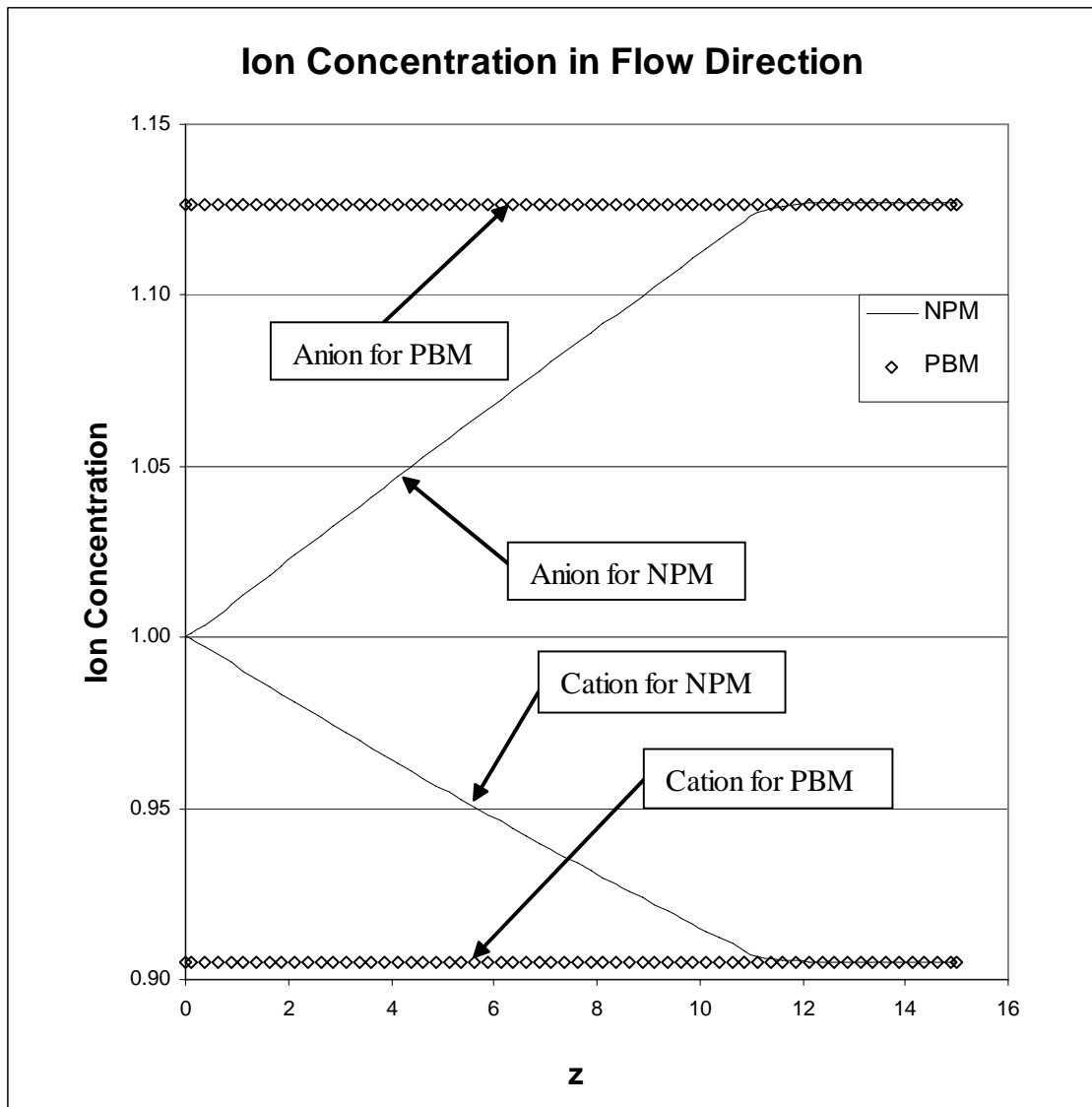


Figure 6.9 Cation and anion concentration distribution along  $z$ -direction at near wall grid

However, in NPM prediction, the dimensionless ion concentration changes from value of unity (inlet boundary condition,  $\overline{n^+}, \overline{n^-} = 1.0$ ) to a fully developed value of 1.13 and 0.91 for  $\overline{n^+}$  and  $\overline{n^-}$  respectively. The change is found to be nearly linear. The discrepancy of ion concentration distribution in  $z$ -direction of the two predictions in the near wall region, will affect the near wall shear stress, which can be reflected by the value of friction coefficient,  $C_f$ .

### 6.2.2 Friction Coefficient, $C_f$

Friction coefficient,  $C_f$ , is an important parameter to characterize the efficiency of a microchannel. It is defined as the product of friction factor ( $f$ ) and Reynolds number ( $Re$ ),  $fRe$ . In the conventional fluid mechanics, the friction factor for the flow through rectangular channels is defined as

$$f = \frac{-\frac{dP}{dZ} \frac{D_h}{4}}{\rho_f \frac{W_{ave}^2}{2}} = \frac{-\frac{dp}{dz}}{2 Re_o \frac{w_{ave}^2}{2}} \quad (6-1)$$

The friction coefficient,  $C_f$ , defined by means of the Fanning friction factor ( $f$ ) is thus given as

$$C_f = f Re = \frac{-\frac{dp}{dz}}{2 Re_o \frac{w_{ave}^2}{2}} Re_o = \frac{-\frac{dp}{dz}}{2 w_{ave}^2} \quad (6-2)$$

As shown in Figure 6.10, both NPM and PBM give the similar trend in friction coefficient distribution in the  $z$ -direction. High  $C_f$  value is found at inlet of the channel. As uniform velocity is defined as the inlet boundary condition, high velocity gradient is found at inlet near wall region, which leads to high shear stress and high friction. When the flow is fully developed, the  $C_f$  value stabilizes.

However, it is also found that the  $C_f$  values predicted by NPM and PBM have significant discrepancy. The  $C_f$  value at the hot wall in fully developed region predicted using NPM is around 3.38% lower than that predicted using PBM (16.8559 as compared to 17.4252 at fully developed region, see Table 6.4).



As shown in equation (6-2),  $C_f$  is affected by pressure gradient in  $z$ -direction,  $\frac{dp}{dz}$  and average  $z$ -direction velocity,  $w_{ave}$ . Since the inlet boundary condition,  $w = 1$  is set,  $w_{ave}$  has similar value in either PBM or NPM. As a result, the discrepancy in  $C_f$  value of the predictions by the two models is caused by the difference in pressure gradient. From equation (3-26), it is shown that  $\frac{dp}{dz}$  will be affected by the EDL body force, where  $F_{EDL} = -\bar{G}_1 \bar{E}_z \bar{\rho}_e$ . The  $\frac{dp}{dz}$  (positive value) represents the driving force but  $F_{EDL}$  (negative positive value) represents the opposing force. A larger  $F_{EDL}$  value will lead to a higher  $\frac{dp}{dz}$  and hence larger  $C_f$ .

The EDL body force,  $F_{EDL}$  as predicted by PBM is higher than that computed with NPM due to the following two factors:

(1) Larger charge density,  $\bar{\rho}_e$ . Figure 6.9 reveals that PBM predicts a large difference in the cations concentration  $n^+$  and anions concentration  $n^-$ . Using equation (3-3) with large differences in  $(n^+ - n^-)$  will lead to larger  $\bar{\rho}_e$  and  $F_{EDL}$ , hence larger value of  $C_f$ .

(2) Larger electrical field strength,  $\bar{E}_z$ . As shown in equation (3-27),  $\bar{E}_z$  is affected by

the difference of both the cations concentration gradient,  $\frac{\partial n^+}{\partial z}$  and anions

concentration gradient  $\frac{\partial n^-}{\partial z}$ . In Figure 6.9, it is shown that both  $\frac{\partial n^+}{\partial z}$  and  $\frac{\partial n^-}{\partial z}$  are

equal to zero as computed with PBM. However in the prediction of NPM,  $\frac{\partial n^+}{\partial z}$  is

positive and  $\frac{\partial n^-}{\partial z}$  is negative (Figure 6.9), hence  $\left( \frac{\partial n^+}{\partial z} - \frac{\partial n^-}{\partial z} \right)$  is a positive term.

Therefore the term  $\int \left[ \rho_e w - \left( e D_f \frac{\partial n^+}{\partial z} - e D_f \frac{\partial n^-}{\partial z} \right) \right] d\bar{A}$  predicted using NPM is smaller

than that computed with PBM. Thus, NPM predicts a lower  $\bar{E}_z$  and as a result, a lower value of  $C_f$  (Figure 6.10). In brief, PBM predicts a higher friction coefficient value as compared to NPM. Larger friction coefficient implies higher wall shear stress.

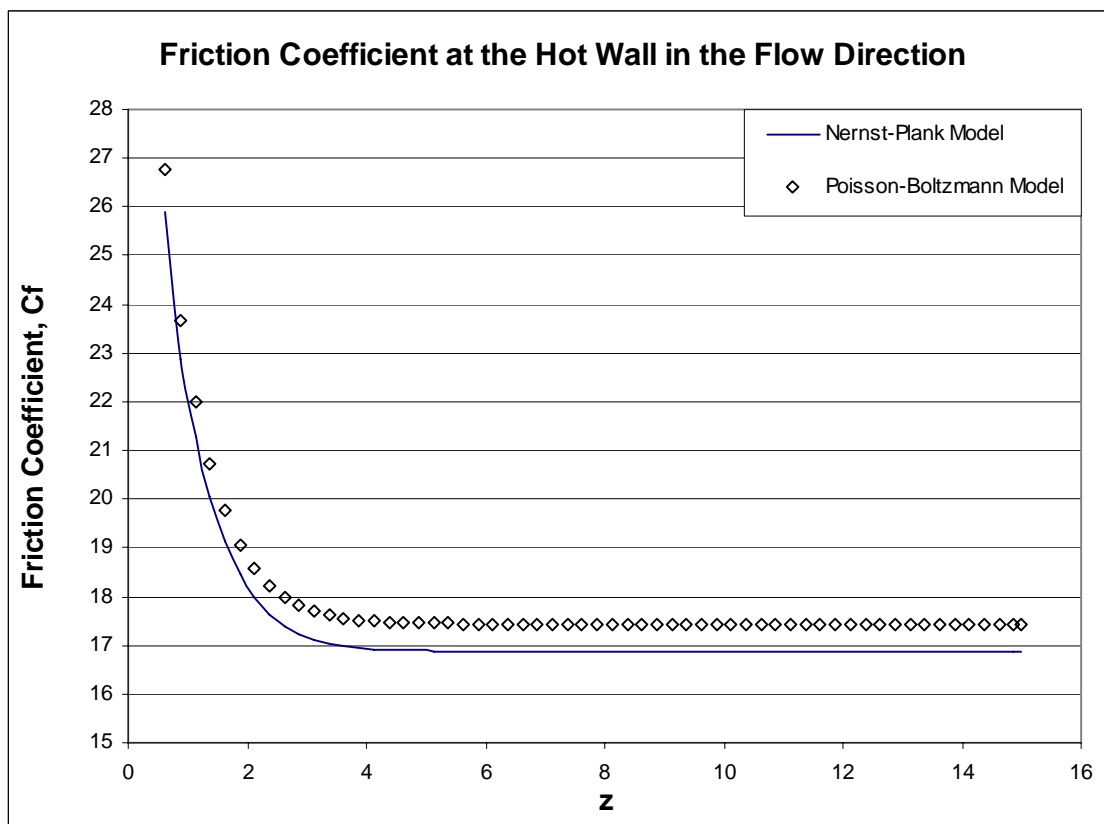


Figure 6.10 The  $C_f$  distribution at microchannel wall along the flow direction

Table 6.4 Comparing of the results predicted by PBM and NPM

Predicted Parameters	PBM	NPM	% Different
Dimensionless velocity $w$ at center of microchannel in fully developed region	1.9899	1.9939	0.20%

Friction coefficient $C_f$ at hot wall at fully developed region	17.4252	16.8559	-3.38%
Dimensionless temperature $\theta$ at hot wall at fully developed region	0.0218	0.0214	-1.97%
Local Nusselt $Nu_x$ at hot wall at fully developed region	3.6178	3.7298	3.00%
Average Nusselt $Nu_{ave}$ of the microchannel	4.4032	4.5600	3.44 %

### 6.2.3 Velocity distribution in the main stream direction

The flow fields of microchannel predicted using the PBM and NPM are compared, prediction with no EDL effect is also included as base-reference. Dimensionless velocity of fluid at the center of microchannel is used to investigate the characteristic of the flow field of the microchannel in the main stream region (a region where percentage change, in direction normal to the wall, of the dimensionless velocity less than 1%). As shown in Figure 6.11, the dimensionless velocities of fluid at the center of microchannel predicted by the PBM and NPM are very similar. For example, the dimensionless velocities at the center of microchannel velocity in the fully developed region predicted by PBM and NPM are 1.9899 and 1.9939 respectively (as shown in Table 6.4). The difference is only 0.20%. This is consistent with the previous research which stated that EDL effect is mainly affecting the flow field in the near wall region but not in the main stream [Mala et al (1997)]. The differences between velocity distributions by two models however are not significant as expected.

As the velocity of fluid at microchannel wall is zero, friction coefficient ( $fRe$ ) is used for comparing the difference of the flow field in the near wall region predicted using different models. To sum up, differences between the two predictions are significant only at the near wall region. At the mainstream region (center of microchannel), the discrepancy is negligible.

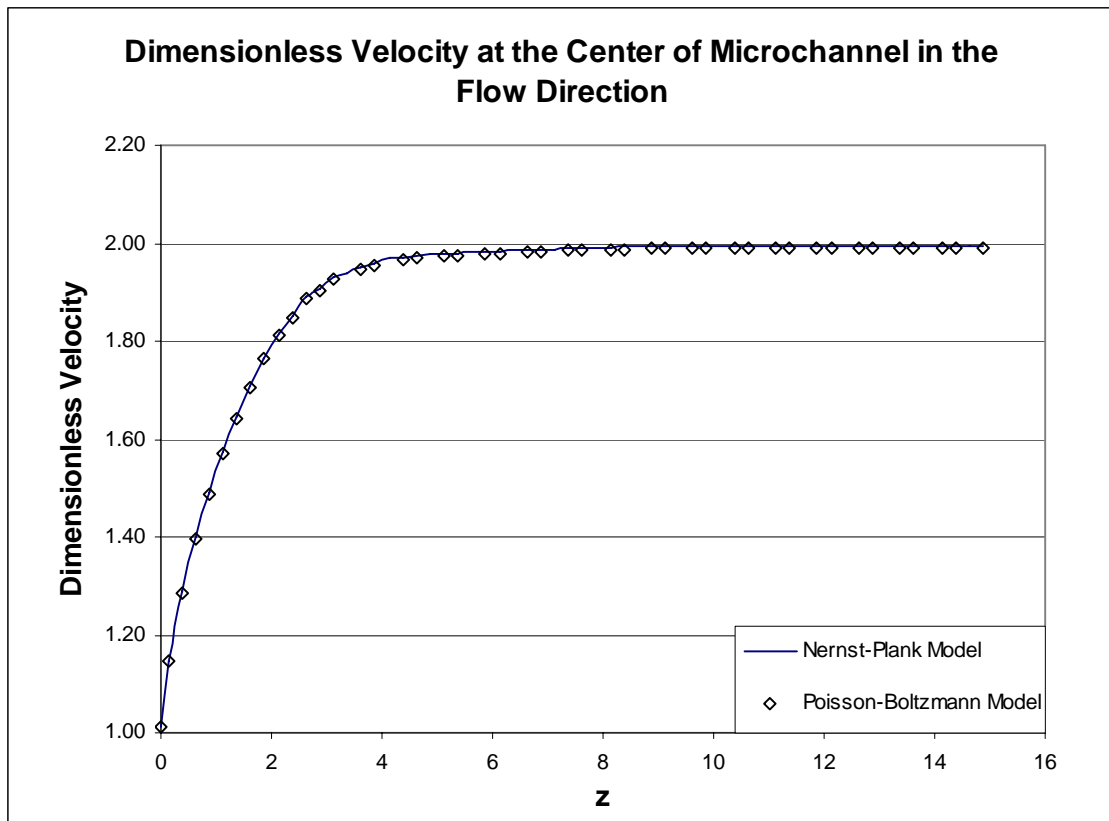


Figure 6.11 Dimensionless velocity distributions at the center of microchannel in the flow direction

#### 6.2.4 Temperature field

$C_f$  values indicate the amount of work done convertible to heat energy, hence affecting the temperature at the near wall flow field. The discrepancy in  $C_f$  predicted by PBM and NPM mentioned in section 6.2.2 will therefore cause discrepancy in the predicted dimensionless temperature at the hot wall. As shown in Figure 6.12, the dimensionless temperature along the hot wall computed using NPM is lower than that predicted using PBM. As a reference, at thermal fully developed region, the dimensionless temperature at the hot wall calculated using NPM is 1.97% lower than that computed using PBM model. The higher fluid temperature along the hot wall would reduce the heat transfer from the hot wall to the fluid and thus affecting the effectiveness of the microchannel.

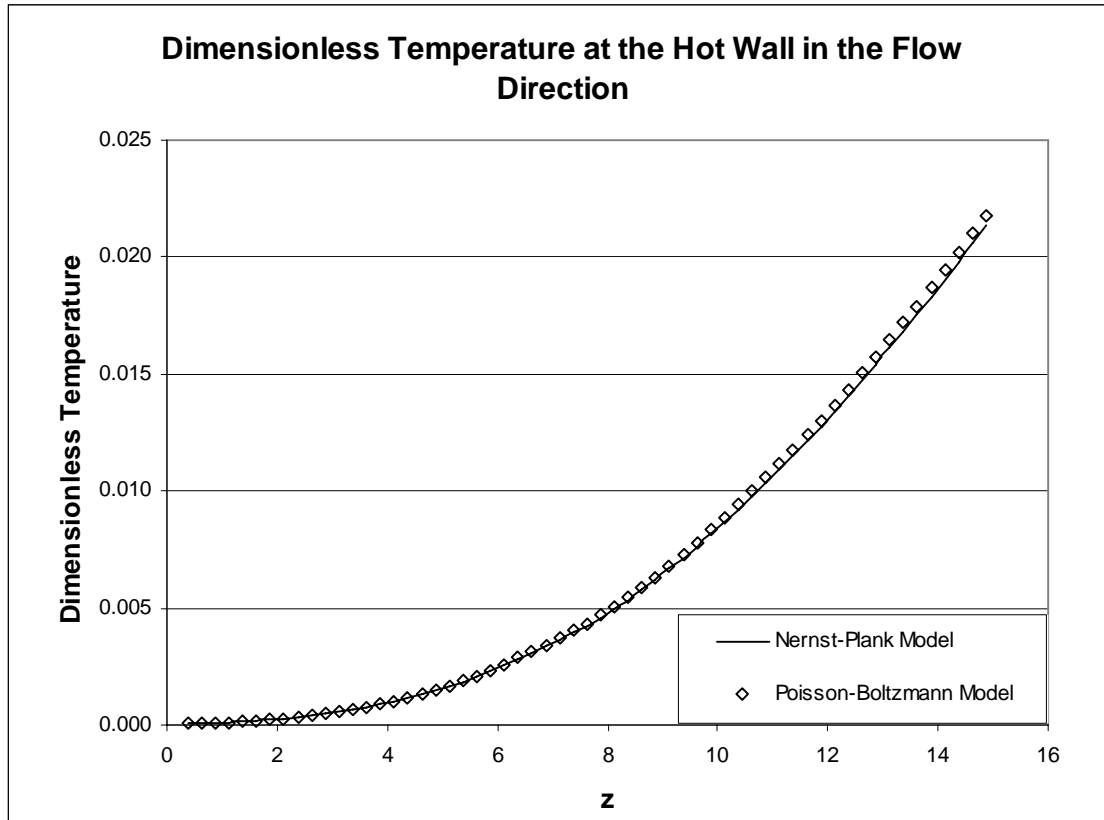


Figure 6.12 Dimensionless temperature distributions on hot wall along the flow direction

### 6.2.5 Nusselt number distribution

Nusselt number is an essential parameter to evaluate the performance of heat transfer device. A local Nusselt number is expressed as

$$Nu_x = \frac{hD_h}{k_f} \quad (6-3)$$

where  $h$  is heat coefficient and  $k_f$  is the thermal conductivity of the fluid.

The average Nusselt number of the microchannel is defined as

$$Nu_{ave} = \frac{1}{L} \int_0^L Nu_x dZ \quad (6-4)$$

Figure 6.13 presents the local Nusselt number distribution at the hot wall along the flow direction; the PBM predicts the lowest values of local Nusselt number. The averaged Nusselt number of the microchannel computed by PBM and NPM is 4.4032

and 4.5600 respectively. From theoretical viewpoint, NPM is considered as the most accurate model, therefore PBM under-predicts the performance of the microchannel by 3.44%.

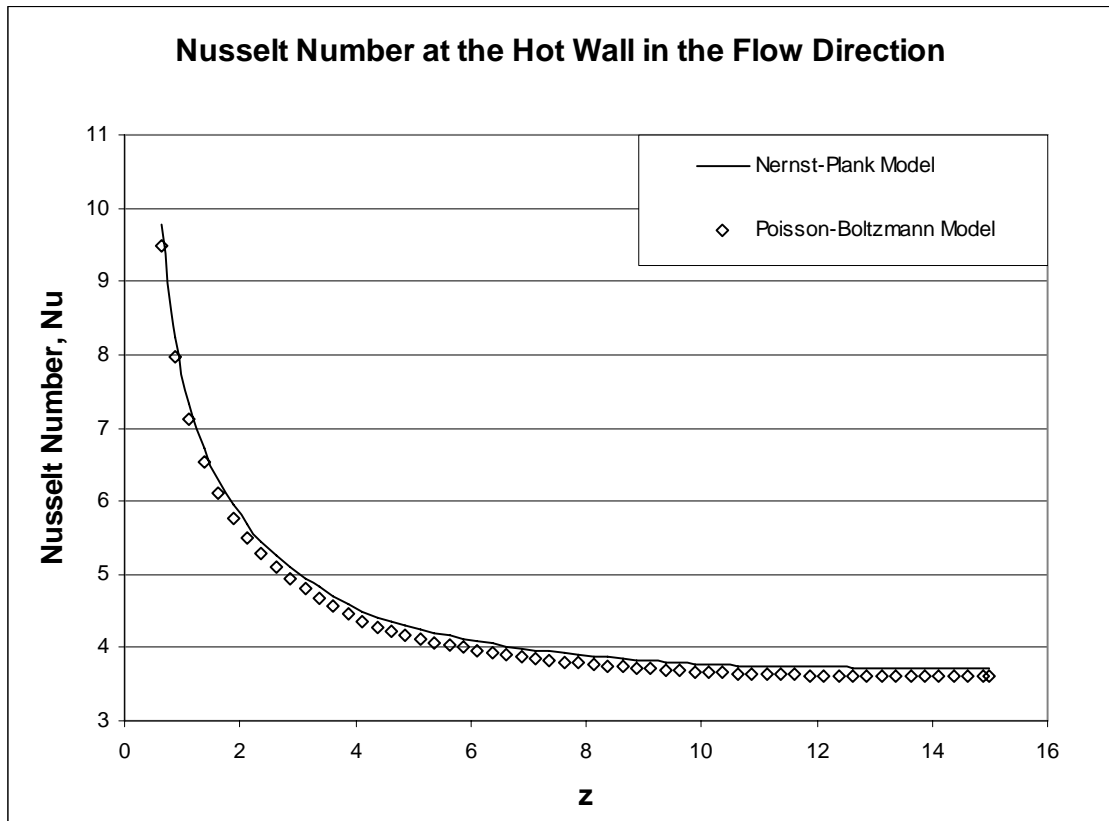


Figure 6.13 Local Nusselt number distributions on hot wall along the flow direction

### 6.2.6 The effect of $K$ number on the discrepancy of prediction by NPM and PBM

The dimensionless velocity of the fluid at the center of a microchannel, for  $K$  value of 20 is included in Figure 6.14 for analysis purpose.  $K$  number is the product of Debye-Huckel parameter,  $\kappa$  and hydraulic length  $D_h$  (equation 3-4).  $1/\kappa$  is the thickness of EDL while  $D_h$  is the hydraulic diameter of the micrometer.  $D_h$  is the parameter which shows the channel is in microscale.  $K$  is a ratio of the characteristic length of microchannel over the EDL thickness. A smaller  $K$  value of 20 means thicker EDL.

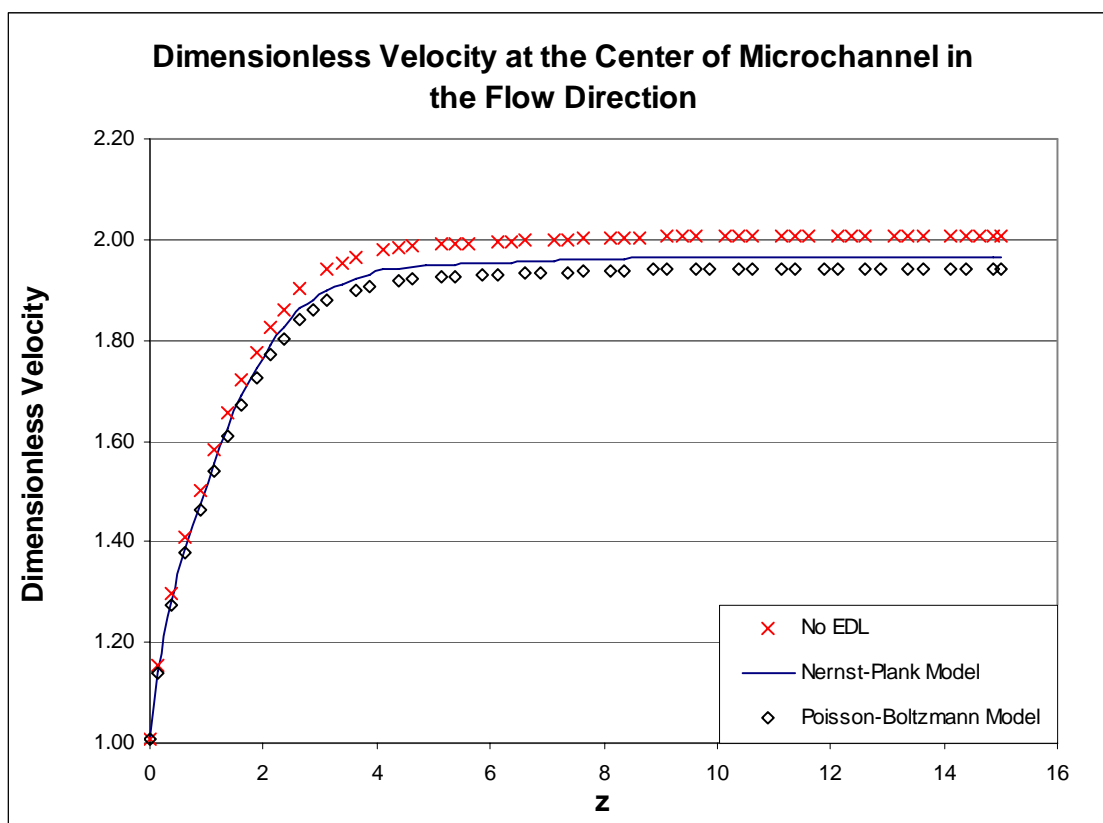


Figure 6.14 Dimensionless velocity at the center of microchannel in the flow direction, for  $K=20$

Stronger EDL effect is therefore expected as shown in the larger discrepancy of prediction by PBM and NPM when comparing to the prediction without EDL effect (3.26 % and 2.08%, see Table 6.6). However the discrepancy is rather small. Even in



the case for  $K$  of 20, the discrepancy between PBM and NPM (1.20%, see Table 6.7) is small, as mentioned in section 6.2.3 the EDL effect mainly affects the flow field in the near wall region but not the mainstream flow.

Table 6.5 Comparison of the result predicted by PBM, NPM and without EDL effect, for  $K=20$

Prediction Item	PBM	NPM	No EDL
Dimensionless velocity $w$ at center of microchannel in fully developed region	1.9404	1.9641	2.0059
Friction coefficient $C_f$ at hot wall at fully developed region	18.7540	17.8793	15.5074
Dimensionless temperature $\theta$ at hot wall at fully developed region	0.0234	0.0224	0.0203
Local Nusselt number $Nu_x$ at hot wall at fully developed region	2.8313	2.9696	4.1367
Average Nusselt number $Nu_{ave}$ of the microchannel	3.4550	3.5890	5.1970

Table 6.6 Comparison of the percentage difference between result predicted by PBM, NPM with result predicted without EDL effect, for  $K=20$

Prediction Item	PBM	NPM
Dimensionless velocity $w$ at center of microchannel in fully developed region	-3.26%	-2.08%
Friction coefficient $C_f$ at hot wall at fully developed region	20.94%	15.30%
Dimensionless temperature $\theta$ at hot wall at fully developed region	15.42%	10.53%
Local Nusselt number $Nu_x$ at hot wall at fully developed region	-31.56%	-28.21%
Average Nusselt number $Nu_{ave}$ of the microchannel	-33.52%	-30.94%

Table 6.7 Comparison of the percentage difference between result predicted by PBM with NPM with, for  $K=20$

Prediction Item	Compare PBM with NPM
Dimensionless velocity $w$ at Center of Microchannel in fully developed region	-1.20%
Friction Coefficient $C_f$ at hot wall at fully developed region	4.89%
Dimensionless temperature $\theta$ at hot wall at fully developed region	4.43%
Local Nusselt number $Nu_x$ at hot wall at fully developed region	-4.66%
Average Nusselt number $Nu_{ave}$ of the microchannel	-3.73

Figure 6.15 and figure 6.16 suggest that the differences of the friction coefficient and dimensionless temperature in the  $z$ -direction in the fully developed region as predicted by NPM and PBM at  $\kappa$  equal to 20 are 4.89% and 4.66% respectively, which are within the acceptable range of engineering tolerance (say 5%).

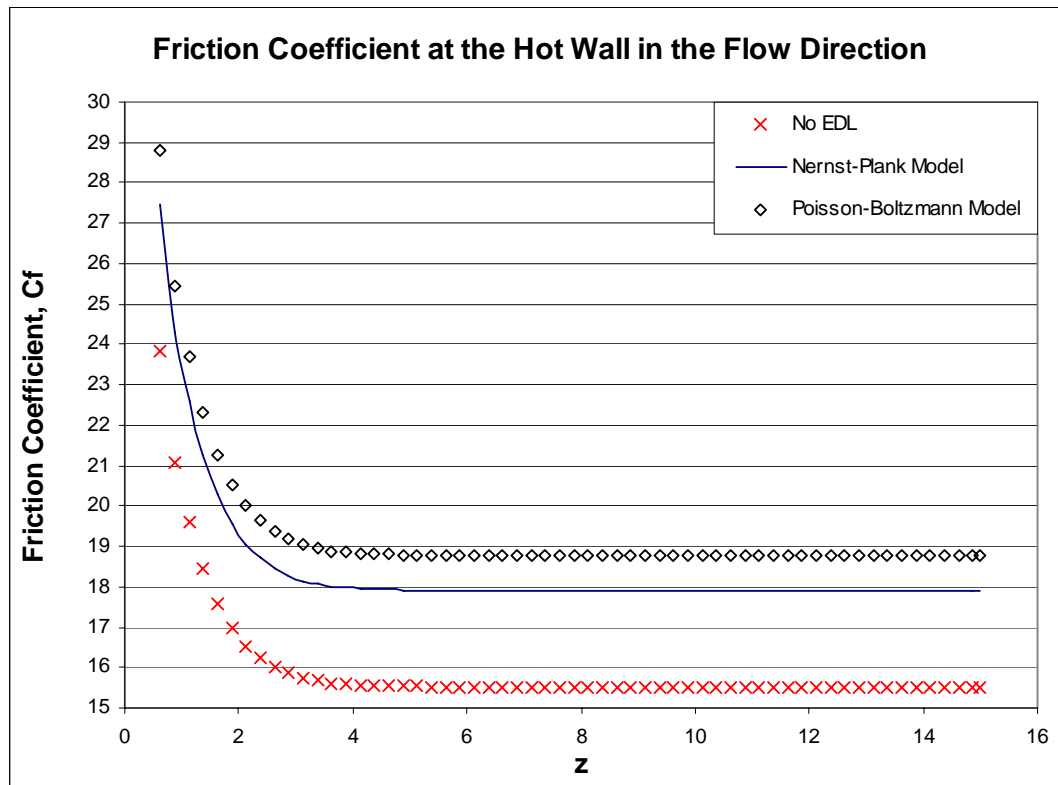


Figure 6.15 The  $C_f$  distribution at microchannel wall along the flow direction, for  $K=20$

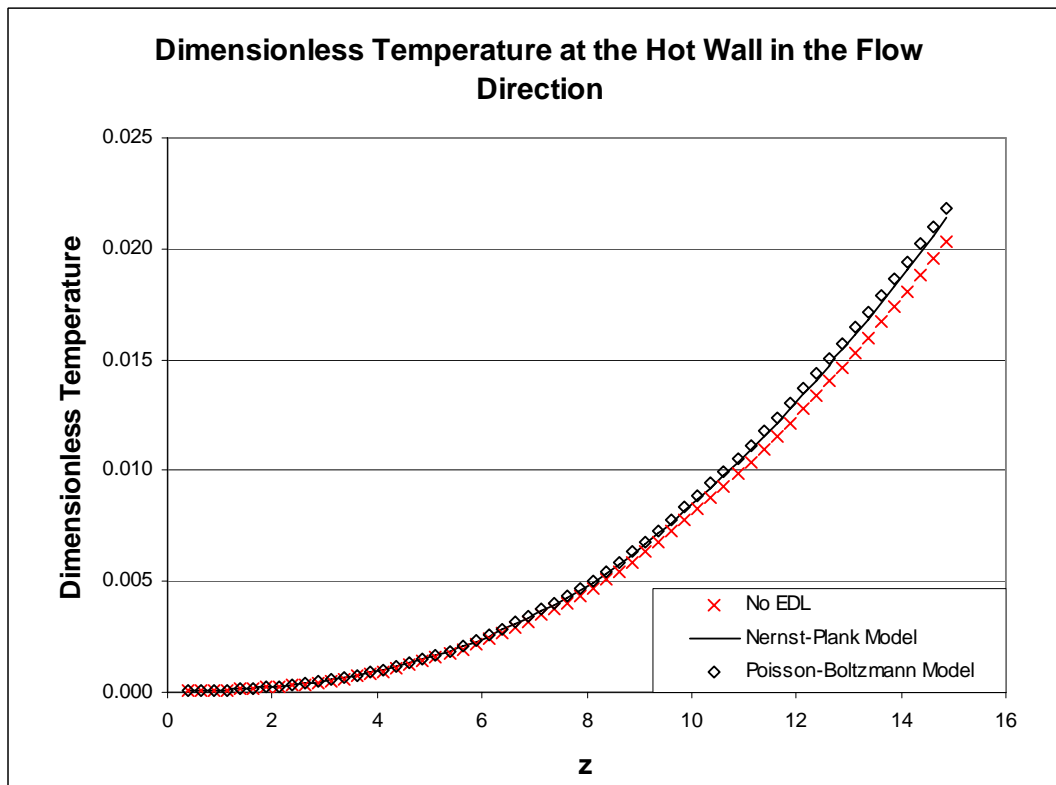


Figure 6.16 Dimensionless temperature distribution on hot wall along the flow direction, for  $K=20$

Figure 6.17 and Table 6.5 further show that the discrepancy between the predictions by PBM and NPM for the averaged Nusselt number with  $\kappa$  of 20 is 3.73%, and is also within engineering tolerance. Therefore even in the case of high EDL thickness, the discrepancy of prediction of the performance of PBM and NPM is still within 5%.

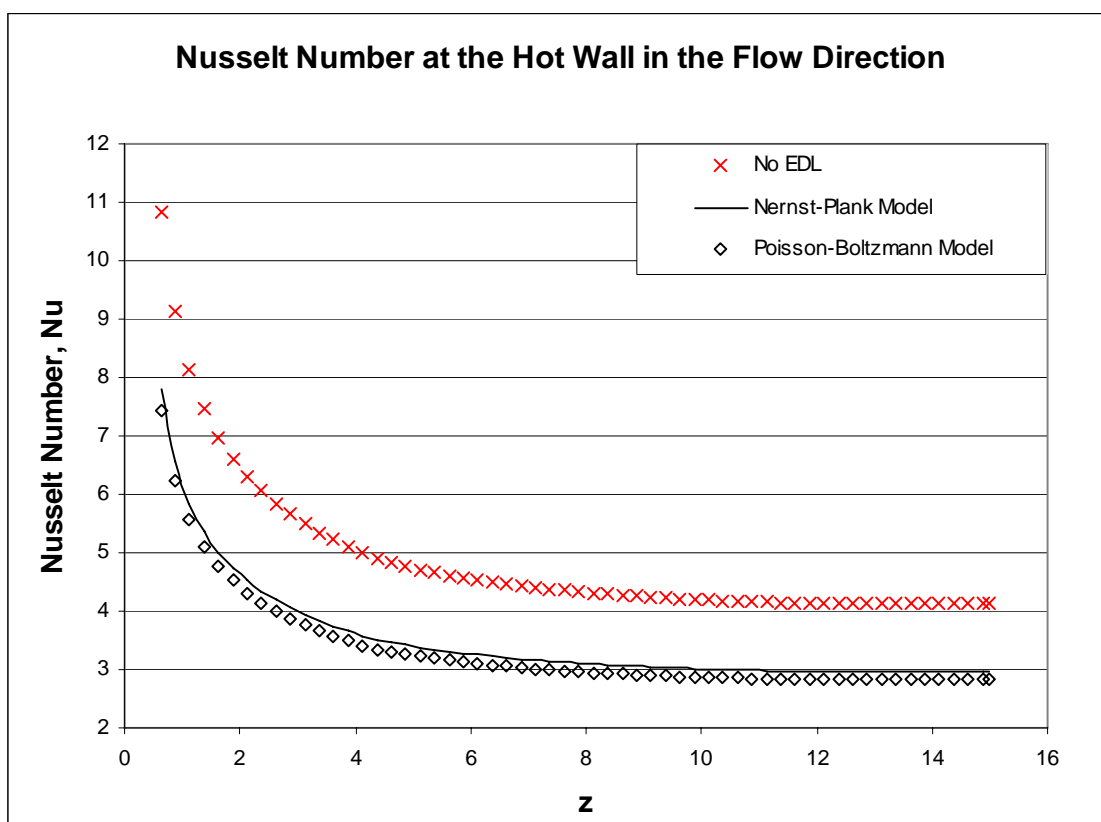


Figure 6.17 Distribution of local Nusselt number on hot wall along the flow direction, for  $K=20$

### 6.3 Effect of Aspect Ratio

When comparing to 2-D model, a 3-D model is far more challenging to handle and more CPU time is needed. However, for complex shapes and in cases where aspect ratio, AR is not close to zero, a 3-D model is unavoidable. Shah and London (1978)

reported the different  $fRe$  values at different AR values for fully developed region. For developing region, this study can only be done by using a 3-D model. In this section, a total of 5 aspect ratio values, 0.30, 0.50, 0.67, 0.75 and 1.00 were chosen to study the effect of aspect ratio for microchannels.

Figure 6.18 shows the  $fRe$  value distribution along  $z$ -direction (flow direction) for different AR values. The trend of the  $fRe$  value is similar. However, the values of  $fRe$  increase with decreasing of aspect ratios.

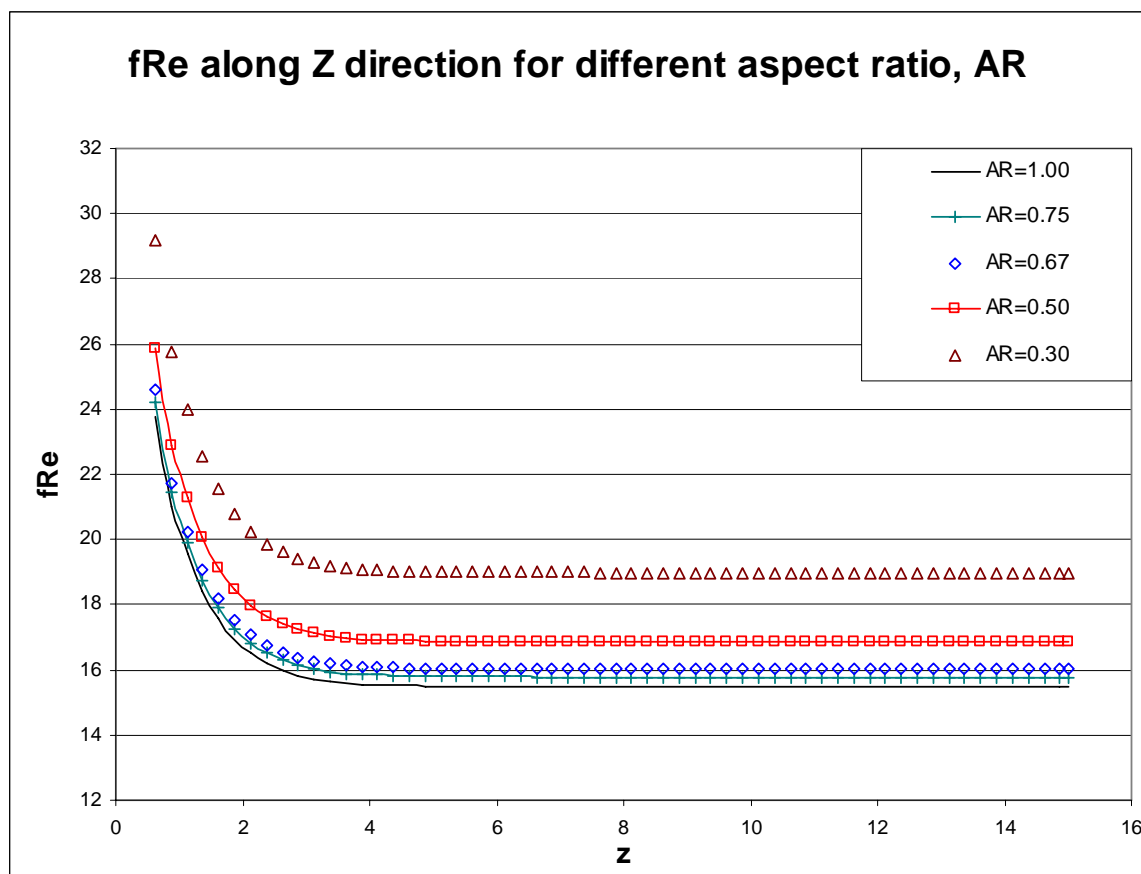


Figure 6.18 Friction Coefficient,  $fRe$  distribution along  $z$ -direction for different aspect ratios,  $AR$

Figure 6.19 summarizes the  $fRe$  value in the fully developed region for flow field with and without the EDL effect [Shah and Landon (1978)]. As mentioned in

section 6.1, the EDL body force is an opposing force; therefore it is found in Figure 6.19 that the  $fRe$  values for flow field with EDL are generally higher than that without EDL effect. The percentage differences between  $fRe$  values predicted with and without EDL effect at different aspect ratio are summarized in Table 6.8.

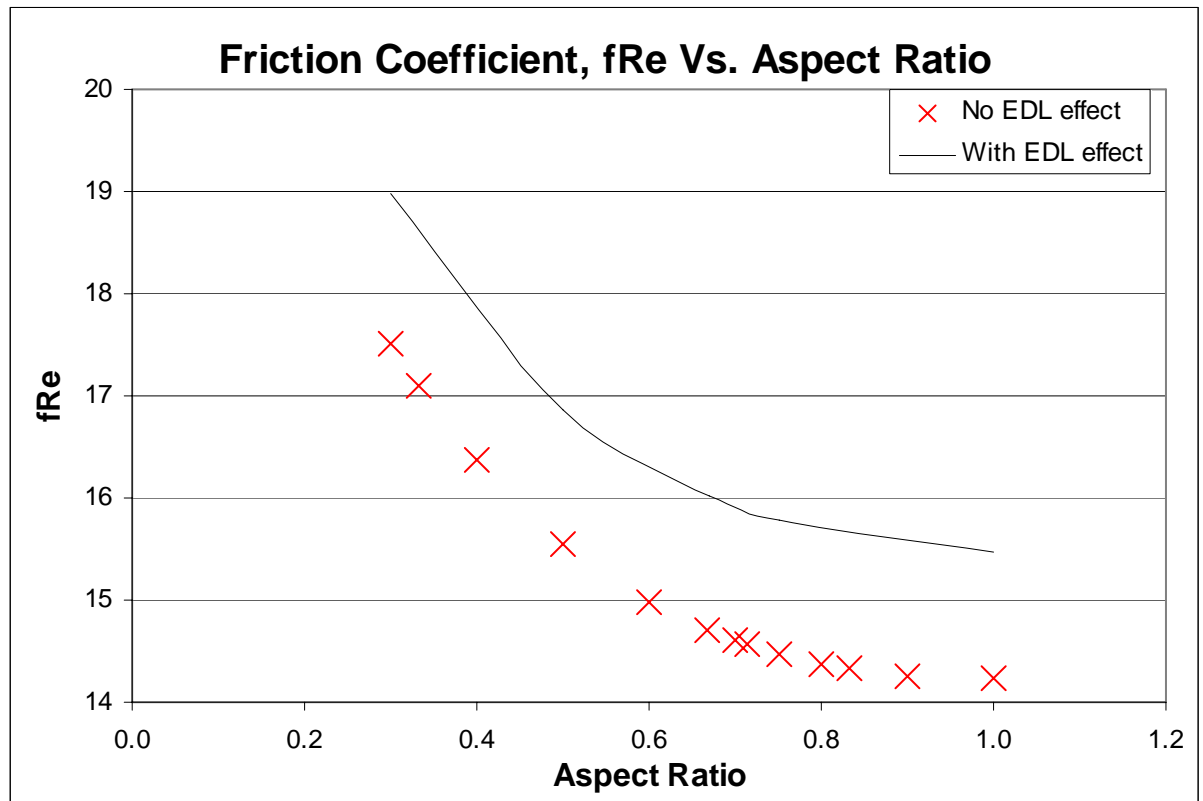


Figure 6.19 Friction coefficient,  $fRe$ , in the fully developed region for different aspect ratios,  $AR$

Table 6.8 Comparison of the percentage differences between  $fRe$  predicted with and without EDL effect at different aspect ratio

$fRe$ value	AR = 0.3	AR = 0.5	AR = 1.0
with EDL Effect	18.99	16.86	15.48
without EDL Effect	17.51	15.51	14.23
Percentage different	8.45%	8.70%	8.78%

As for developing flow, the entrance length is one of important parameter, Figure 6.20 shows the entrance length at different aspect ratio for both with and without EDL effects. The entrance length,  $L_e$ , for prediction without EDL effect is based on the transitional empirical formula [Schlichting (1979)].

$$L_e \approx 0.06Re \quad (6-5)$$

and with the definition of Reynolds number,  $Re$ , equation 6-5 can be written as

$$L_e \approx 0.06 \frac{\rho_f w D_h}{\mu_f} \quad (6-6)$$

As shown in Figure 6.20, with the higher effective viscous force due to the EDL effect, the flow field predicted with EDL effect is fully developed with a smaller entrance length.

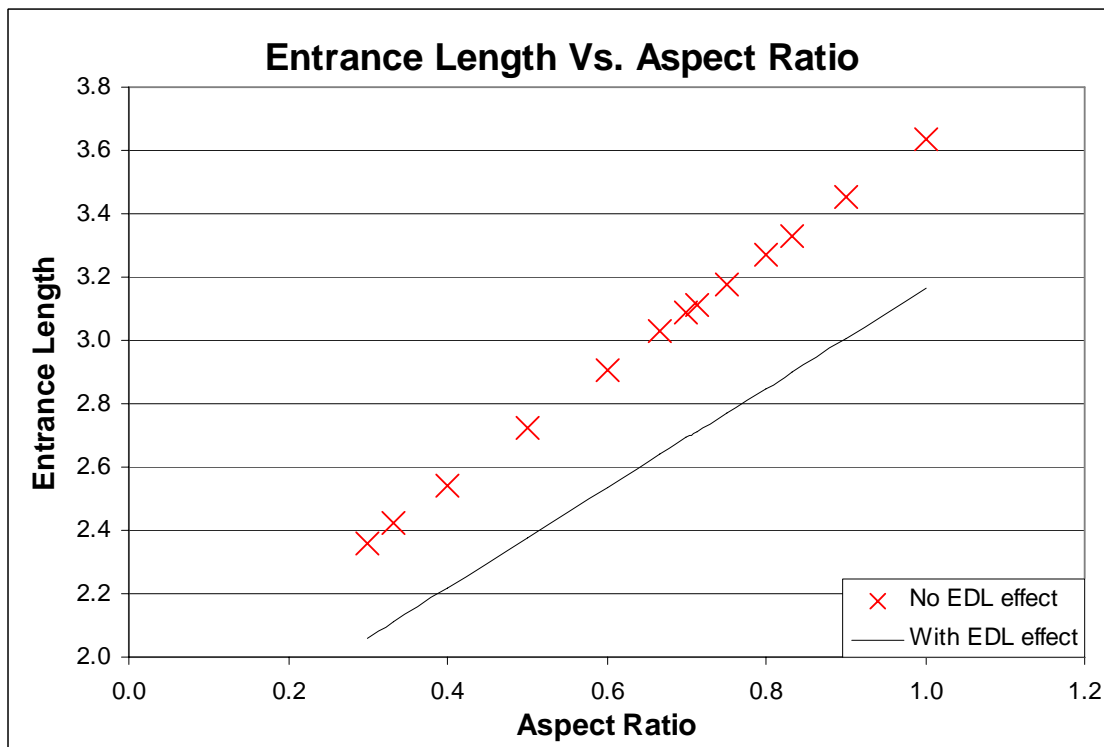


Figure 6.20 Entrance length for different aspect ratios,  $AR$

Similar to the  $fRe$  values, the distribution along  $z$ -direction at different aspect ratios have similar trend from the viewpoint of thermal aspect. In the inlet region, the gradient in decreasing in  $Nu$  value is very steep (as shown in Figure 6.21). The  $Nu$  for a given  $AR$  approaches its asymptotic value in the fully developed region for  $z$  greater than about 8.

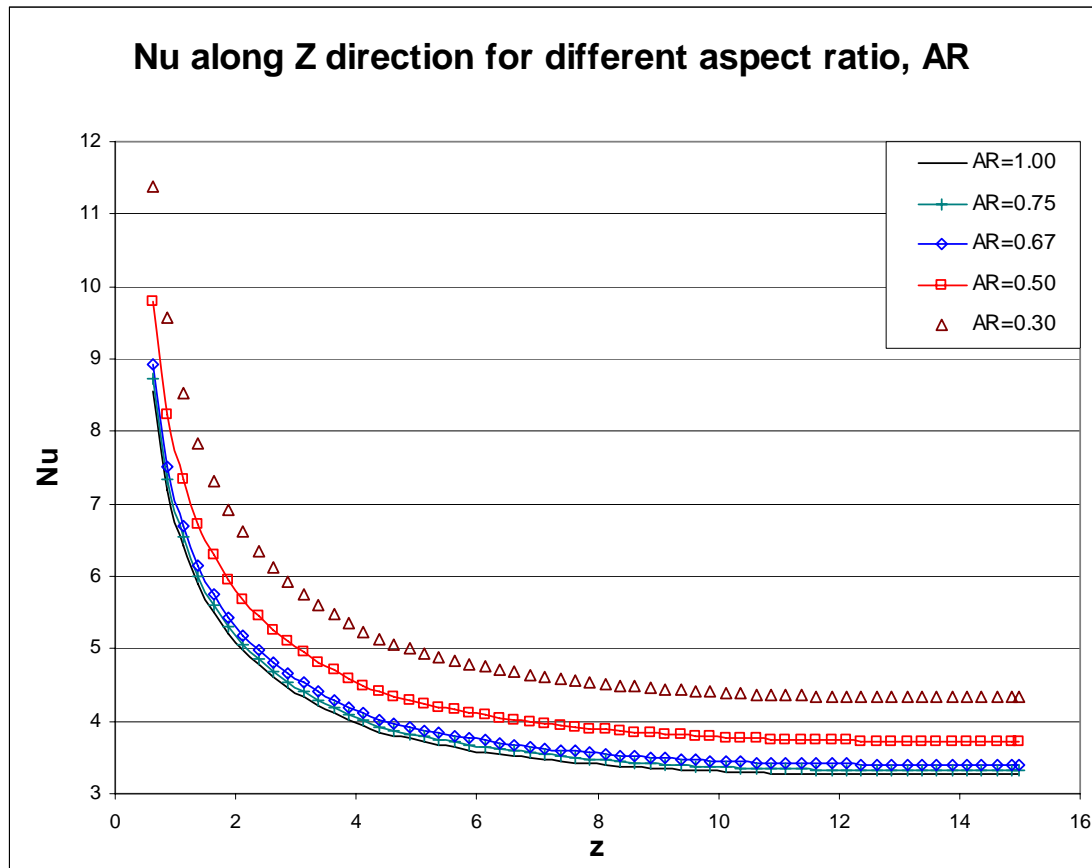


Figure 6.21 Nusselt Number,  $Nu$  distribution along  $z$ -direction for different aspect ratios,  $AR$

Figure 6.22 summarizes the  $Nu$  value in the the fully developed region for different aspect ratios. It is found that the smaller aspect ratio would result in higher  $Nu$  values. With the higher opposing force, extra heat is produced and hence reduces the efficiency of heat transfer. Therefore, the  $Nu$  values with EDL effect are lower

than that without EDL effect. The percentage differences between  $Nu$  values predicted with and without EDL effect at different aspect ratio are summarized in Table 6.9.

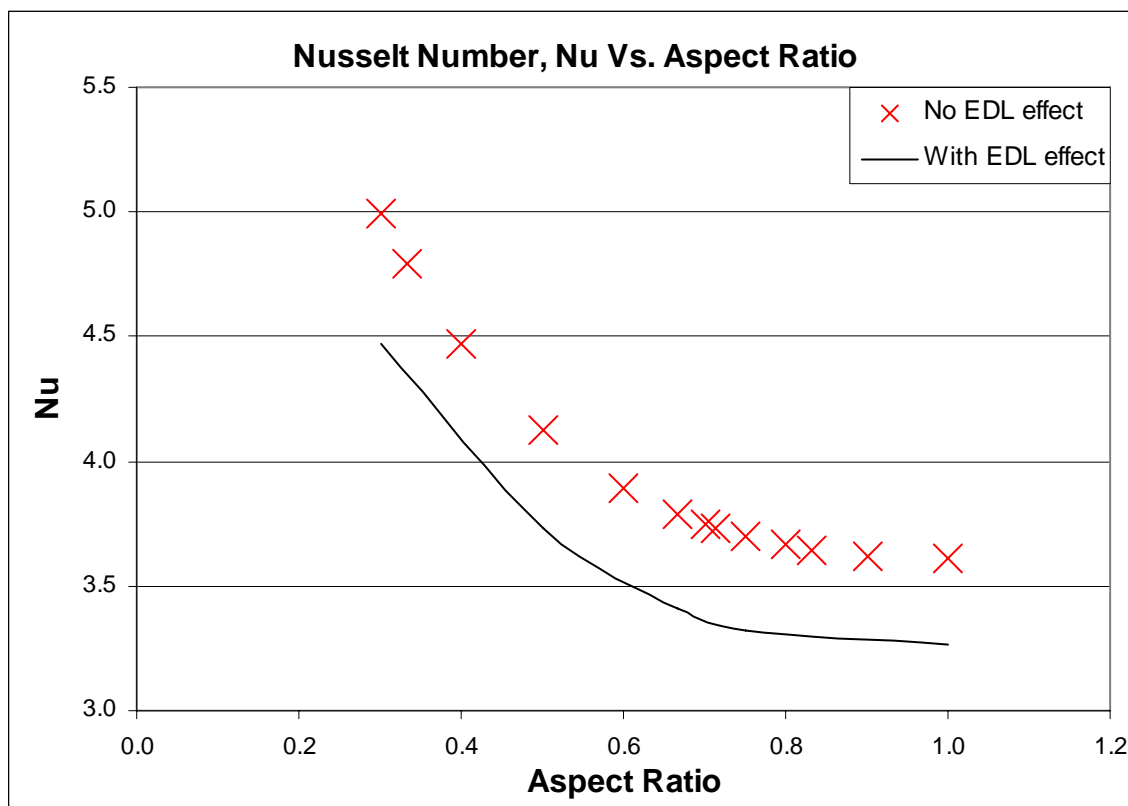


Figure 6.22 Nusselt number,  $Nu$  in the fully developed region for different aspect ratios,  $AR$

Table 6.9 Comparison of the percentage differences between  $Nu$  predicted with and without EDL effect at different aspect ratio

$Nu$ value	$AR = 0.3$	$AR = 0.5$	$AR = 1.0$
with EDL Effect	4.474	3.730	3.264
without EDL Effect	4.990	4.137	3.608
Percentage different	-10.34%	-9.84%	-9.53%

In all, the discrepancy of  $fRe$  and  $Nu$  values for different  $AR$ s are significant. As shown in Table 6.8 and 6.9, in case of the aspect ratio equal to 0.3 and 1.0 the



discrepancy of  $fRe$  and  $Nu$  can be up to 23% (18.99 for  $AR=0.3$  and 15.48 for  $AR=1.0$ ) and 37% (4.474 for  $AR=0.3$  and 3.264 for  $AR=1.0$ ) respectively for prediction with EDL effect. Therefore a 3-D analysis is concluded to be important and necessary for investigating the EDL effect in microchannel.

#### 6.4 Comparing Results at Different Schmidt Number ( $Sc$ )

Compared to PBM, an extra parameter termed as Schmidt number,

$Sc = \frac{\mu_f}{\rho_f D_f}$ , is found in the NPM (as shown in section 3.2.3).  $Sc$  represents the ratio

of viscosity and diffusivity effects and thus is a function of fluid properties only. For a fixed Reynolds number,  $Re$ , the lower  $Sc$  value, the larger would be the diffusion layer.

As shown, Figure 6.23, the anions concentration gradient,  $\frac{\partial n^-}{\partial z}$  decreases as

the Schmidt number increases, but the cations concentration gradient  $\frac{\partial n^+}{\partial z}$  increases.

As a result, the value of  $\left( \frac{\partial n^+}{\partial z} - \frac{\partial n^-}{\partial z} \right)$  increases and causes the EDL body force to

reduce (as  $\left( \frac{\partial n^+}{\partial z} - \frac{\partial n^-}{\partial z} \right)$  is a positive term), which leads to a lower friction coefficient

as shown in Figure 6.24.

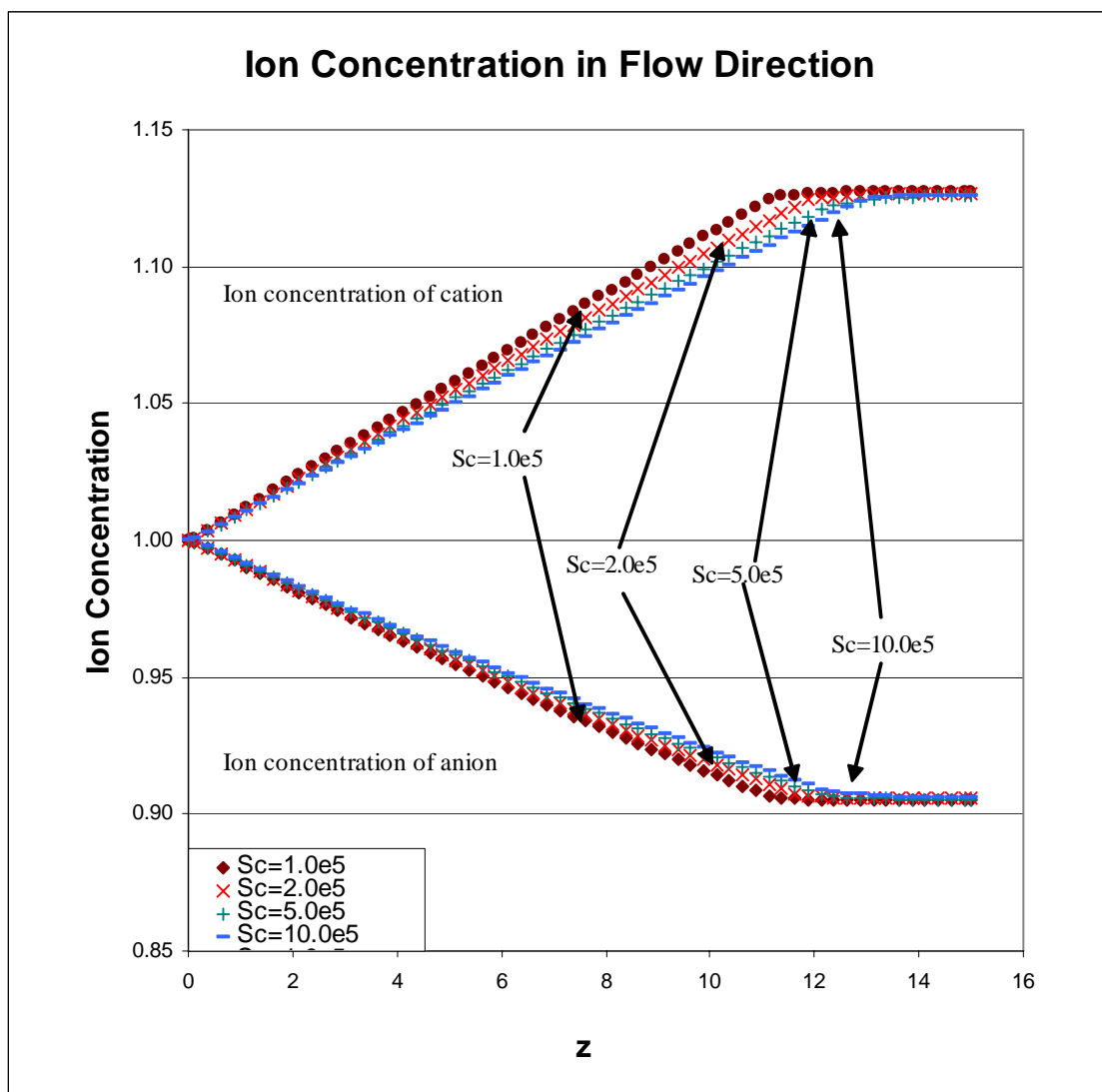


Figure 6.23 Cation and anion concentration distribution along  $z$ -direction at near wall grid

The effect of Schmidt number on friction coefficient however is not significant. Ten times increases in the Schmidt number ( $1.0 \times 10^5$  to  $1.0 \times 10^6$ , see Figure 6.25) only leads to 2% reduction in the friction coefficient (16.86 to 16.48). Note that the use of Schmidt number  $1.0 \times 10^6$  is purely for investigative purpose since fluid with Schmidt number  $1.0 \times 10^6$  may not be realistic.

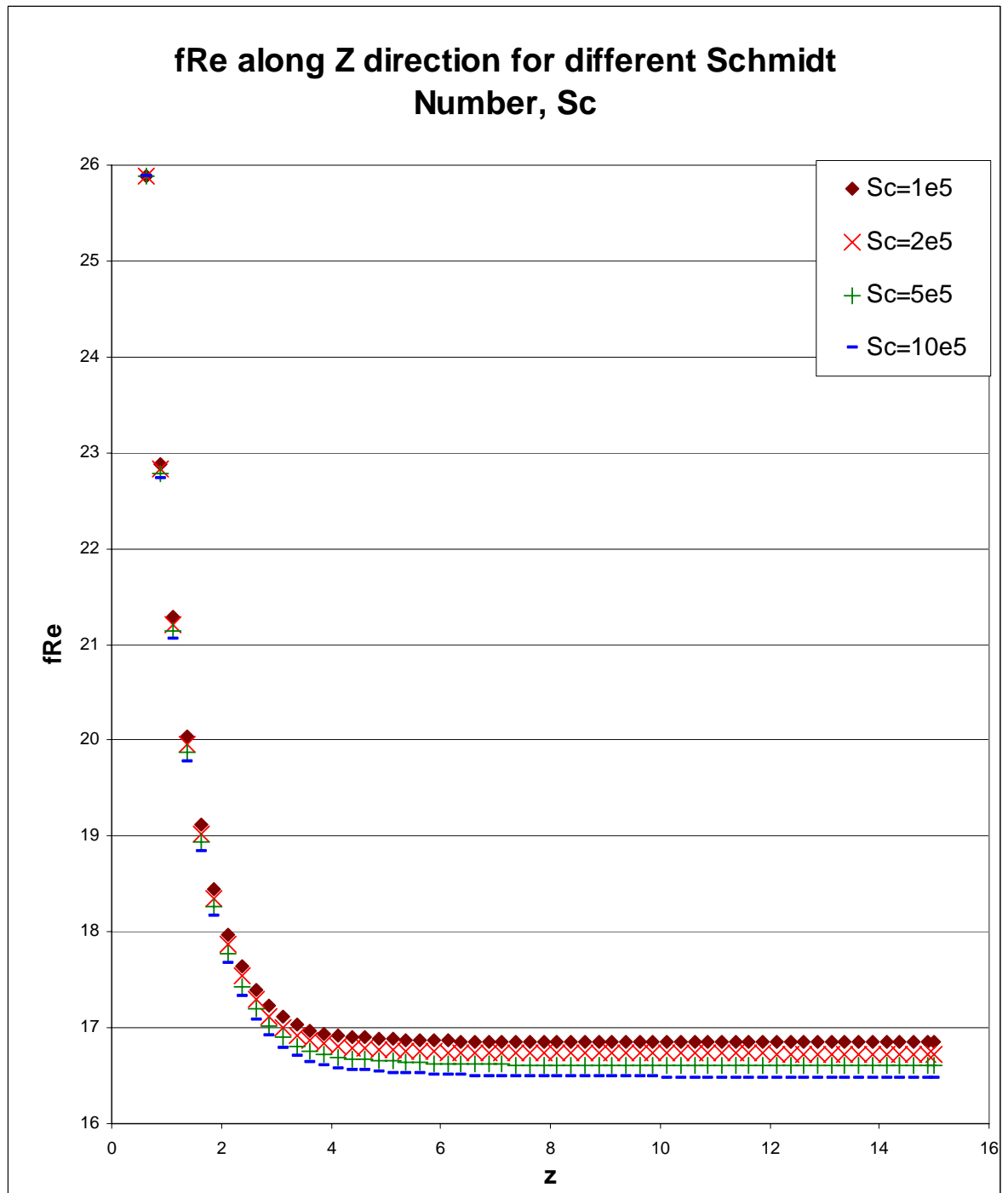


Figure 6.24 Friction coefficients,  $C_f$  distributions for different Schmidt numbers,  $Sc$ , on microchannel wall along the flow direction

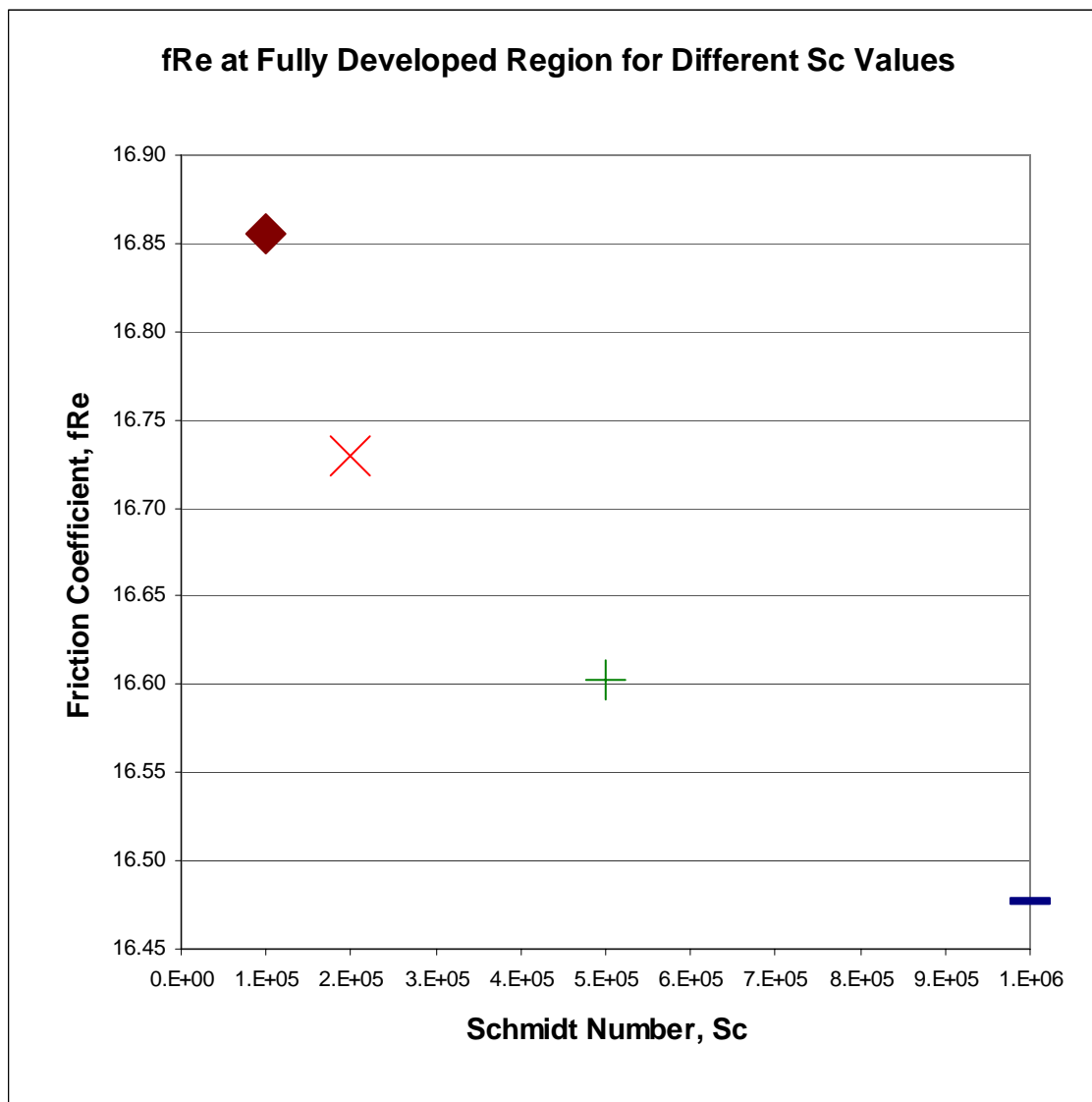


Figure 6.25 Friction coefficients,  $C_f$  in the fully developed region for different Schmidt numbers,  $Sc$ .

## 6.5 Effect of Wall Electrical Potential

In this section, the effect of wall electrical potential  $\bar{\xi}_o$  is studied. A total of five cases of dimensionless electrical potentials,  $\bar{\xi}_o$  namely 1, 2, 3 and 4, are used as examples.

Fig. 6.25 shows the values of dimensionless velocities at the center of the channel grid along the  $z$ -direction (streamwise), for  $\bar{\xi}_o=1, 2, 3$  and 4. The plots are

rather similar, and the flows become fully developed when  $z$  values are around 8.8 to 11.8. The deviation increases when  $\bar{\xi}_o$  is increased. As the applied wall electrical potential increases, the center velocity in the fully developed region increases. This can be explained as follows. As the inlet condition is set as  $z=0$ ,  $w=1$ , the stronger the EDL effects, the higher the walls shear stress hence the near wall velocity is reduced. However as the net flow is fixed, the velocity at the channel centerline will be higher so to compensate the lower velocity at near wall. And with hence increase the velocity gradient which tally with higher wall shear at near wall region.

The nondimensional fully developed velocities at the center of channel for  $\bar{\xi}_o$  at 1 and 4 are 1.987 and 2.11 respectively. It is also observed that the difference in the nondimensional fully developed velocity is not linearly related with the wall electrical potential. Fig. 6.25 further shows an increase in the entrance length with higher values of the wall electrical potential.

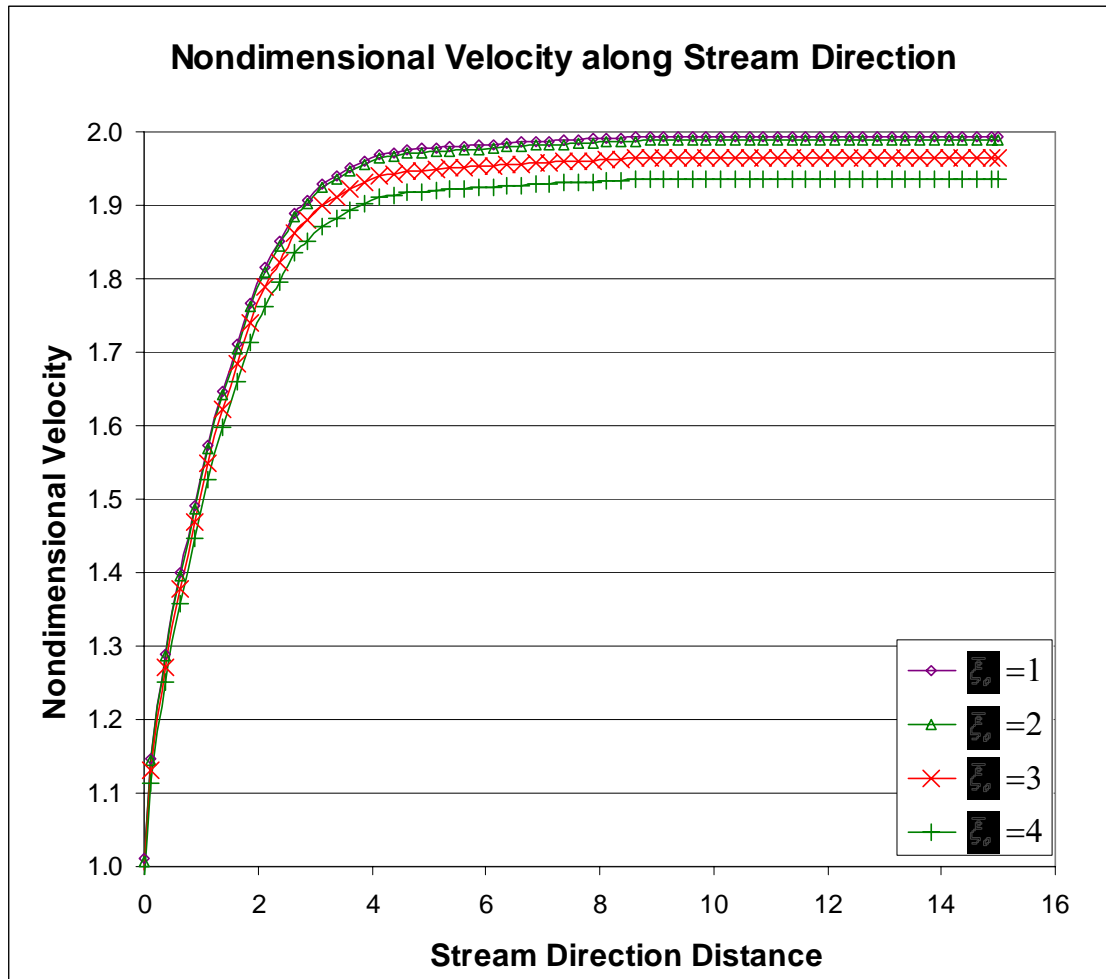


Figure 6.26 Channel-center velocity distributions along the stream flow direction

The relationship between the nondimensional entrance length and wall electrical potential is summarized in Fig. 6.26. Due to the higher ion concentration, the effective viscosity of the flow is stronger hence the flow fully developed faster and hence shorter developing length is needed; the strong EDL effect hence will causes a shorter developing length required.

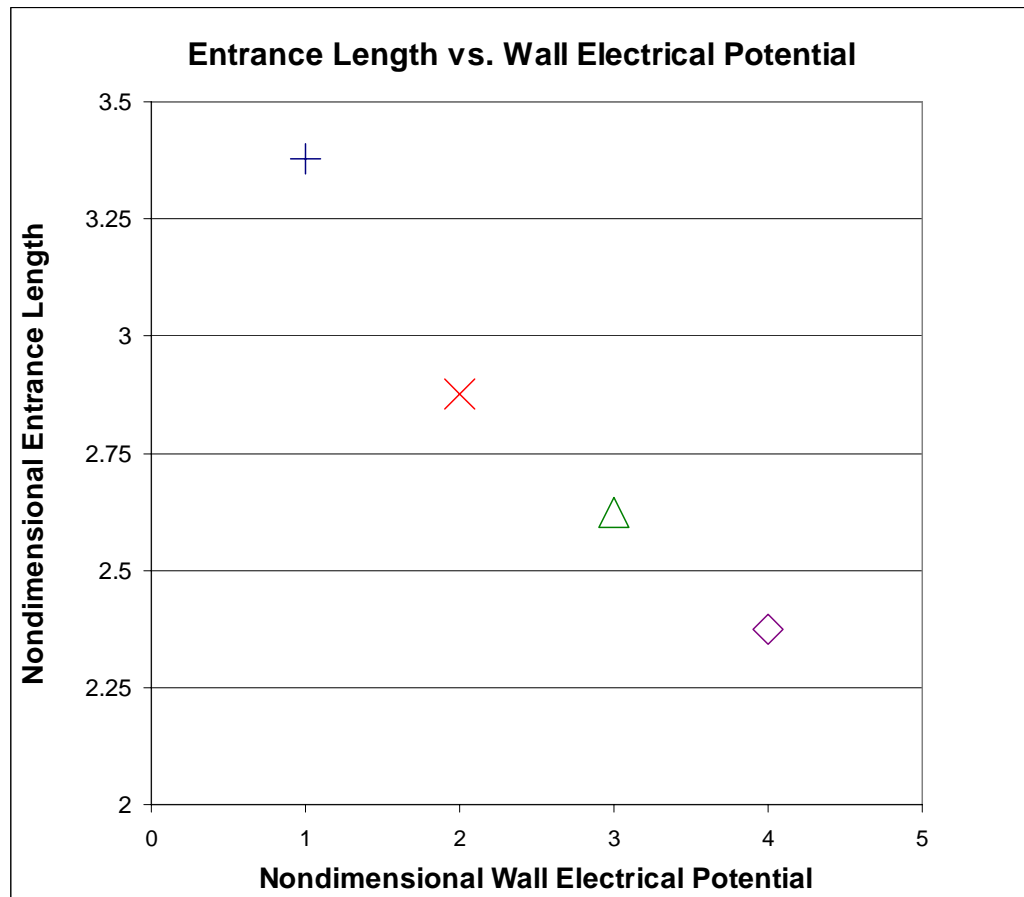


Figure 6.27 Nondimensional entrance length vs. nondimensional wall electrical potential

With higher opposing force for cases of larger wall electrical potential, the energy dissipated in the near wall region is higher. Hence the near wall temperature for higher  $\bar{\xi}_o$ , is higher (Figure 6.28). The higher near wall temperature will eventually reduce the efficiency of heat transfer of the microchannel.

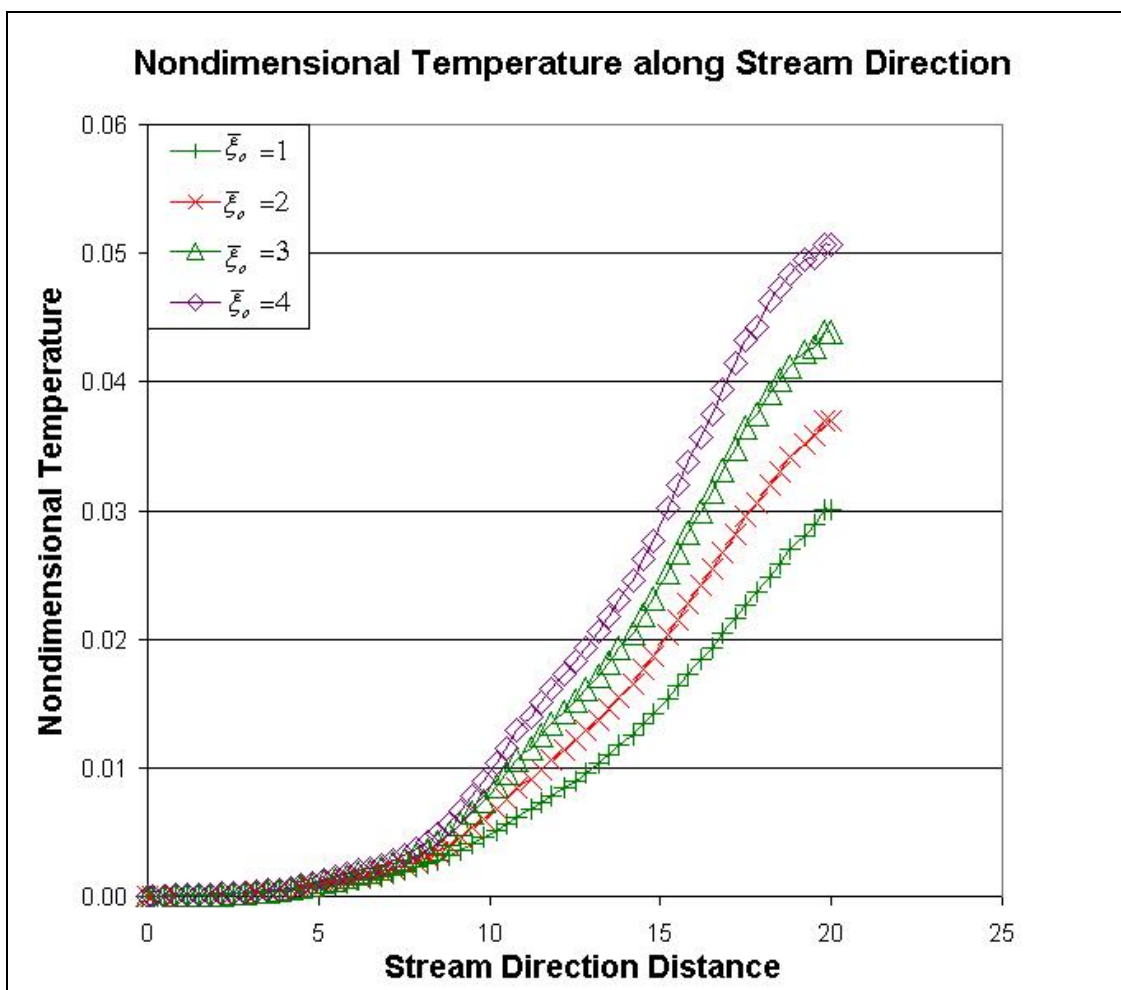


Figure 6.28 Nondimensional hot wall temperature distributions along stream direction

Due to the ineffectiveness of heat transfer for the flow field with EDL effect, Figure 6.29 shows the Nusselt number decreases as the nondimensional wall electrical potential increases. It is also noted that, near the entrance, the Nusselt number for all  $\bar{\xi}_o$  values are almost identical. This shows that the effect of EDL is significant only at further downstream from the entrance. Figure 6.29 suggests that high Nusselt number exists (9 times as compared to the fully developed region) at the entrance of the microchannel which implies that the study of EDL effect on heat transfer effect in the developing region in a 3D microchannel cannot be omitted.



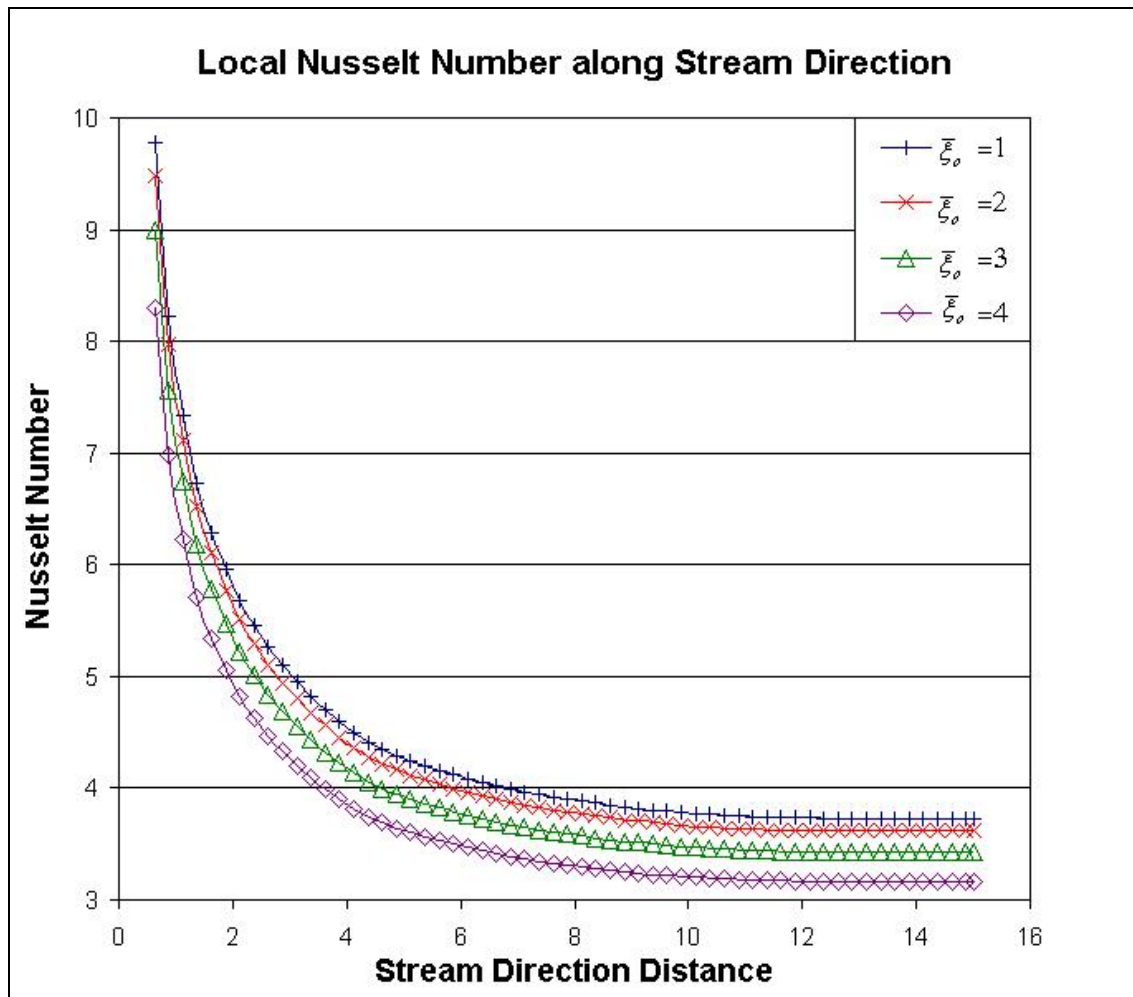


Figure 6.29 Local Nusselt number along z-direction (streamwise)

As shown in Figure 6.30, Nusselt number in the fully developed region with reduces in the wall electrical potential. It shows that the higher wall electrical potential the more significant the EDL effect, thus higher viscous drag force and cause higher heat dissipation and lead to the lower Nusselt number.

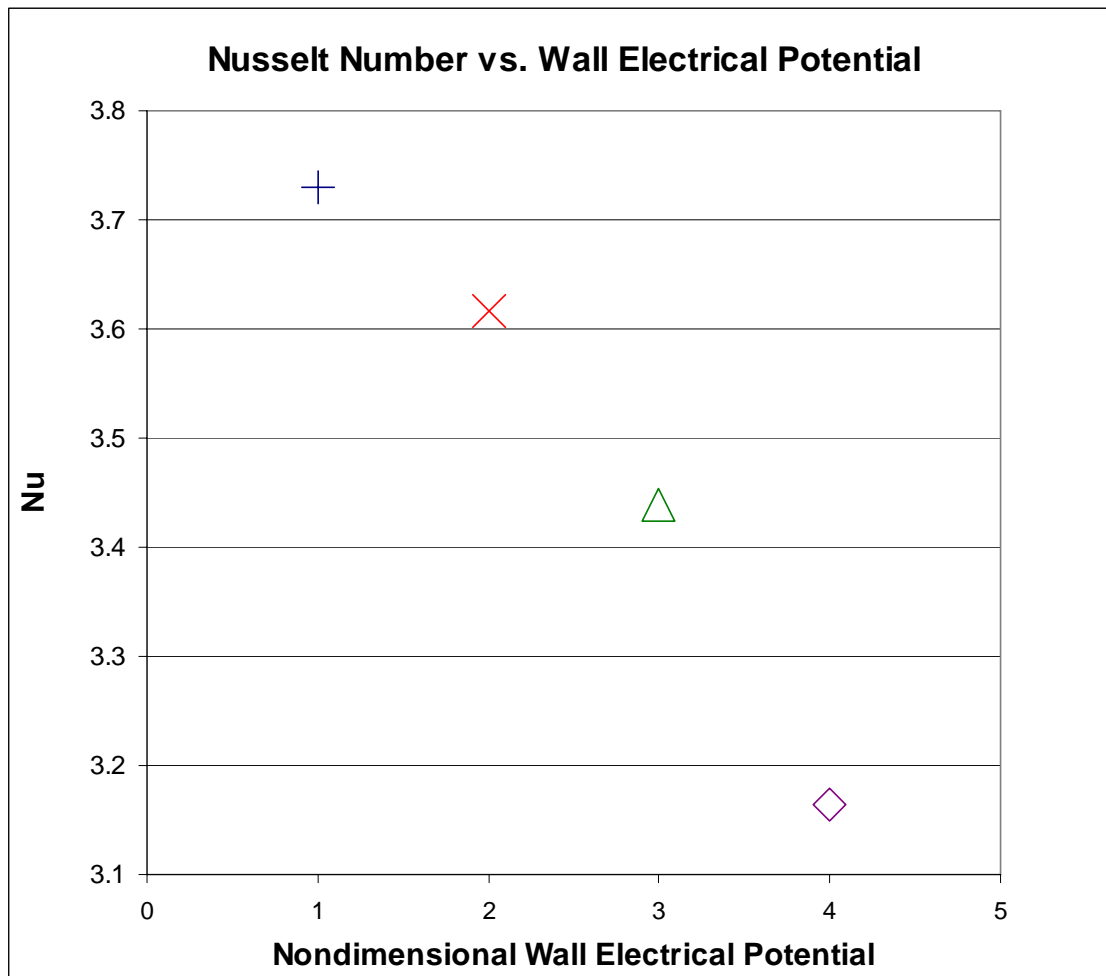


Figure 6.30 Nusselt number in the fully developed region vs. nondimensional wall electrical potential

## Chapter Seven

### CONCLUSIONS AND FUTURE WORK

---

#### 7.1 CONCLUSIONS

In the current study, the 3-D flow field for a microchannel was modeled based on the Navier-Stokes equations. Both developing and fully developed flows were included so that a realistic and practical model can be obtained. A nonlinear source term in the form of an electrical body force was included in the z-direction of momentum governing equations to simulate the EDL effect with the electrical potential of the fluid. A Poisson equation was used to relate the electrical potential and ion concentration. As the developing region was included, Nernst-Planck equations were used to simulate the ion concentration distribution. Microchannel heat sink is known as a potential high performance heat exchanger that is used to regulate the temperature of electronic devices with high heat flux capacity. A comprehensive 3-D thermal model based on conservation of energy was thus used to model the temperature field. The development of velocity, temperature and ion concentration can then be predicted, so as to have a better insight of the EDL effect. Numerical scheme, SIMPLER, was used to solve the partial differential equations for the modeling. A code written in computer language FROTRAN was compiled to predict the flow field. Verification of the in-house developed code was done based on the 2-D velocity profile, friction coefficient, Nusselt number and electrical potential in the fully developed region.

The present research shows that the EDL has a significant effect and it indicates similar result as effect of wall friction on the flow field, in such a manner

that, the streamwise direction velocity (in z-direction) will tend to have a parabolic distribution at the cross-section of the channel. Consequently, a smaller flow rate is expected. Due to the development of ion concentration, with EDL effect, it was found that a longer entrance length is expected for flow field to be fully developed. Therefore, EDL effect is important in microchannels, which cannot be neglected and it decreases the effectiveness of the microchannel.

The prediction of performance of microchannels based on the PBM was done to compare with the prediction based on NPM. The discrepancy in the results predicted by the two models is more dominant at the near wall region and not in the mainstream region. Therefore PBM is still an attractive model to compute EDL effect in microchannel, even for developing flows. The PBM is more cost effective (CPU & RAM) as compared to NPM (for the case study used in section 6.2, with RAM of 256 MB, the CPU time for prediction using PBM and NPM are 1168 and 2394 seconds respectively) and there is less discrepancy of modeling the EDL in the mainstream region. However, PBM is less suitable if the attention is on the flow field at the near wall region.

The effect of some parameters that affect the EDL effect such as Schmidt number and wall electrical potential on microchannel was further studied. An increase in Schmidt number will lead to decrease in friction coefficient. The effect of Schmidt number was however found to be less significant when compared to the effect of wall electrical potential. The increase in the wall electrical potential was followed by reduction in Nusselt number, resulting in the deterioration of the efficiency of the microchannel.

The important contributions of the author are listed as follows:

1. A comprehension of literature review that is related to microchannel is documented.
2. A 3-D body force term due to EDL effect for developing flow field is derived (section 3.3.1). The body force is coupled with Navier-Stoke equations for simulation of the EDL effect.
3. Numerical treatment and linearization of the highly non-linear term in the Nernst-Planck equations and the Z-direction momentum equation, in order to obtain the possible convergence solution effectively.
4. The code was developed from scratch (which is enormous amount of work) based on SIMPLER algorithm.
5. With the current developed code, the following unique study of done
  - a. Comparison between the prediction using PBM and NPM on velocity, thermal, electrical field and important parameter such as  $fRe$  and  $Nu$ , at 3-D developing flow region.
  - b. The effect of the aspect ratio on  $fRe$  and  $Nu$  and entrance length was studied and discuss.
  - c. The effect Schmidt Number ( $Sc$ ) on the  $fRe$ ,  $Nu$  and charge concentration for 3-D flow field at developing region is study and discuss.
  - d. The effect of the 3-D electrical field at developing flow on  $fRe$  and  $Nu$  and entrance length was studied and discuss.

## 7.2 FUTURE WORK

The future work proposed is as follows.

1. Flow field of more complex geometries i.e. blend, spiral etc. should be investigated.
2. The magnetic effect due to the flow of the ion (termed as streaming current in equation 3-22). Each streaming current is a source of magnetic field. As all streamline of ion flow at same direction, there will be attract force on the ions between different streamline. This force in due to magnetic effect is essential and should be studied.
3. The flow behavior and heat transfer performance of a microchannel heat sink including the potential of using a non-Newtonian fluid can be examined.
4. The performance of a microchannel with an unsteady or transient flow field should be investigated.

## REFERENCES

---

Adams, T. M., Abdel-Khalik, S. I., Jeter, S. M., and Qureshi, Z. H., 1998. An experimental investigation of single-phase forced convection in microchannels. *Int. J. Heat Mass Transfer* 41(6-7): 851-857.

Anderson, D. A., Tannehill, J. C., and Pletcher, R. H., 1984. *Computational Fluid Mechanics and Heat Transfer*, Hemisphere, WA.

Ames, W. F., 1992. *Numerical Methods For Partial Differential Equation*, Academic Press, San Diego.

Arkilic, E. B., Breuer, K. S., and Schmidt, M. A., 1994. Gaseous flow in microchannels. *Application of Microfabrication to Fluid Mechanics*: 57-66.

Arkilic, E. B., Schmidt, M. A., and Breuer, K. S., 1997. Gaseous slip flow in long microchannels. *Journal of Microelectromechanical Systems* 6(2): 167-178.

Baker, J., and Calvert, M. E., 1996. Effect of variable viscosity on coupled heat and momentum transfer in microchannel flows. 1996 Fluid Engineering Division Conference 2: 775-782.

Beck, J. V., Cole, K. D., Haji-Sheikh, A., and Litkouhi, B., 1992. *Heat Conduction Using Green's Function*, Hemisphere, London.

## References

---

Beskok, A., and Karniadakis, G. E., 1992. Simulation of slip-flows in complex microgeometries. *Micromechanical Systems* 40:355-370.

Beskok A., and Karniadakis G. E., 1994. Simulation of heat and momentum transfer in complex microgeometries. *Journal of Thermophysics and Heat Transfer* 8(4): 647-655.

Beskok, A., Karniadakis, G. E., and Trimmer, W., 1996. Rarefaction and compressibility effects in gas microflows. *Journal of Fluids Engineering* 118: 448-456.

Bowers, M. B., and Mudawar, I., 1993. Two-phase electronic cooling using mini-channel and micro-channel heat sinks: Part 1 - Design criteria and heat diffusion constraints. *Advances in Electronic Packaging* 4(2): 693-702.

Bowers, M. B., and Mudawar, I., 1993. Two-phase electronic cooling using mini-channel and micro-channel heat sinks: Part 2 - Flow rate and pressure drop constraints. *Advances in Electronic Packaging* 4(2): 703-712.

Bowers, M. B., and Mudawar, I., 1994. High flux boiling in low flow rate, low pressure drop mini-channel and micro-channel heat sinks. *Int. J. Heat Mass Transfer* 37(2): 321-332.



## References

---

Chen, X. Y., Toh K. C., Yang, C. and Chai, J. C., 2004. Numerical computational of hydrodynamically and thermally developing liquid flow in microchannel with electrokinetics effects, Journal of Heat Transfer, Transactions of the ASME, Vol. 126, 70-75

Choi, U. S., Rogers, C. S., and Mills, D. M., 1992. High-performance microchannel heat exchanger for cooling high-heat-load X-ray optical elements. Micromechanical Systems 40: 83-89.

Copeland, D., 1995. Manifold microchannel heat sinks: Analysis and optimization. Thermal Science and Engineering 3(1): 7-12.

Copeland, D., 1995. Manifold microchannel heat sinks: Numerical analysis. Cooling and Thermal Design of Electronic Systems 15: 111-116.

Copeland, D., Behnia, M., Nakayama, W., and Pak, B.-C., 1997. Manifold microchannel heat sinks: Review and comparison. Advances in Electronic Packaging 19-2: 2065-2070.

Copeland, D., Takahira, H., Nakayama, W., and Pak, B.-C., 1995. Manifold microchannel heat sinks: Theory and experiment. Advances in Electronic Packaging, 102: 829-835.

## References

---

Diev, M. D., and Leontiev, A. I., 1998. A study of liquid microlayer during boiling in narrow vertical slot channels, *Experimental Heat Transfer* 11: 101-120.

Emi, O., and Yasuaki, K., 1997. Boundary layer characteristics change in the case of micron-sized rough surface. *The Seventh Asian Congress of Fluid Mechanics*: 801-804.

Eringen, A. C. and Okada, K., 1995. A lubrication theory for fluids with microstructure. *Int. J. Engng. Sci.* 33(15): 2297-2308.

Fletcher, C.A.J., 1991. *Computational Techniques For Fluid Dynamics* 1, 2 d Ed., Springer-Verlag, Berlin.

Flik, M. I., Choi, B. I., and Goodson, K. E., 1991. Heat transfer regimes in microstructures. *Micromechanical Sensors. Actuators, and Systems*: 31-47.

Fu, L. M., Yang, R. J., and Lee G. B., 2002. Analysis of Geometry Effects on Band Spreading of Microchip Electrophoresis. *Electrophoresis* 2002, 23, 602-612.

Fu, L. M., Yang, R. J., Lee, G. B. and Liu, H. H., 2002. Electrokinetic Injection Techniques in Microfluidic Chips, *Analytical Chemistry*, Vol. 74, No.19 (2002) 5084-5091

## References

---

Fu, L. M., Lin, J. Y. and Yang, R. J., 2003. Analysis of electroosmotic flow with step change in zeta potential, *Journal of Colloid and Interface Science* 258 (2003) 266-275

Gravesen, P., Branebjerg, J., and Jensen, O. S., 1993. Microfluidics- a review. *J. Micromech. Microen.* 3: 168-182.

Goodson, K. E., Kurabayashi, K., and Pease, R. F. W., 1995. Improved heat sinking for laser-diode arrays using microchannels in CVD diamond. . 1995 National Heat Transfer Conference 3: 187-192.

Harley, J., Pfahler, J., Bau, H., and Zemel, J. N., 1989. Transport processes in micron and submicron channels. *Convection Heat Transfer and Transport Processes*: 1-5.

Hetsroni, G., Yarin L. P., and Kaftori, D., 1996. A mechanistic model for heat transfer from a wall to a fluid. *Int. J. Heat Mass Transfer* 39(7): 1475-1478.

Ho, C. M., and Tai, Y. C., 1994. MEMS: Science and technology. Application of Microfabrication to Fluid Mechanics: FED- Vol.197, 39-50, ASME

Ho, C. M., and Tai, Y. C., 1998. Micro-electro-mechanical- systems (MEMS) and fluid flows. Annu. Rev. Fluid Mech. 30: 579-612.

Hoffmann, K.A., 1989. Computational Fluid Dynamics for Engineers. Engineering Education System, Austin, Texas

## References

---

Hunter, R. J., 1981. Zeta Potential in Colloid Science: Principles and Applications, Academic Press, New York.

Incropera, F. P., 1988. Convection heat transfer in electronic equipment cooling. Journal of Heat Transfer, 110: 1097-1111.

Jayakanthan, A., Hassan, A. Y., and Seetharamu, K. N., 1997. Applications of CFD in cooling of electronic packages. The Seventh Asian Congress of Fluid Mechanics: 777-780.

Kendall, S. R., 1996. Analysis of fluid flow through micron sized rectangular passages. Ph.D. Diss., University of Huddersfield, U. K..

Kendall, S. R., and Rao, H. V., 1995, CFD analysis of flow through micron sized rectangular passages. Numerical Methods in Laminar and Turbulent Flow 9: 1235-1245.

Kendall, S. R., and Rao, H. V., 1997. The relationship between Reynolds number and the friction factor in micro-passage flows. Numerical Methods in Laminar and Turbulent Flow 10: 1160-1169.

## References

---

Khrustalev, D., and Faghri, A., 1995. Boiling heat transfer in the miniature axially grooved rectangular channel with discrete heat sources. 1995 National Heat Transfer Conference 3: 165-174.

Knight, R. W., Hall, D. J., Goodling, J. S., and Jaeger, R. C., 1992. Heat sink optimization with application to microchannels. IEEE Transactions on Components, Hybrids, and Manufacturing Technology 15(5): 832-842.

Knight, R. W., Goodling J. S., and Gross, B. E., 1992. Optimal thermal design of air cooled forced convection finned heat sinks - experimental verification. IEEE Transactions on Components, Hybrids, and Manufacturing Technology, 15(5): 754-760.

Landram C. S., 1994. Microchannel flow boiling mechanisms leading to burnout. Heat Transfer in Electronic Systems 292: 129-136.

Lin, L., Udell, K. S., and Pisano, A. P., 1993. Vapor bubble formation on a micro heater in confined and unconfined micro-channels. Heat Transfer on the Microscale: 85-93.

Ma, S. W., Gerner, F. M., and Tsuei, Y. G., 1992. Forced convection heat transfer from microstructures. Heat Transfer on the Microscale: 35-43.

## References

---

Mahalingam M., and Andrews, J., 1988. High performance air cooling for microelectronics. Cooling Technology for Electronic Equipment: 139-155.

Mala, G. M., Li, D., and Dale, J. D., 1997. Heat transfer and fluid flow in microchannels. Int. J. Heat Mass Transfer 40(13): 3079-3088.

Mala, G. M., Li, D., Wemer, C., Jacobasch, H. -J., and Ning, Y. B., 1997. Flow characteristics of water through a microchannel between two parallel plates with electrokinetic effects. Int. J. Heat and Fluid Flow 18: 489-496.

Mala, G. M., Yang, C. and Li D., 1998. Electrical double layer potential distribution in a rectangular microchannel. Colloids and Surfaces A: Physicochemical and Engineering Aspects 135 (1998) 109-116

Nagasaki, T., Hijikata, K., Fushinobu, K., and Phelan, P. E., 1992. Numerical simulation of the conjugate direct cooling of a micro heat generating element. Advances in Electronic Packaging 1(1): 217-223.

Ng, E.Y.K., and Liu, N., 2002. The impacts of time-step size in the application of DSMC method to ultra-thin gas film lubrication. Journal of Micromechanics and Microengineering 12 (2002) 1-7.

## References

---

Ng, E.Y.K., and Poh, S. T., 2000. Investigative study of manifold microchannel heat sinks for electronic cooling design. Journal of Electronics Manufacturing 9(2): 155-166.

Ng, E. Y. K. and Poh, S. T., 2000. Parametric studies of microchannel conjugate liquid flows with Zeta potential effects, Journal of Electronics Manufacturing, Vol. 10, No. 4 (2000) 237-252

Ng, E. Y. K. and Poh, S. T., 2002. Modelling of electric double layer effects through pressure-driven microchannel flows, CMES, Vol. 3. No. 3 (2002) 351-365

Ng, E. Y. K., and Poh S. T., 2002. Modeling of electric double layer effects through pressure-driven microchannel flows. J. of Computer Modeling in Engineering & Sciences, vol. 3, no. 3, 351-365, 2002.

Ng, E. Y. K. and Tan, S.T., 2004. Computation of 3D Developing Pressure-driven Liquid Flow in Microchannel with EDL Effect, Numerical Heat Transfer, Part A: Applications, vol. 45, no. 10, 1013-1027.

Ng, E. Y. K., Tso, C. P., Wen, Z. M. and Choo, K. F., Numerical simulation of flow and conjugate heat transfer in a microchannel for electronics cooling. Journal of Electronics Manufacturing, Vol. 9, No. 2 (1999) 141-153

## References

---

Nguyen, N. T., Bochnia, D., Kiehnscherf, R., and Dotzel, W., 1996. Investigation of forced convection in microfluid systems. Sensors and Actuators, 55: 49-55.

Obot, N. T., 2002. Toward a Better Understanding of Friction and Heat/mass Transfer in Microchannels-- a literature review, Microscale Thermophysical Engineering, vol. 6, no. 3, 155-173.

Pak, B.-C., Chun, W.C., Baek, B.J., and Copeland, D., 1997. Forced air cooling by using manifold microchannel heat sinks. Advances in Electronic Packaging 19-2: 1837-1842.

Patankar, S.V., 1980. Numerical Heat Transfer and Fluid Flow, McGraw-Hill, New York.

Patankar, S.V., 1991. Computation of Conduction and Duct Flow Heat Transfer, Innovative Research, Inc, Maple Groove.

Peng, X. F., and Peterson, G. P., 1995. The effect of themofluid and geometrical parameters on convection of liquids through rectangular microchannels. Int. J. Heat Mass Transfer 38(4): 755-758.

Peng, X. F., Wang, B. X., Peterson, G. P., and Ma, H. B., 1995. Experimental investigation of heat transfer in flat plates with rectangular microchannels. Int. J. Heat Mass Transfer 38(1): 127-137.



## References

---

Peng, X. F., Peterson, G. P., and Wang, B. X., 1996. Flow boiling of binary mixtures in microchannels plates. Int. J. Heat Mass Transfer 39(6): 1257-1264.

Peng, X. F., Wang, B. X., Peterson, G. P. and MA, H. B., Experimental investigation of heat transfer in flat plates with rectangular microchannels, Int. J. Heat Mass Transfer Vol 38, No. 1, (1995) 127-137

Peng, X. F., Hu, H. Y., and Wang, B. X., 1998. Boiling nucleation during liquid flow in microchannels. Int. J. Heat Mass Transfer 41(1): 101-106.

Pfahler, J., Harley, J., Bau, H., and Zemel, J. N., 1991. Gas and liquid flows in small channels. Micromechanical Sensors, Actuators, and Systems: 49-60.

Phillips, R. J., 1990. Microchannel heat sinks. Advances in Thermal Modeling of Electronic Components 2(Chap. 3): 109-184.

Phillips, R. J., Glicksman, L. R., and Larson, R., 1988. Forced-convection, liquid-cooled, microchannel heat sinks for high-power-density microelectronics. Cooling Technology for Electronic Equipment: 295-316.

Piekos, E. S., and Breuer, K. S., 1996. Numerical modeling of micromechanical devices using direct simulation Monte Carlo method. Journal of Fluids Engineering 118: 464-469.

## References

---

Poh, S. T., and Ng, E. Y. K., 1998. Heat transfer and flow issues in manifold microchannel heat sinks: A CFD approach. 1998 IEEE/CPMT 2nd Electronics Packaging Technology Conference: 246-250.

Poh, S. T., and Ng, E. Y. K., 1999. Fluid flow and heat transfer in manifold microchannel heat sinks: A CFD approach. Computer Modeling and Simulation in Engineering 4(4): 282-289.

Pong, K. C., Ho, C. M., Liu, J., and Tai, Y. C., 1994. Non-linear pressure distribution in uniform microchannels. Application of Microfabrication to Fluid Mechanics: 51-56.

Probstein R. F., 1994. Physicochemical Hydrodynamics, An Introduction, 2nd ed.. John Wiley & Sons Ltd.. New York.

Rahman, M. M., and Gui, F., 1993. Experimental measurements of fluid flow and heat transfer in microchannel cooling passages in a chip substrate. Advances in Electronic Packaging 4(2): 685-692.

Ravigururajan, T. S., and Drost, M. K., 1996. Liquid flow characteristics in a diamond pattern micro-heat-exchanger. Microelectromechanical Systems (MEMS): 159-166.

## References

---

Rujano, J. R., and Rahman, M. M., 1995. Analysis and computation of conjugate heat transfer in trapezoidal microchannel heat sinks in a silicon substrate. 1995 National Heat Transfer Conference 3: 175-185.

Shah, R. K., and London A. L., 1978. Laminar Flow Forced Convection in Ducts, A source Book for Compact Heat Exchanger Analytical Data, Academic Press, New York.

Samaraskii, A. A., and Vabishchevich, P. N., 1995. Computational heat transfer, Volume 1: Mathematical modeling. Chichester: 1st ed. John Wiley & Sons Ltd..

Samalam, V. K., 1989. Convective heat transfer in microchannels. Journal of Electronic Materials 18(5): 611-617.

Shah, R. K., and London A. L., 1978. Laminar Flow Forced Convection in Ducts, A Source Book for Compact Heat Exchanger Analytical Data, Academic Press, New York.

Schlichting, H., "Boundary layer Theory," 7th ed., McGraw-Hill, New York, 1979

Tan S.T., and, Ng, E. Y-K., Numerical Studies of Developing Flow in Microchannel, International Journal of Computational Engineering Science, Special Issue on MEMs, Vol. 4, No:2, Imperial College Press, (2003), Pp. 389-392.

## References

---

Tardu S., 2003. The Electric Double Layer Effect on the Microchannel Flow Stability. First International Conference on Microchannels and Minichannels. April 24-25, 2003, New York.

Tardu S, Analysis of the Electric Double Layer Effect on Microchannel Flow Stability, *Microscale Thermophysical Engineering*, vol. 8, no. 4, 383-401, 2004.

Tardu S, Intercial Electrokinetic Effect on the Microchannel Flow Linear Stability, *Journal of Fluids Engineering, Trans ASME Vol 126*, 10-13

Tien, C. L., and Chen, G., 1994. Challenges in microscale conductive and radiative heat transfer. Journal of Heat Transfer 116: 799- 807.

Tso, C. P., and Mahulikar, S. P., 1998. The use of the Binkmann number for single phase forced convective heat transfer in microchannels. *Int. J. Heat Mass Transfer* 41(12): 1759-1769.

Tuckennan, D. B., 1984. Heat-transfer microstructures for integrated circuits. Ph.D. Diss., Stanford University.

Tuckerinan, D. B., and Pease R. F. W., 1981. High-performance heat sinking for VLSI. IEEE Electron Device Letters 2(5): 126-129.

Van de Ven T.G.M., 1989. Colloidal Hydrodynamics, Academic Press, San Diego

## References

---

Weast, R., Astle, M.J., and Beyer, W.H., 1986. CRC Handbook of Chemistry and Physics, CRC Press Inc., Boca Raton.

Weisberg, A., Bau, H. H., and Zemel, J. N., 1992. Analysis of microchannels for integrated cooling. Int. J. Heat Mass Transfer 35(10): 2465-2474.

White F. M., 1988. Fluid Mechanics. McGraw-Hill Book Company, New York

Yang, C. and Li, D., 1997. Electrokinetic effects on pressure-driven liquid flows in rectangular microchannels. J. Colloid and Interface Science. 194: 95-107 (1997).

Yang, C. and Li, D., 1998, Analysis of electrokinetic effects on the liquid flow in rectangular microchannels. Colloids Surfaces A: Physicochem. Eng. Aspects 143 (1998) 339-353.

Yang, C., Li, D., and Masiiyah, J. H., 1998. Modeling forced liquid convection in rectangular microchannels with electrokinetic effects. Int. J. Heat Mass Transfer 41: 4230-4249.

Yang, R. J., Fu, L. M. and Hwang, C. C., Electroosmotic entry flow in a microchannel, Journal of Colloid and Interface Science 244 (2001) 173-179

## References

---

Yang, R. J., Fu, L. M. and Lee, G. B., Electroosmotic Flows in Microchips Chips, The 5<sup>th</sup> Asian Computational Fluids Dynamics Busan, Korea, (2003) 27-30

Yang, R. J., Fu, L. M. and Lin, Y. C., Electroosmotic flow in Microchanel, Journal of Colloid and Interface Science 239 (2001) 98-105

Yeung, T. S., Yuen, M. M. F., and Zohar, Y., 1995. Heat transfer in a microcooling system. The Sixth Asian Congress of Fluid Mechanics: 785-788.

You, H. I., 1989. Experimental determination of heat transfer coefficient between a microstucture and fluid. Int. Comm. Heat Mass Transfer 16: 537-546.

Zengerle, R., and Richter, M., 1994. Simulation of microfluid systems. J. Micromech. Microeng. 4:192-204.